

Chapter 12

Nanomedicine

12.1 Introduction

Applications of nanotechnology for diagnosis, treatment, monitoring, and control of biological systems have been referred to as “nanomedicine” by the US National Institute of Health (NIH) [12.1]. According to a Forward Report published by the European Science Foundation [12.2], nanomedicine aims at “ensuring the comprehensive monitoring, control, construction, repair, defense, and improvement of all human biological systems, working from the molecular level using engineering devices and nanostructures, ultimately to achieve medical benefit” [12.3]. Nanotechnology is positively impacting health care. Nanomedicine is an interdisciplinary approach because it requires the intersection of many disciplines including biology, chemistry, physics, chemical and mechanical engineering, materials science, and clinical medicine [12.4]. Nanoscale and biosystems research are merging with information technology and cognitive science, leading to completely new science and technology platforms such as those for genome pharmaceutics, biosystems on a chip, regenerative medicine, and neuroscience [12.5].

At the forefront of projects in nanomedicine is the research into the rational delivery and targeting of pharmaceutical, diagnostic, and therapeutic agents via intravenous and interstitial routes of administration [12.1]. These involve the identification of precise targets (cells and receptors) related to specific clinical conditions and choice of the appropriate nanocarriers to achieve the required responses while minimizing side effects. Since human illness begins and advances at the cellular level, recent breakthroughs and advances (see [12.1]) in understanding how materials like proteins or drug ingredients affect an individual cell can give researchers important insight into how the material might impact the entire human body [12.6].

The field of nanomedicine is currently in its early phase of sharp growth and may be a considerable number of years away from maturity [12.4]. A continuous impact of nanotechnology on health care is, however, expected at many levels including (1) detection of molecular changes in disease pathogenesis; (2) disease diagnosis and imaging; (3) targeted drug delivery and therapy; (4) multifunctional systems for combined diagnostic and therapeutic applications; (5) vehicles to report the *in vivo* efficacy of therapeutic agents, and (6) nanoscience basic research (see

[12.4]). In addition, the unprecedented precision of nanotechnology for cellular and intracellular manipulation opens the field of nanosurgery [12.7]. Despite the great rash into nanomaterials, there certainly is a heightened awareness of the potential problems that exist [12.8]. For example, although NanoMedicine Summit 2008 presented a huge number of potential applications of nanotechnology to medicine (www.nanomedicinesummit.org/agenda.asp), we also note that there are serious concerns to be addressed [12.9].

Nanoparticles including colloidal gold, semiconductor quantum dots, iron oxide nanocrystals, or nanocrystalline bismuth sulfide with typical sizes of 1–20 nm or polymeric micelles, dendrimers, and liposomes ranging from a few to 250 nm are being studied for medical diagnosis and therapy. Some of them, such as iron oxide nanoparticles for contrast enhancement in magnetic resonance imaging (MRI) [12.10], liposomes conjugated with the anticancer agent doxorubicin (Doxil) [12.4], or albumin nanoparticles decorated with the anticancer drug paclitaxel (Abraxane) [12.11] have gained approval by the US Food and Drug Administration (FDA) and by regulatory bodies in other countries [12.10]. Gold and silver nanoparticles can absorb and scatter light from UV to near-infrared (NIR) wavelengths due to their size- and shape-dependent surface plasmon oscillations (see [12.12]). In semiconductor quantum dots, such as, e.g., CdSe, the fluorescence emission wavelength (UV to NIR) can be tuned due to the size-dependent spacing of the electron energy levels [12.13] yielding the potential to revolutionize cell, receptor, antigen, and enzyme imaging (see [12.1]). Iron oxide nanocrystals are of importance for MRI contrast enhancement, as they cause changes in the nuclear spin relaxation times of neighboring water molecules. By virtue of their small size and by functionalizing their surface with polymers and appropriate ligands, intravenously or subcutaneously administered nanoparticulate carriers can be targeted to specific cells, locations, or organs within the body where these agents can cure diseases, minimizing unwanted side effects. Some nanoparticles are designed with the focus on multifunctionality for simultaneous targeting, drug delivery, and sensing (see [12.1]).

Nanoparticles injected intravenously can be retained in the blood circulation for a longer period by appropriate surface manipulation. The particle escape from the vasculature is mainly restricted to sites where the capillaries have open fenestration, as in the sinus endothelium of the liver or when the integrity of the endothelial barrier is perturbed by inflammatory processes or by tumor growth which is the result of dysregulated angiogenesis. In the liver, the size of fenestrae in the sinus endothelium can be as large as 150 nm; in tumor capillaries they rarely exceed 300 nm. This escape of nanoparticles from the vasculature can be exploited to direct diagnostic and therapeutic entities to selected pathological vessels, particularly to those of cancer (see [12.1]). Furthermore, by appropriate targeting ligands conjugated to the nanoparticles, these can search for signature molecules expressed by the target, a process often referred to as active targeting.

Interstitial injection of nanoparticles, however, may be the preferred choice, particularly if the target is a specific lymph node (see [12.1]). After interstitial injection, many of the overlapping endothelial cells are separated and thus passage ways are

provided between the interstitium and the lymphatic lumen through which particles are conveyed to the node via the afferent lymph. The fate of interstitially injected nanoparticles is controlled by their size and surface characteristics. The size of the particles must be large enough to prevent their leakage into the blood capillaries; particles in the range of 30–100 nm satisfy this criterion, whereas particles larger than 100 nm move very slowly and are susceptible to clearance by interstitial macrophages. Very small particles (1–20 nm), particularly when they are long circulatory, can slowly extravasate from the vasculature into the interstitial spaces, from which they are transported to lymph nodes via lymphatic vessels (see [12.1]).

The convergence of nanoscale science with modern biology and medicine is a trend that is reflected in science policy decisions [12.5]. In the United States, the National Institute of Health (NIH) has sponsored approximately 20 Nanomedicine Development Centers [12.14], including the seven centers of Cancer Nanotechnology Excellence at the University of North Carolina, the University of California, San Diego, the Emory-Georgia Tech, Caltech, and Washington University, St. Louis, MO. [12.15]. The European Commission launched a European Technology Platform on nanomedicine, with the goal of defining a European Strategic Research Agenda with the following priority list: cardiovascular diseases, cancer, musculoskeletal disorders, neurodegenerative diseases and psychiatric conditions, diabetes and bacterial and viral infection diseases. The Commission will channel some 100€ million into nanomedicine projects annually under its Seventh Framework Programme for research (2007–2013). Meanwhile the European Group on Ethics has published an opinion on nanomedicine, specifying that safety concerns should be a priority in the development of new techniques and treatments [12.16].

A number of International Conferences focused to nanomedicine have been organized recently, such as, *Cancer Nanotech 2007*, Paris, France, *Investing in Medical Nanotechnologies*, London, UK, 2006, or *Euro Nano Medicine Conference*, Bled, Slovenia, 2009.

The market for many drugs is rapidly expanding due to nanotechnology and nanoscience approaches to particle design and formulation, which is the basis for a highly profitable niche within the industry, although some predicted benefits may be hyped [12.1]. In addition, a sharp increase over the past years in the number of patent applications in this area underscores the heightened level of interest in nanomedicine by both academia and industry investigators [12.4]. However, although an estimated 130 nanotech-based drugs and delivery systems are being developed worldwide [12.3], a number of outstanding issues related to toxicity and environmental impact of nanoscale materials will have to be resolved before regulatory agencies can approve further products (see [12.3, 12.17]).

This chapter will review the application of nanoscience and nanotechnology in medicine that will transform disease diagnosis, therapy, and prevention in the near future. This medical change will usher in the era of mature nanomedicine and will be instrumental in the eventual emergence of nanosurgery and nanoneurosurgery. Mature nanomedicine will involve the design and fabrication of molecular devices with anatomic precision and then using them in patients to establish and maintain health [12.14].

12.2 Diagnostic Imaging and Molecular Detection Techniques

Medical imaging systems that provide anatomical and physiological information are now in widespread clinical and preclinical use (see [12.18]). By contrast, systems that obtain molecular information are just emerging.

Medical imaging modalities include [12.19] the following:

- (i) Magnetic resonance imaging (MRI). This is a phenomenon involving the transition between different energy levels of atomic nuclei under the action of a radiofrequency signal.
- (ii) Computed tomography (CT). This technique uses x-rays to create with the aid of computers cross-section images of the body and three-dimensional images of areas of interest.
- (iii) Ultrasound (US) imaging. This modality is based on the different passage rates of ultrasound through different types of tissues.
- (iv) Positron emission tomography (PET). In this technique radioactive isotopes are used which emit positrons (antiparticles of electrons). The positron-electron annihilation radiation emerging from a particular site is employed for tomographic imaging.
- (v) Emerging imaging modalities: Raman spectroscopy and photoacoustic tomography.
- (vi) Biomolecular detection techniques to identify the expression and activity of specific molecules and of biological processes for medical diagnosis.

In the following, the recent advances in these diagnostic techniques provided by nanotechnology and molecular approaches will be concisely reviewed.

12.2.1 Magnetic Resonance Imaging (MRI)

Although magnetic resonance imaging (MRI) is one of the most powerful medical diagnosis tools, its temporal resolution and sensitivity performance can be significantly improved by utilizing magnetic nanoparticles [12.20, 12.21].

For MRI, ferrite iron oxide magnetite (Fe_3O_4) or maghemite ($\gamma\text{-Fe}_2\text{O}_3$) nanoparticles (Fig. 12.1) are used, with high saturation magnetizations of 92 emug^{-1} or 78 emug^{-1} at 300 K, respectively (see [12.21]). These nanoparticles are superparamagnetic, i.e., they are characterized by a large magnetic moment in an external magnetic field, but their magnetization is reduced to zero upon removal of the external field.

The effect of magnetic nanoparticles on MRI is the following: The external field induces a magnetization in the magnetic nanoparticles, they align and their magnetization gives rise to a stray field δM (Fig. 12.2) with a very high local magnetic field gradient. This induces dephasing of water proton spins and consequently shortening of the T_1 and T_2 relaxation times of the surrounding water molecules, resulting in a darkening of the local MR imaging (Fig. 12.2b).

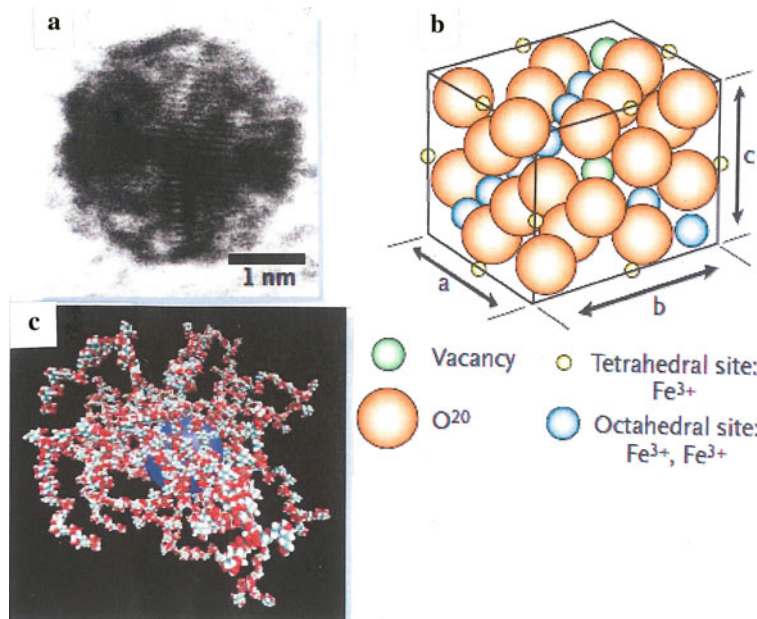


Fig. 12.1 Superparamagnetic iron oxide nanoparticles with a lymphotropic dextran coating. (a) Electron micrograph of a nanoparticle. (b) Crystal structure of the iron oxide nanoparticle. (c) Molecular model of the surface-bound 10 kDa dextrans with a mean size of 28 nm. (Reprinted with permission from [12.22]. © 2003 Massachusetts Medical Society)

For high-contrast magnetic resonance imaging (MRI), MnFe_2O_4 nanoparticles with a mixed spinel structure and a diameter of 12 nm have been developed, yielding higher relaxivities $R_2 = 1/T_2$ and therefore better contrast than Fe_3O_4 nanoparticles [12.23]. After conjugation with the cancer-targeting antibody Herceptin, which specifically binds to the HER2/neu marker overexpressed in breast and ovarian cancer, tumors as small as 50 mg could be detected in mice by MRI [12.23].

When magnetic nanocrystals are conjugated with biologically active materials (e.g., antibodies), the conjugates exhibit multifunctionality of both an MRI contrast enhancement and a selective biological recognition of target molecules. This conjugate can efficiently report on molecular and genetic events in target tissues [12.20]. Iron oxide nanocrystals of various sizes can be fabricated with narrow size distributions (Fig. 12.3) and modified by, e.g., 2,3-dimercaptosuccinic acid (DMSA) ligands for water solubility. When these modified nanocrystals are conjugated to the cancer-targeting antibody molecule, Herceptin (Fig. 12.3d), these conjugates can be effectively used for breast cancer diagnosis (see [12.20]). When used for *in vivo* detection of NiH3T6.7 cancer cells with Her 2/ neu overexpression, implanted in mice, these tumor sites could be imaged with high MRI contrast (Fig. 12.4). When unconjugated Fe_3O_4 control particles are injected into mice, no time-dependent changes in the color-mapped MRI signal (Fig. 12.4) and the T_2 value at the tumor

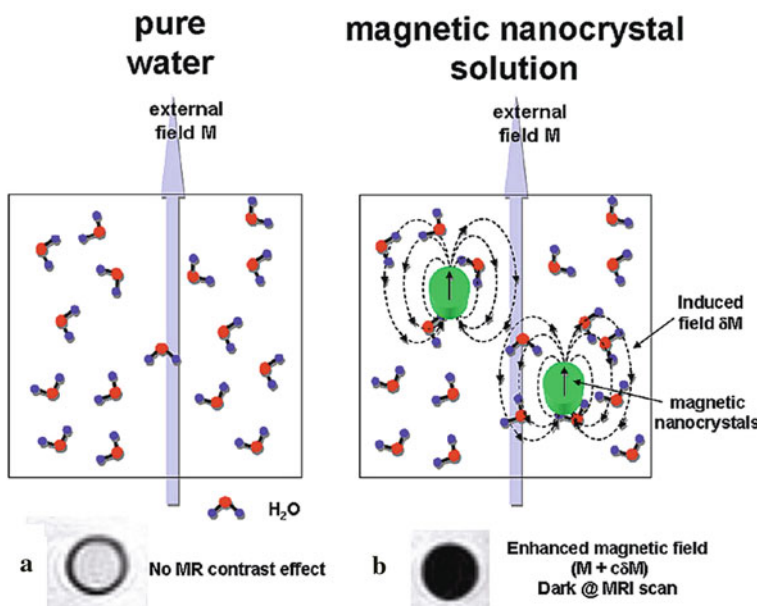


Fig. 12.2 Magnetic resonance imaging (MRI) contrast effect of magnetic nanocrystals. (Reprinted with permission from [12.20]. © 2006 Korean Chemical Society)

site are detected. In contrast, after injection of the Fe_3O_4 –Herceptin conjugates, immediate color changes to blue are evident and a drop of the T_2 within 10 min is observed. This demonstrates that the Fe_3O_4 –Herceptin conjugates successfully reach and bind to the target cancer cells for sensitive identification of tumors [12.20].

Most of the recent research of magnetic iron oxide nanoparticles for MRI contrast enhancement has concerned cellular imaging with imaging of in vivo macrophage activity showing that several clinical applications are possible: detection of liver metastases, metastatic lymph nodes, or inflammatory or degenerative diseases [12.21]. A few examples of nanoparticle MRI enhancement in brain cancer, breast cancer, myometrium and cervical tumors, prostate cancer lymph nodes, arthritis, infection, angiography, and atherosclerosis will be shown in the following.

Brain tumors. The determination of brain tumor margins both during the presurgical planning phase and during surgical resection has long been a challenging task in the therapy of brain tumor (see also Sect. 12.5) patients. Multimodal (magnetic and near-infrared fluorescent) nanoparticles have been explored recently in rats as a preoperative magnetic resonance imaging contrast agent in a 4.7T Bruker MRI tomography [12.24] and for intraoperative optical imaging of brain tumors [12.24]. The multimodal Cy5.5–CLIO nanoparticles consisted of dextran-coated iron oxide nanoparticles (CLIO) with the near-infrared fluorescent (NIRF) dye Cy5.5 attached to the coating.

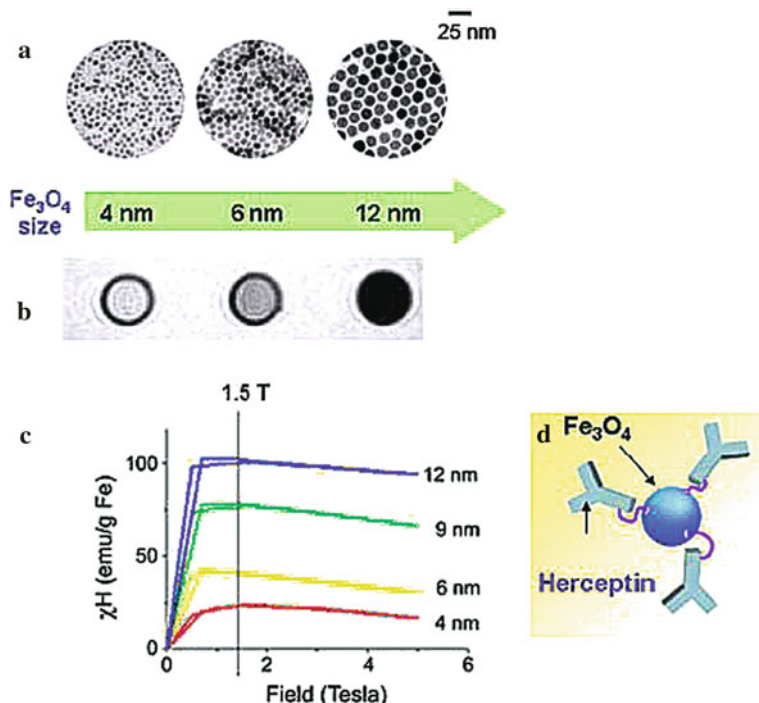


Fig. 12.3 Size-dependent properties of iron oxide (Fe_3O_4) nanocrystals and surface modification of the nanocrystals by Herceptin conjugates. **(a)** TEM imaging of Fe_3O_4 nanocrystals of various sizes. **(b)** Size-dependent T_2 -weighted MR images of water soluble Fe_3O_4 nanocrystals. **(c)** Magnetization of the water soluble Fe_3O_4 nanocrystals. **(d)** Schematic representation of Fe_3O_4 –Herceptin conjugates. (Reprinted with permission from [12.20]. © 2006 Korean Chemical Society)

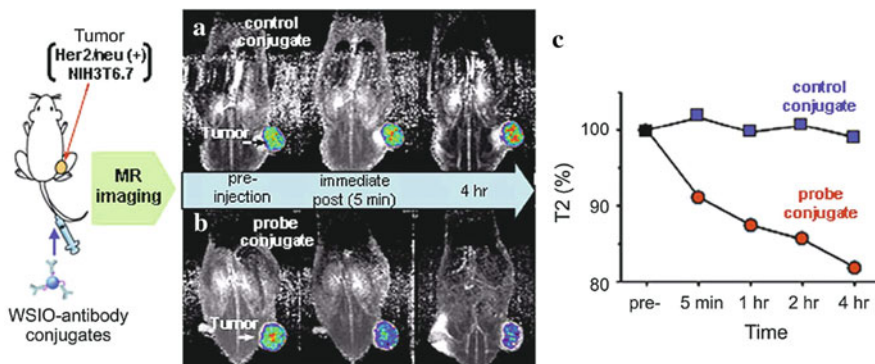


Fig. 12.4 In vivo MR detection of cancer implanted into a nude mouse. **(a)** Color maps of the T_2 -weighted MR images of cancer cells (NIH3T6.7) at different times after injection of Fe_3O_4 –antibody control conjugates into mice (preinjection; after 5 min, after 4 h) and **(b)** after injection of Fe_3O_4 –Herceptin probe conjugates. **(c)** T_2 values of cancer cells in **(a)** and **(b)** samples versus time after injection of nanoparticles. (Reprinted with permission from [12.20]. © 2006 Korean Chemical Society)

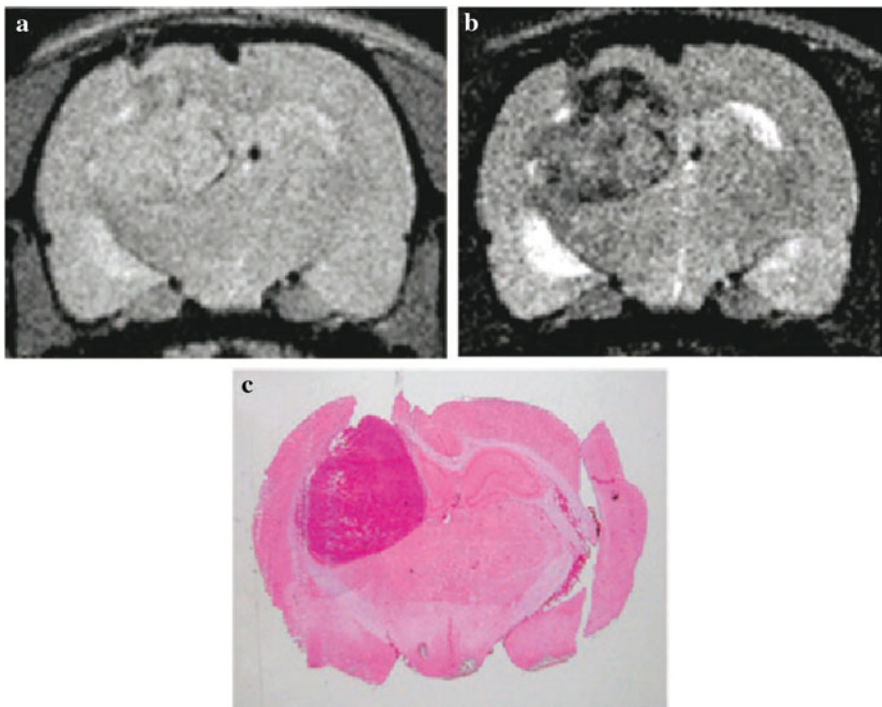


Fig. 12.5 Cy5.5-CLIO nanoparticles in a 9L rat glioblastoma (malignant cerebral tumor) as a preoperative MRI contrast agent. Proton density and T_2 -weighted images are shown in **a** and **b**, respectively. Tumor uptake of iron oxide (CLIO) nanoparticles is evident in the T_2 -weighted images (**b**) as regions of low-signal intensity (dark) whereas the tumor is isointense to the surrounding tissue using proton density images (**a**). **(c)** Hematoxylin and eosin (H&E) staining of a histological section corresponding to the MRI slices in A and B. (Reprinted with permission from [12.24]. © 2003 American Association of Cancer Research)

Figure 12.5 shows a representative example of a 9L rat glioblastoma by proton density-weighted MR imaging (Fig. 12.5a) and by T_2 -weighted MR imaging after Cy5.5-CLIO administration (Fig. 12.5b). The hypointense tumor relative to the surrounding tissue on the T_2 -weighted image (Fig. 12.5b) is indicative of nanoparticle accumulation, which causes a reduction of signal intensity with T_2 -weighted spin echo pulse sequences. This contrast is not seen with conventional Gd chelates [12.24]. There is high congruency between signal reduction in MRI and the histological imaging by hematoxylin and eosin (H&E) staining (Fig. 12.5c). It can be shown that Cy5.5-CLIO nanoparticles can be used to delineate brain tumors precisely in a rat model intraoperative setting. In Fig. 12.6, a rat is shown by white light illumination after craniotomy and exposition of the tumor. In Fig. 12.6b the tumor is imaged by the green fluorescence protein (GFP) expressed by the tumor and in Fig. 12.6c by the Cy5.5 near-infrared fluorescence (NIRF) coinciding with the GFP image. The tumor delineations are furthermore confirmed by histological investigations making

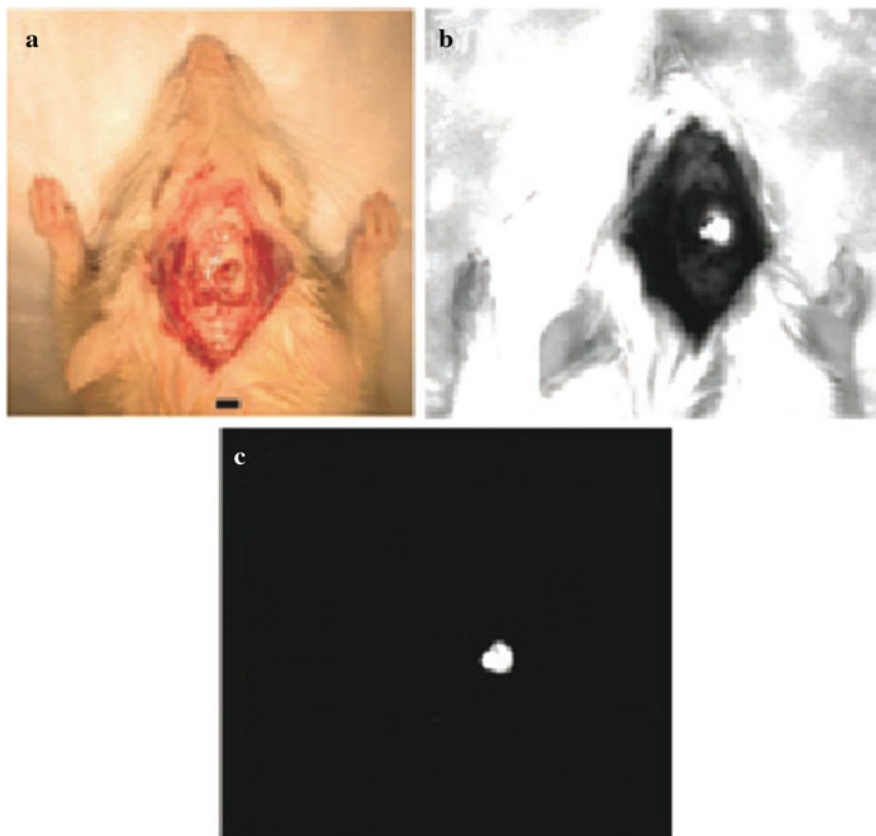


Fig. 12.6 Delineation of a GFP-expressing 9L glioma tumor (tumor in the supporting tissue of the brain) by optical imaging in an intraoperative setting. The brain tissue overlying the tumor was removed for optical imaging. (a) White-light imaging, (b) GFP imaging, and (c) Cy5.5 near-infrared fluorescence (NIRF) imaging. Scale bar: 5 mm. (Reprinted with permission from [12.24]. © 2003 American Association of Cancer Research)

use of H&E staining [12.24]. Thus, the combined NIRF optical and magnetic properties of Cy5.5–CLIO nanoparticles may allow neurosurgeons and radiologists to see the same probe in the same cells. This may increase the precision of surgical resection and improve the outlook for brain cancer patients.

Breast cancer lymphangiography. Breast cancer is the most common malignancy among women, resulting in approximately 45,000 deaths annually in the United States (see [12.25]). The presence of lymph node metastases has major prognostic implications in breast cancer patients, and it is the major criterion for adjuvant chemotherapy. The disease status of the sentinel lymph node (SLN) accurately reflects the status of the more distant lymph nodes. Therefore, the SLN metastasis diagnosis by non-invasive techniques such as MRI is of particular interest. By using polyamidoamine dendrimer G6 nanoparticles (9 nm in diameter; 240 kDa),

containing each 213 paramagnetic Gd ions, in lymphangiography, the metastatic foci of breast cancer-affected lymph nodes in mice could be revealed by the absence of MRI intensity [12.25]. This may be a powerful method for sentinel lymph node localization in human breast cancer [12.25]. It should be mentioned that there is a potential to detect even more and smaller lymph nodes by MRI in higher magnetic fields (3.0 T) compared to the situation in conventional fields (1.5 T) [12.26].

Myometrium and cervical carcinoma. Ultrasmall superparamagnetic iron oxide (USPIO) nanoparticles were used in order to study whether USPIO-enhanced T_2^* -weighted gradient-echo (GRE) images might provide advantages on disease staging (T-staging) of uterine malignancies having surgery and histology as standards of reference [12.27]. A decrease of the signal intensity of myometrium carcinoma (Fig. 12.7a, b) and of cervical carcinoma patients (Fig. 12.7c, d) on T_2^* -weighted

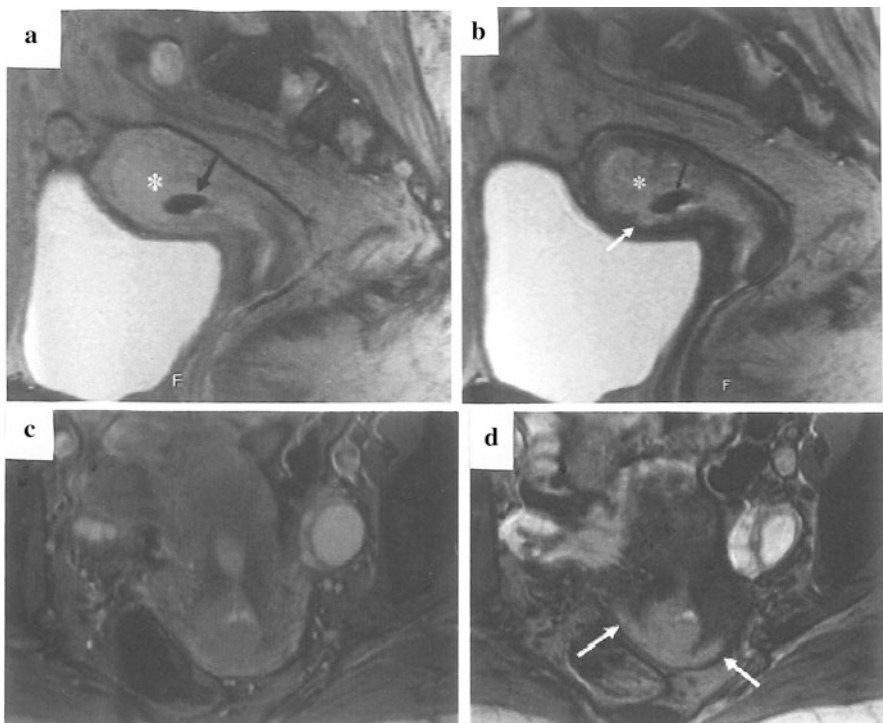


Fig. 12.7 (a, b): Patient with endometrial carcinoma (stage Ic according to the International Federation of Gynecology and Obstetrics-FIGO classification) and **c, d:** patient with cervical carcinoma (stage II FIGO). On the unenhanced T_2^* -weighted graded echo (GRE) image (a) the tumor (asterisk) shows a superficial infiltration of myometrium; USPIO-enhanced MR (b) shows a focal area of deep infiltration of the myometrium (white arrow) with a calcification within the tumor (black arrow). On the unenhanced GRE T_2^* -weighted image of a cervical carcinoma (c), the tumor appears as a slightly hyperintense mass confined within the cervical stroma; on the USPIO-enhanced MRI, the infiltration of the vaginal formix is well depicted (arrows). (Reprinted with permission from [12.27]. © 2004 Lippincott Williams & Wilkins)

GRE images after the intravenous administration of USPIO should be considered a constant and physiological finding that improves tumor conspicuity, allowing more accurate T-staging of neoplastic lesions [12.27].

Prostate cancer and lymph node metastases: In the United States more than 30,000 men died of prostate cancer in 2001 [12.22]. Therefore, the detection of occult lymph node metastases is greatly needed for identifying the disease. In conventional MRI, which is relatively insensitive for the detection of lymph node metastases, lymph nodes were classified as malignant if their diameter exceeded 8–10 mm (see [12.22]).

For the detection of metastases which have not caused an increase in the size of a lymph node (clinically occult disease), superparamagnetic iron oxide nanoparticles were used [12.22]. The intravenously injected nanoparticles are slowly extravasated from the vascular into the interstitial space, from which they are transported to lymph nodes via lymphatic vessels (Fig. 12.8a).

The sensitivity of the detection of lymph nodes with metastases in prostate cancer patients by MRI with lymphotropic superparamagnetic nanoparticles was 90.5% (see Fig. 12.8c) and is significantly higher than that of conventional MRI (sensitivity, 35.4%; see Fig. 12.8b). With MRI using superparamagnetic nanoparticles, metastases less than 2 mm in diameter can be detected. This is below the threshold of detection of any other imaging technique such as positron emission tomography (PET) where the limit of detection is 6–10 mm [12.28].

Arthritis: Rheumatic arthritis (RA) is the most common chronic inflammatory joint disease and a major cause for disability, morbidity, and premature mortality. The initial step in the management of RA is to establish the diagnosis as early as possible in order to prevent irreversible joint damage (see [12.29]). Clinically, RA can be difficult to diagnose in its early stage. Conventional x-rays only show secondary arthritic changes, e.g., bone erosions, late in the course of the disease. Conventional (unenhanced) MRI provides a superior soft-tissue contrast and a direct depiction of the synovium (a membrane in joint cavities secreting lubricating fluid), the initial site of the disease. The MRI contrast enhancement in the synovium by conventional gadopentetate dimeglumine (Gd-DTPA; 547 Da) is, however, limited. Ultrasmall superparamagnetic iron oxide particles (USPIO SHU555C) with a 3.5 nm iron oxide core and a carboxydextran coat (30 nm in diameter) may improve the specificity of MRI for the characterization of inflammation. These nanoparticles may identify inflammatory cell infiltration within the synovium, since they are phagocytosed by macrophages and subsequently cause a marked signal loss in inflammatory tissue on delayed postcontrast T_2 -weighted MR images, 24 h postinjection.

USPIO SHU555C was shown [12.29] to cause in arthritis-induced knees of rats (Fig. 12.9) a substantial, progressive, and positive enhancement of the inflamed synovium on T_1 -weighted gradient-echo (GE) images at 3 min postinjection slowly progressing over time and lasting for at least 2 h. USPIO SHU555C provides a higher difference between the patterns of arthritic and normal joints compared to standard Gd-DFPA because Gd-DFPA shows a higher enhancement in normal joints [12.29].

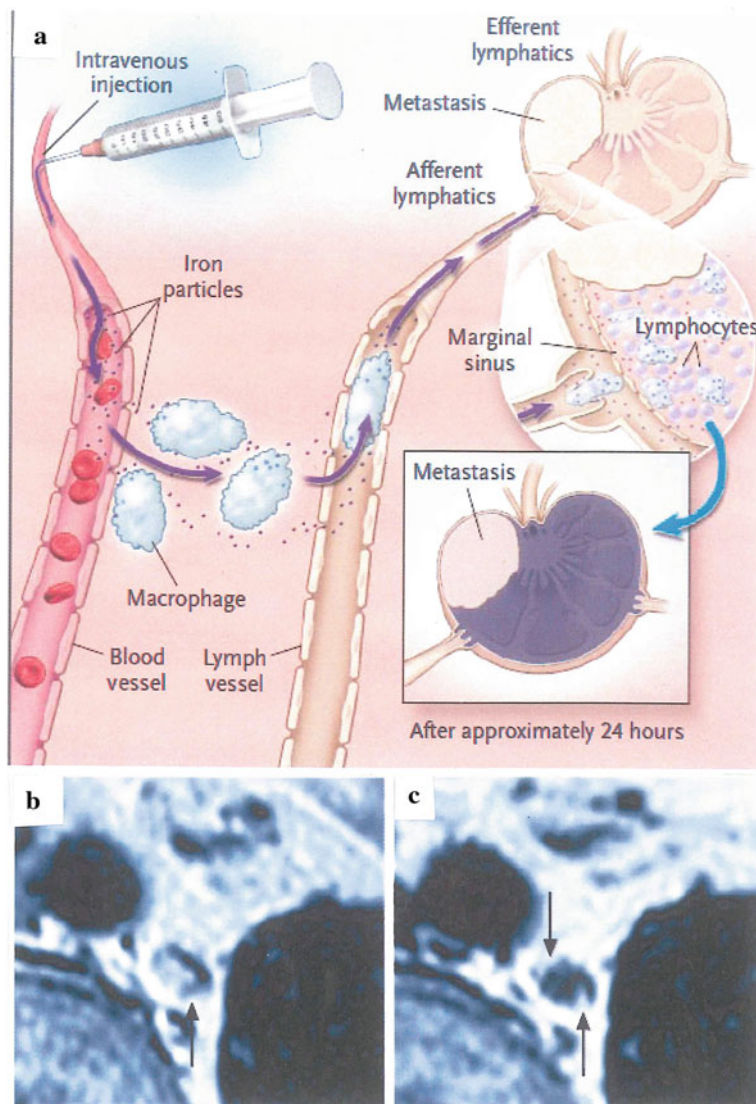


Fig. 12.8 (a) Systemically injected long-circulating nanoparticles gain access to the interstitium and are drained through lymphatic vessels. Disturbances in lymph flow or in model architecture caused by metastases lead to abnormal patterns of accumulation of lymphotropic superparamagnetic nanoparticles, which are detectable by MRI. (b) Conventional MRI shows high signal intensity in a retroperitoneal node with micrometastases (arrow). (c) MRI with lymphotropic superparamagnetic nanoparticles demonstrates two hyperintense foci (arrows) within the node, corresponding to 2 mm metastases. Corresponding histologic analysis confirms the presence of adenocarcinoma within the node. (Reprinted with permission from [12.22]. © 2003 Massachusetts Medical Society)

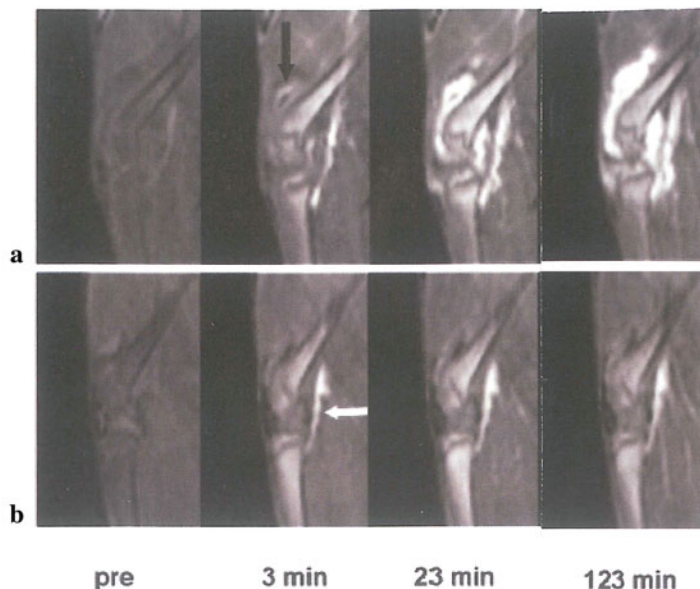


Fig. 12.9 Arthritic (a) and normal (b) knee joint of a rat on T_1 -weighted MR images (magnetic field 2.0 T) before and at various times after injection of the USPIO SHU555C nanoparticles. Minor synovial enhancement can be seen as early as 3 min postinjection (black arrow) which increases over time and persists for at least 2 h. The popliteal artery is indicated by a white arrow. (Reprinted with permission from [12.29]. © 2006 Wiley Interscience)

Arthritis in its earliest stages can be detected by atomic force micrographs (AFM) of the thickening and reduction in elasticity of cartilage fibers [12.30], long before any outward signs appear.

Soft-tissue infection. The role of magnetic resonance imaging (MRI) for detection of macrophage (e.g., white blood cells) phagocytic activity is evolving. It has been shown [12.31] that bacterially induced soft-tissue abscesses in rats can be specifically detected after administration of superparamagnetic iron oxide nanoparticles (USPIO) by T_1 -, T_2 -, or T_2^* -weighted MR imaging (Fig. 12.10). The T_2^* -weighted MR images after USPIO administration show a slightly hyperintense oval center with according to histopathology, necrotic debris. The center is surrounded by an inner hypointense rim, a middle hyperintense ring, and an outer hypointense rim. According to histopathological examination (see [12.31]), the inner and the outer rims represent dense bands of accumulated macrophages within the wall of the tissue, which surrounds the liquified abscess center.

Atherosclerosis and MR angiography (MRA). The composition and stage of atherosclerotic plaques are clinically relevant because of the risk of ischemic events. Atherosclerosis is basically an inflammatory disease. Monocytes adhere to the vascular endothelium and accumulate in lesion-prone arterial sites. Adherent monocytes are subsequently enticed into the arterial intima where they differentiate into macrophages. This suggests that macrophages are a marker of unstable

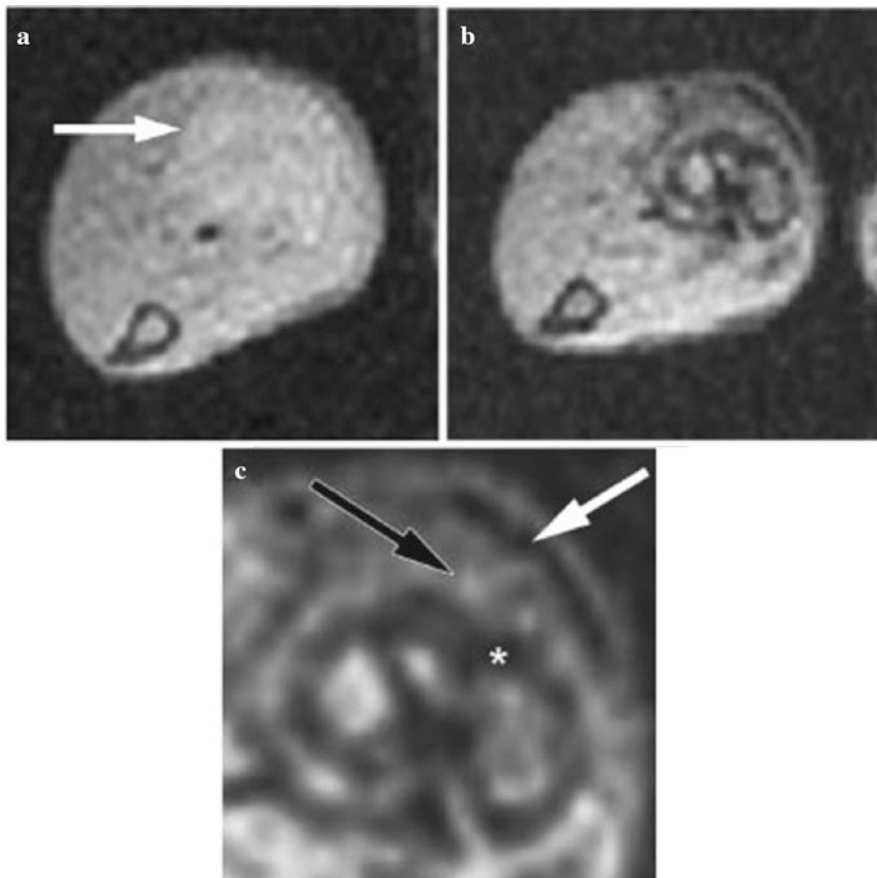


Fig. 12.10 Bacterially induced soft-tissue abscess in the calf of the left hind leg of a rat with high-dose USPIO administration. (a, b) T_2^* -weighted MR images and (c) enlarged view of (b). (a) The image prior to USPIO administration shows a slight hyperintense signal bond (arrow) at the site of the tissue infection. (b) Image of the abscess 24 h after USPIO administration. (c) The enlarged view of (b) (original magnification $2.5\times$) shows three layers of the abscess wall; directly adjacent to the necrotic hyperintense center of the abscess is the hypointense layer (*) followed by a hyperintense middle layer (black arrow) and a hypointense outer layer (white arrow). The hypointense wall layers correspond to higher accumulations of iron oxide-filled macrophages as shown by histologic examination. (Reprinted with permission from [12.31]. © 2005 Radiological Society of North America)

atherosclerotic plaques and that specific targeting of these cells may lead to the characterization of atheromatous plaques prone to rupture [12.21]. Animal studies have shown that superparamagnetic iron oxide nanoparticles induce a focal MRI signal intensity decrease in the aortic wall of atheromatous rabbits (see Fig. 12.11a, b). In coronary, pulmonary, or peripheral angiography, the use of superparamagnetic nanoparticles for MRI has been evaluated [12.21] with both arterial and venous contrast enhancement (see Fig. 12.11c).

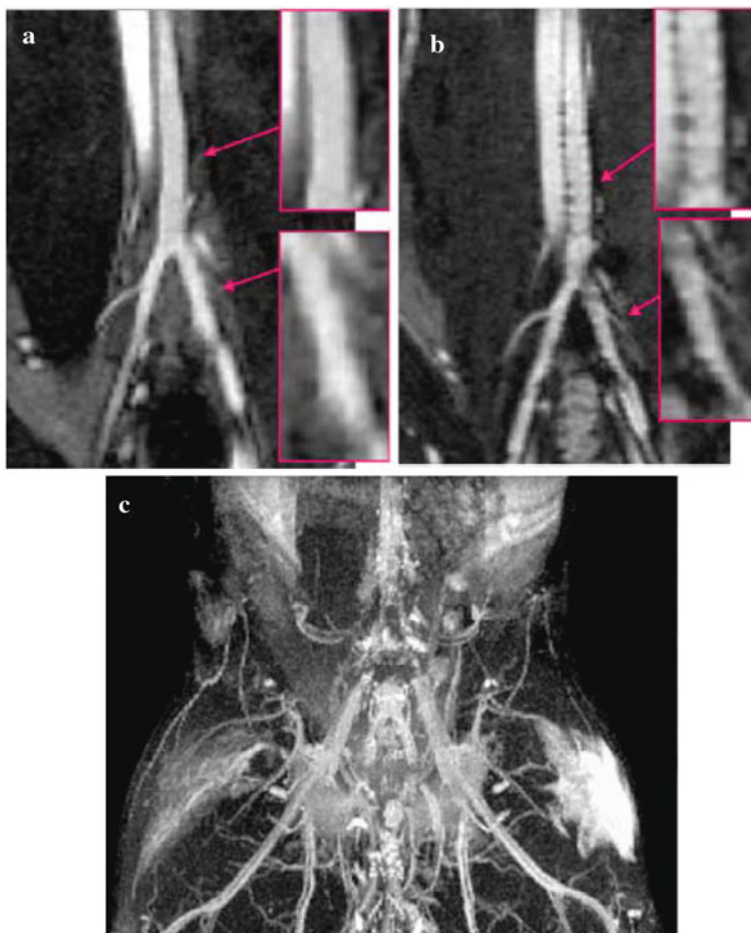
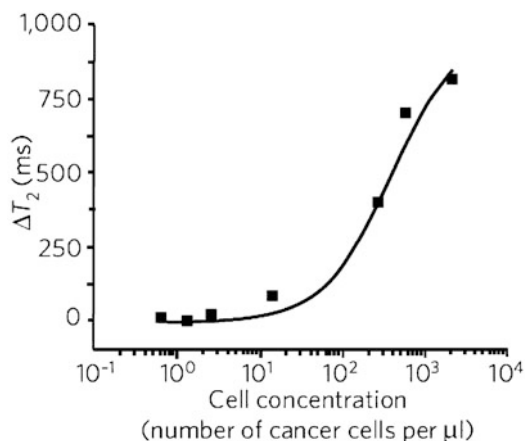


Fig. 12.11 (a, b) Atherosclerotic MRI in rabbits 5 days after injection of superparamagnetic nanoparticles. (a) Normal rabbit: bright blood due to the T_1 effect of the nanoparticles. (b) Atherosclerotic rabbit: note the dark signal in the vessel wall due to the macrophage uptake of the superparamagnetic nanoparticles in atherosclerotic lesions. (c) Angio-MR in a rabbit after injection of superparamagnetic nanoparticles. Even small arteries and veins are visible. (Reprinted with permission from [12.21]. © 2006 Elsevier)

A chip-based diagnostic magnetic resonance imaging (DMR) platform of tumor cells [12.18], using functionalized magnetic nanoparticles as sensors to amplify molecular interactions, can carry out highly sensitive and selective profiling of circulating cells (see Fig. 12.12). The number of circulating tumor cells (CTCs) is a sensitive biomarker for tumor progression and metastasis. Therefore, the quantification of CTCs is emerging as useful for diagnosing and “staging” cancer, for assessing response to treatment, and for evaluating whether there is residual disease [12.18].

Fig. 12.12 Changes of chip-based diagnostic MRI (DMR; change in the time of magnetic relaxation, ΔT_2) of whole blood as a function of the concentration of cancer cells. (Reprinted with permission from [12.18]. © 2008 Nature Publishing Group)



12.2.2 CT Contrast Enhancement

For high-contrast x-ray computed tomography (CT), bismuth sulfide (Bi_2S_3) nanoplatelets (Fig. 12.13) coated with the biocompatible polymer polyvinylpyrrolidone (PVP) and with a hydrodynamic diameter of 30 nm are envisaged. The enhanced x-ray absorption of the coated Bi_2S_3 nanoparticles (five times higher than conventional iodine contrast agents) results in a clear delineation of the cardiac ventricles and all major arterial and venous structures (Fig. 12.14). CT imaging after intravenous administration confirms that the Bi_2S_3 nanoparticles had

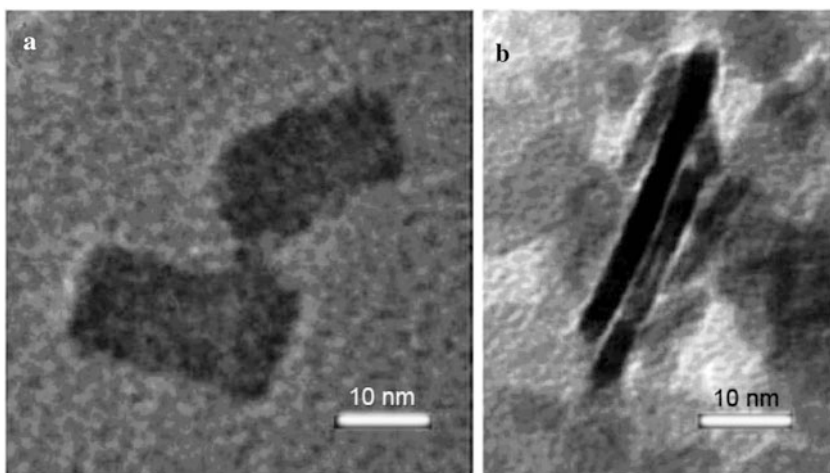


Fig. 12.13 Transmission electron micrograph (TEM) characterization of Bi_2S_3 nanoparticles. (Reprinted with permission from [12.32]. © 2006 Nature Publishing Group)

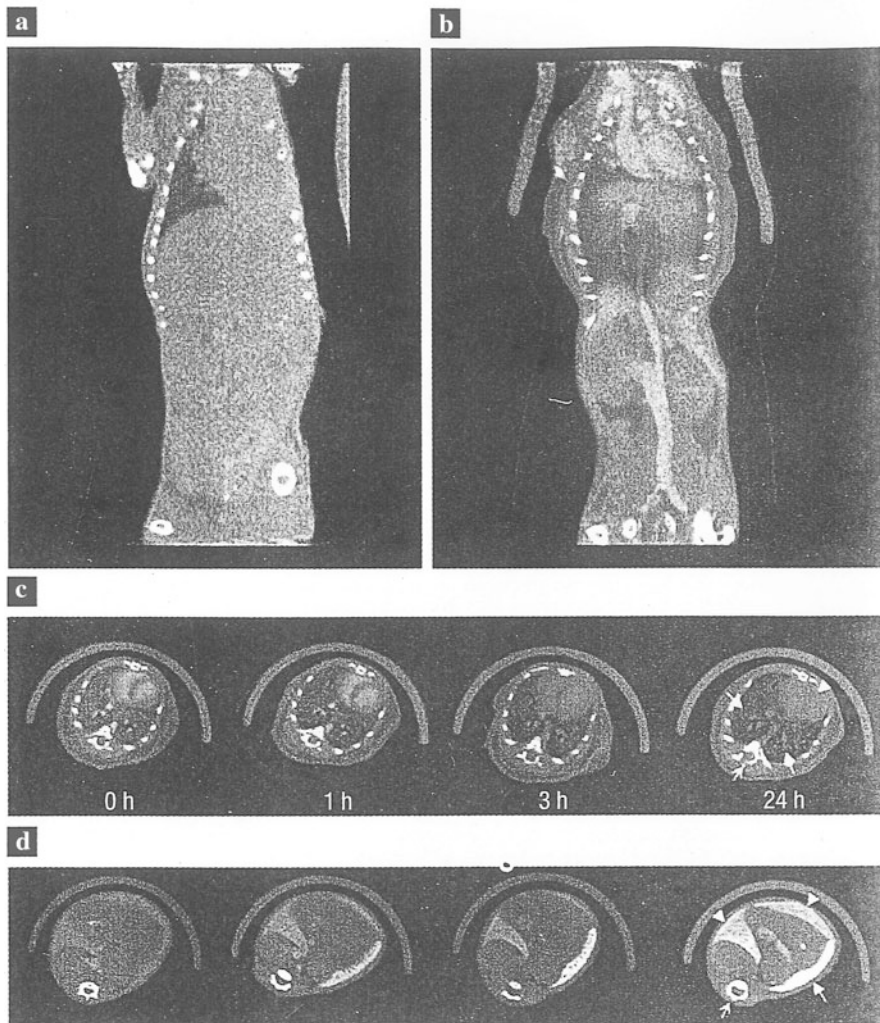


Fig. 12.14 In vivo imaging of vasculature (a, b). Coronal x-ray CT reconstruction of a live mouse before (a) and after (b) intravenous administration of polymer-coated Bi_2S_3 nanoparticles (BPNP), showing large vessels and the heart, and the organ delineation. The length of the reconstruction is 6.5 cm. (c, d) Serial CD scans of a live mouse following tail vein injection of BPNP suspension (0.228 M Bi). Series (c) shows transverse slices through the heart (arrow head), the lungs (solid arrow), and a vertebra (open arrow). Series (d) shows transverse slices including the liver (arrow head), the spleen (solid arrow), and a vertebral body (open arrow). The diameter of the mouse is 1.6 cm. (Reprinted with permission from [12.32]. © 2006 Nature Publishing Group)

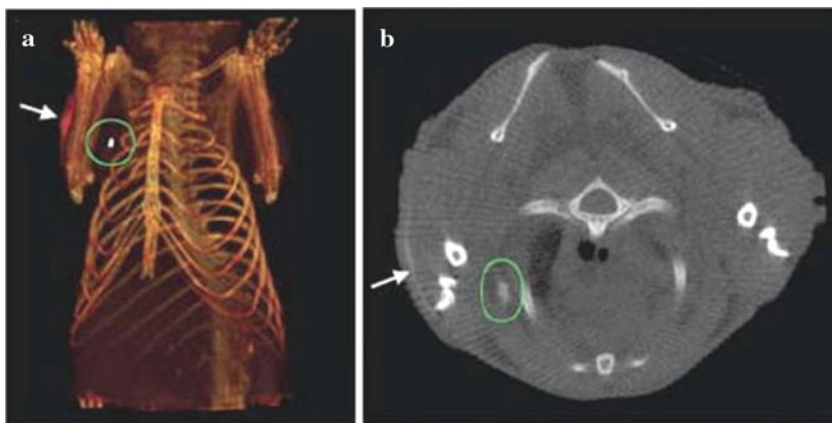


Fig. 12.15 Lymph node CT imaging of a mouse with the Bi_2S_3 nanoparticles imaging agent. (a) 3D volume rendering of the CT data set, 3.8 cm in length. (b) Transverse slice at the height of the lymph node in (a). The maximum diameter of the mouse is 1.8 cm. The position of the lymph node under the right shoulder is indicated by the ovals, and the injection site is shown by the arrows. Note the lack of contrast in the corresponding contra lateral (left shoulder) lymph node. (Reprinted with permission from [12.32]. © 2006 Nature Publishing Group)

distributed to organs containing phagocytic cells (liver, spleen, lymph nodes), reflecting uptake into macrophages, and hepatocytes so that this technique could be used for improved detection of hepatic metastases by CT. It further was investigated whether the Bi_2S_3 nanoparticles could be used for lymph node delivery to improve cancer staging. Lymph nodes in mice were clearly contrasted (Fig. 12.15). In toxicity studies [12.32], polymer-coated Bi_2S_3 nanoparticles showed to be at least one order of magnitude less toxic than free bismuth ions. When administered to human macrophage (U-937) cell lines, the coated Bi_2S_3 nanoparticles showed a toxicity profile similar to that of an iodinated agent in clinical use whereas for the hepatocyte (HepG2) cell line, the Bi_2S_3 nanoparticles showed a profile superior to that of the iodinated agent.

12.2.3 Contrast-Enhanced Ultrasound Techniques

Ultrasound (US) lymphography making use of contrast enhancement by nanobubble suspensions has been demonstrated by *in vivo* studies on dogs as an alternative to current sentinel lymph node detection methods [12.33]. Sentinel lymph nodes can be defined as the first nodes to receive lymphatic drainage from a neoplasm and are therefore at highest risk for regional metastasis through lymphatic spread. Regional lymphatic mapping together with selective lymph node biopsy has gained widespread acceptance as an alternative to radical axillary node dissection in

breast cancer patients due to proven staging accuracy [12.34], reduced perioperative patient anxiety, and lower postoperative morbidity when sentinel nodes are found to be negative for malignancy. When sentinel nodes are found to be free of metastases based on intraoperative section evaluation, the remainder of the lymphatic system is also considered free of metastases and surgery is limited to the excision of the primary tumor.

For the *US lymphography* investigations [12.33], ultrasound contrast formulations were used comprising nitrogen gas nanobubbles encapsulated within a bilayered shell composed of an outer layer of human serum albumin and an inner layer of biodegradable polymer. The contrast uptake in a lymph node following contrast injection is shown in Fig. 12.16. Whereas the lymph node is invisible before contrast administration, it is clearly visible 36 min following the injection of the contrast agent. This documents proof of principle for sentinel node detection using contrast-enhanced power Doppler ultrasound.

The specific mechanism by which the 740 nm nanobubble contrast agent enters the lymphatic system is not so clear. Leaky endothelial junction and fenestrations up to a few microns in width can provide an avenue for particle uptake (see [12.33]). Lymphatic ultrasound contrast enhancement, therefore, may be a compromise between the countervailing constraints for the nanobubble size of entry into the lymphatic system and ultrasound signal intensity.

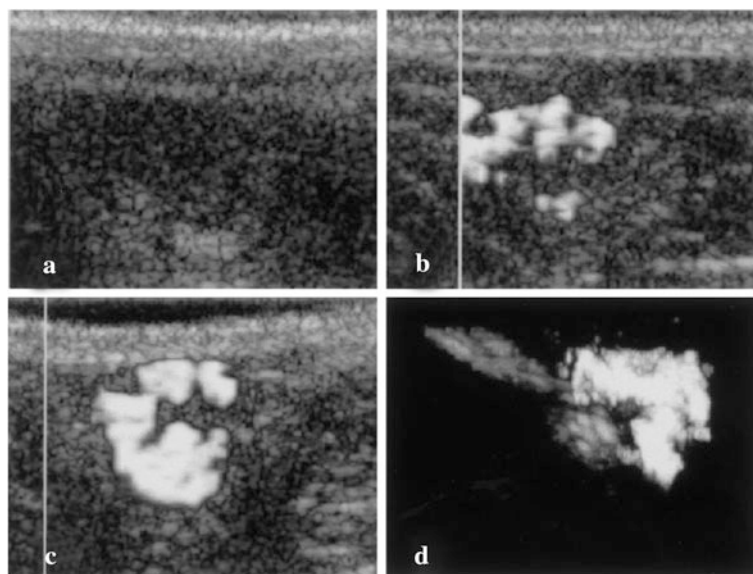


Fig. 12.16 Ultrasound images of a popliteal lymph node of a dog before contrast administration (a) and 5 min (b) and 36 min (c) following subcutaneous injection of a 740 nm nanobubble contrast agent. (d) A 3D rendering of the contrast-enhanced node seen in (c). (Reprinted with permission from [12.33]. © 2003 Lippincott Williams & Wilkins)

Hepatocellular carcinoma (HCC) is a liver cancer disease which accounts for about 400,000 deaths each year worldwide [12.35]. Image-guided percutaneous ablation therapy for HCC is most useful because of its minimal invasiveness, easy repeatability, and cost-effectiveness [12.36]. The recent development of ultrasound contrast agents gave rise to a significant improvement in the diagnostic potential of contrast-enhanced ultrasound (CEUS) in the detection of focal liver lesions. Due to this development CEUS has been stated to be complementary to contrast-enhanced computed tomography (CECT) and magnetic resonance imaging (CEMRI) for pre-treatment staging and assessment of lesion vascularity [12.37]. In Fig. 12.17 a nodule in the liver is imaged by conventional ultrasound and by CEUS making use of an aqueous suspension of phospholipid-stabilized sulfur hexafluoride (SF₆; Sono Vue[®]) as a contrast agent; these images are compared to a CECT study with iodinated contrast media. The sensitivity and accuracy of real-time CEUS in the detection of hepatocellular carcinoma vascularization are shown to have equal diagnostic efficacy as contrast-enhanced CT or MRI.

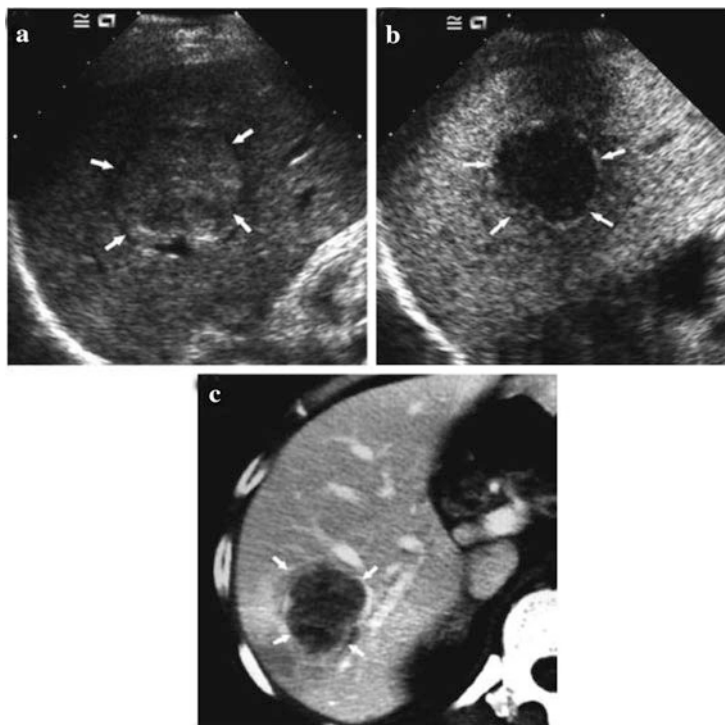


Fig. 12.17 Hepatocellular carcinoma (HCC) in a 46-year old woman. (a) Unenhanced ultrasound imaging shows an isoechoic nodule (diameter 4.1 cm) in the right lobe of the liver; (b) CEUS 170 s after contrast administration showing the HCC which is hypo-echoic with respect to the surrounding liver; (c) contrast-enhanced computed tomography where the nodule is hypo-enhanced with respect to the surrounding liver. (Reprinted with permission from [12.35]. © 2007 Elsevier)

12.2.4 Positron Emission Tomography (PET)

Positron emission tomography (PET) has emerged as a clinical corner stone in cancer staging and is one of the few molecular imaging technologies approved by the Food and Drug Administration (FDA) for imaging of breast cancer, colorectal cancer, esophageal carcinomas, head and neck cancer, lung cancers, melanoma, and lymphoma (see [12.38]). The most frequently used PET agent is $[^{18}\text{F}]$ fluorodeoxyglucose (FDG), a glucose analog that is selectively taken up by cells [12.39]. The proton-rich ^{18}F nucleus (half-life 108.9 min) decays by emission of a positron which is annihilated with an electron in the surrounding tissue, emitting two γ -quanta. By detection of these γ -quanta, the accumulation of the ^{18}F agent in a tumor can be sensitively localized by non-invasive tomography techniques. FDG-PET imaging (Fig. 12.18) is a valuable clinical tool for predicting tumor response to therapy and patient survival [12.40] and was reported to be a more accurate predictor of response to neo-adjuvant chemotherapy than other clinical or histopathological criteria [12.41].

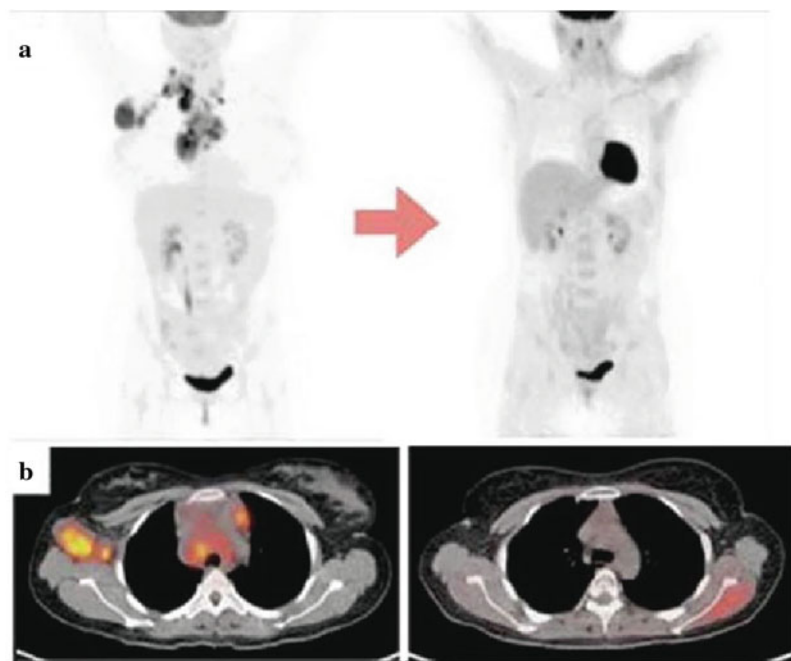


Fig. 12.18 Molecular $[^{18}\text{F}]$ fluorodeoxyglucose positron emission tomography (FDG-PET) imaging used for monitoring of tumor patient response to therapy. (a) FDG-PET scan of a patient with a tumor of lymphoid tissue before (left) and after (right) treatment. (b) Corresponding axial PET-CT sections show a decrease in FDG activity (yellow red) in axilla and mediastinum after treatment. (Reprinted with permission from [12.38]. © 2006 AAAS)

Molecular imaging techniques, such as FDG-PET, may lower costs by reducing the number of patients eligible for a given treatment combination. In some settings, molecular imaging techniques may eliminate costly surgical procedures altogether. In preliminary studies, FDG-PET imaging has been shown to have a high benefit/cost ratio for cancer staging (see [12.38]).

Alzheimer's disease in its early stages can be diagnosed by PET which can be used for detecting neurodegenerative diseases that produce significant alterations in brain functions. Recent developments in small animal imaging provide PET images with a resolution of 1–2 mm [12.42]. By employing Gd-orthosilicate (GSO) [12.43] and lutetium oxyorthosilicate (LSO) [12.44] crystals as γ -detectors, resolutions of 3 mm have been obtained in the human brain. Even in patients with mild impairment, by the time the patient presents with symptoms of neurodegenerative dementia such as Alzheimer's disease, substantial alteration of cortical metabolic function generally has occurred. The associated decrease in glucose metabolism in certain brain areas are readily detectable on FDG-PET images (Fig. 12.19). The sensitivity and specificity for detecting Alzheimer's disease by PET were 92% and 71% as confirmed histopathologically. Even early Alzheimer's disease can be detected with PET due to regional cerebral metabolic changes with an accuracy exceeding 80% (see [12.45, 12.46]). Relative hypometabolism of the associative cortex can be accurately used to predict whether cognitive decline will occur at a rate faster (characteristic for Alzheimer's disease) than for normal aging (see [12.45]). There is also research underway for studying cerebrovascular diseases [12.47].

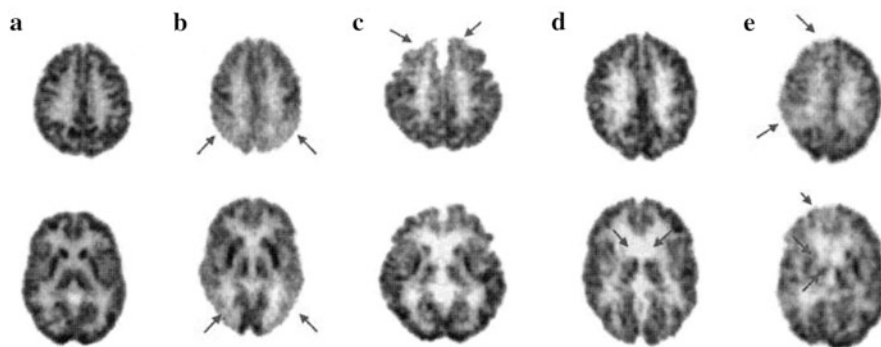


Fig. 12.19 Normal and abnormal patterns of $[^{18}\text{F}]$ fluorodeoxyglucose (FDG) distribution. Positron emission tomography (PET) data are displayed with inverse gray scale, with darkness level of each pixel linearly related to radioactive counts per second. Planes are shown at high-(top row) and mid- (bottom row) transaxial levels for subjects with (a) a normal metabolic brain pattern, (b) posterior hypometabolism characteristic of early Alzheimer disease, (c) anterior hypometabolism characteristic for early frontal lobe dementia, (d) profound striatal hypometabolism characteristic of Huntington's disease, and (e) distributed foci of right-sided hypometabolism in cortical and subcortical structures, characteristic of multiple infarcts in tissue supplied by the right carotid artery. (Reprinted with permission from [12.45]. © 2005 Elsevier)

For the emerging field of molecular imaging, the combination of imaging approaches, i.e., simultaneous MR/PET imaging [12.48] or CT/PET fusion images [12.49] may be of future clinical interest.

12.2.5 Raman Spectroscopy Imaging

By this technique of inelastically scattered photons, highly specific analysis of molecular distributions, of pharmacokinetics, or of targeted drug delivery can be obtained. The sensitivity can be strongly enhanced by surface-enhanced Raman scattering (SERS) [12.50], which is a plasmonic effect (see Sects. 1.7 and 7.6) where molecules absorbed on a noble metal surface or on a nanoparticle experience a dramatic increase in the incident electromagnetic field, resulting in a high Raman intensity. SERS nanoparticles with a gold nanocore, a Raman-active molecular layer, and a silica coating (Biotags) are commercially available [12.51]. Single-walled carbon nanotubes (SWNTs) exhibit a strong Raman peak at 1593 cm^{-1} and do not use a metal surface enhancer. Near-infrared Raman excitation is ideal for penetration into biological tissue.

After injection of Biotag nanoparticles into living mice, an accumulation of the nanoparticles in the liver was observed (see Fig. 12.20a). When SWNTs were conjugated with arginine-glycine-aspartate (RGD) peptide for targeting them to an integrin-positive U87 MG tumor in living mice, a much higher SWNT concentration is demonstrated to be in the tumor by Raman scattering than without conjugation (see Fig. 12.20b).

12.2.6 Photoacoustic Tomography

This is a non-ionizing, non-invasive *in vivo* imaging technique (see [12.52]) where short 800 nm near-infrared (NIR) laser pulses for deep penetration (5 cm) into biological tissue induce a small temperature rise ($<5\text{ mK}$) in the tissue due to absorption which causes thermoelastic expansion and the emission of photoacoustic waves. These signals can be detected by a transducer (see Fig. 12.21a) and stored in a computer for image reconstruction by a back-projection algorithm, yielding images with a spatial resolution of $\sim 60\text{ }\mu\text{m}$ (see [12.52]). The injection of 50 nm gold nanocages with a strong 800 nm plasmon absorption (see Fig. 12.21b, c) into the circulatory system of a rat gives rise to a significantly enhanced contrast in the images of the rat's brain vasculature (see Fig. 12.22a–c).

12.2.7 Biomolecular Detection for Medical Diagnostics

Molecularly targeted agents are expected to broadly expand the capabilities of conventional anatomical imaging methods. Molecular detection will allow clinicians

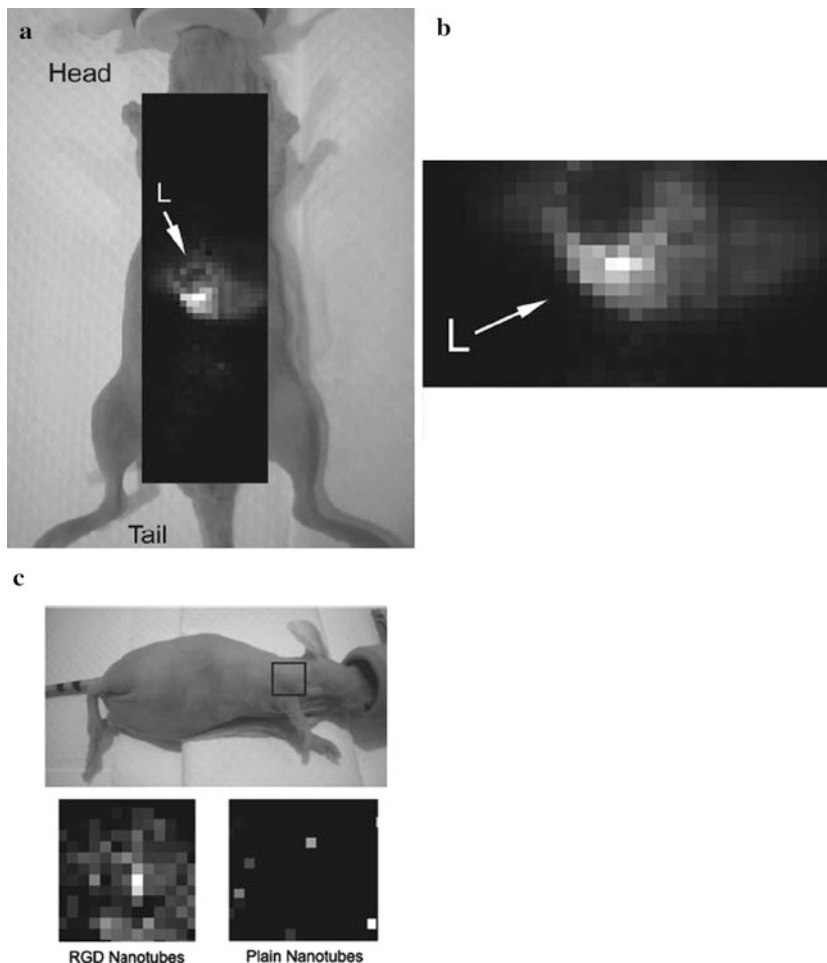


Fig. 12.20 (a) Whole-body raster-scan image (1 mm steps) of a nude mouse 2 h after tail vein injection of surface-enhanced Raman scattering (SERS) nanoparticles. The highest SERS concentration is accumulated in the liver (L; arrow). (b) Map of liver (0.75 mm steps), showing higher definition of the liver (arrow). (c) Accumulation of arginine-glycine-aspartate (RGD) peptide conjugated single-walled carbon nanotubes (SWNTs) within an integrin-positive U87 MG tumor model at 24 h after injection. Photograph of the mouse depicting the tumor area (black square) and corresponding Raman images at 24 h after SWNT injection by raster scan with 750 μ m steps. Notice the accumulation of the RGD SWNTs in the tumor area as opposed to the unconjugated SWNTs (plain) that show little to no accumulation in the tumor. (Reprinted with permission from [12.51]. © 2008 National Academy of Sciences USA)

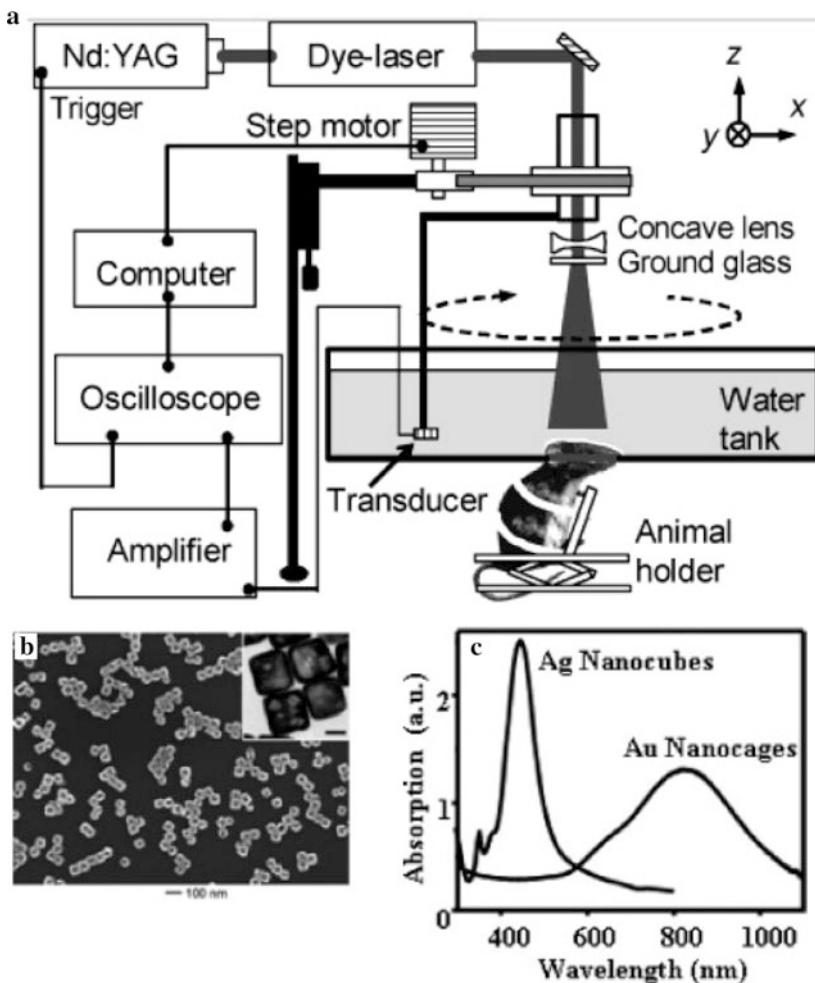


Fig. 12.21 (a) Schematic of the non-invasive photoacoustic tomography (PAT) of a rat brain in vivo for employing Au nanocages contrast agent and near-infrared (NIR) light [12.52]. (b) Scanning electron micrograph of Au nanocages prepared by a galvanic replacement reaction between Ag nanocubes and HAuCl_4 solution. The *inset* shows a transmission electron micrograph of Au nanocages, scale bar: 25 nm. (c) Absorption spectra of Ag nanocubes and Au nanocages. (Reprinted with permission from [12.53]. © 2007 American Chemical Society)

not only to see where a tumor is located in the body but also to visualize the expression and activity of specific molecules (e.g., DNA, RNA, or proteins [12.54]) and biological processes (e.g., apoptosis, angiogenesis, or metastasis) that influence, e.g., tumor behavior and response to therapy. The hope is that clinical molecular analysis will one day be used to detect physiological alterations due to a disease, such as cancer, when it is still at a curable stage, to adjust treatment protocols

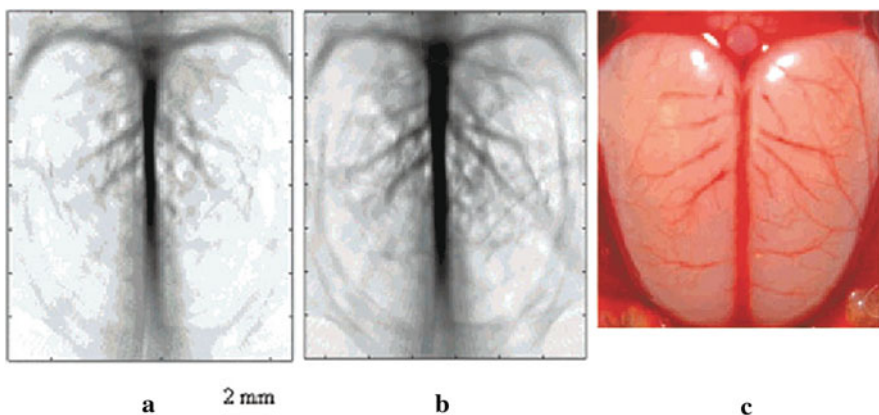


Fig. 12.22 Non-invasive photoacoustic tomograph of a rat's cerebral cortex (a) before the injection of Au nanocages and (b) about 2 h after the injection of Au nanocages. (c) An open-skull photograph of the rat's cerebral cortex. (Reprinted with permission from [12.53]. © 2007 American Chemical Society)

in real time, and to streamline the drug development process [12.38]. An example for a single molecule biomarker for a disease is the prostate-specific antigen (PSA) protein, which is elevated in men with prostate cancer, and researchers seek to find new biomarkers for various diseases. Therefore, characterizing the human plasma proteome is the main goal in proteomics, which is the research to understand the expression and function of proteins on a global level. The blood plasma not only contains the resident proteins but also immunoglobulins (antibodies in the immune response for binding the specific antigens), protein hormones, secreted proteins, foreign proteins, indicative of infection, and proteins from dying cells. Thus, the detailed understanding of the blood plasma proteome will make it possible to relate individual serum proteome profiles to the genome, environments, and lifestyles of individuals and, therefore, will reveal predisposition to, or onset of, disease [12.55].

For diagnostic technologies it is of relevance that the concentration range of the different proteins is of the order of 10^9 , with serum albumin being most abundant (30–50 mg/ml) and low-level proteins such as interleukin-6 present at < 5 pg/ml. The focus of detection should be directed at the less abundant fraction of proteins in the blood plasma, as it is this fraction that best reflects tissue physiology and pathology, as these are the non-resident proteins that are either actively or passively released from tissue into the blood stream [12.55].

Primary examples for emerging nanotechnology approaches in biomolecular detection for medical diagnostics include nanostructured surfaces for the enhancement of proteomic analysis via mass spectrometry (MS), the bio-barcode method for the amplification of protein signatures via the use of a two-particle assay, nanowires as biologically gated transistors, and silicon cantilevers for the mechanical recognition of biomolecular ensembles [12.56] as reported in the following.

Nanostructured surfaces for proteomic analyses via mass spectrometry (MS). Mass spectrometry (MS) is currently the standard for protein expression profiling of biological fluids and tissues [12.56–12.58], with mounting evidence that matrix-assisted laser deposition/ionization time-of-flight (MALDI-TOF) MS can be employed for early detection of malignant diseases. It is hypothesized that the low-molecular-weight proteome (LMWP), comprising proteolytic fragments at extremely low concentrations, contains a wealth of information of diagnostic and prognostic utility. Nanoporous silicon oxide surfaces (Fig. 12.23a) are charged with a diluted human plasma sample to separate the low-molecular-weight (LMW) proteins/peptides from the less interesting high-molecular-weight (HMW) proteins. The LMW fraction is then analyzed in a MALDI-TOF experiment, yielding a mass spectrum (Fig. 12.23b) characteristic for peptide amounts down to the nanogram per milliliter range, which is roughly 400-fold more sensitive than conventional MS analysis. The technique can be improved by chemical and structural surface “tailoring” for a selective enrichment of specific protein/peptide classes. High-throughput MALDI-TOF MS of LMW-enriched plasma is a strategy to rapidly screen and profile a large number of samples, in the search of disease-related biomarkers. The limitations in sensitivity of protein-based molecular profiling due to the lack of PCR-like reactions (PCR – polymerase chain reaction) can be overcome by the bio-barcode assay (see below). The PCR technology allows for the duplication of portions of prospective targets and represents the ultimate in sensitivity but has significant drawbacks including complexity, sensitivity to contamination, cost, and lack of portability and major challenges with respect to multiplexing (detecting multiple targets in a single assay) [12.12].

The bio-barcode assay. This assay [12.56, 12.59] utilizes two types of particles for sample purification, detection, and amplification. The first is a microparticle with a recognition agent that in the case of nucleic acids is an oligonucleotide which is complementary to a statistically unique region of the target and, in the case of proteins, a monoclonal antibody. The second particle is a nanoparticle with a recognition agent that can sandwich the target with the microparticle (Fig. 12.24a). In addition, the nanoparticle carries hundreds of 15 – 20-mer oligonucleotides referred to as barcodes, allowing the user to pair a unique barcode with every conceivable recognition agent, since for a 20-mer there are 4^{20} unique combinations. Once the two particles have sandwiched the target, a magnetic field can be used to separate the complexed target from the sample solution. Release of the barcodes in a buffer is effected chemically (see [12.58]) and the barcodes can be identified with a high-sensitivity detection system, e.g., scanometrically (Fig. 12.24a). The scanometric method has provided the lowest limit of detection to date for both nucleic acid (high zeptomolar, 10^{-21} M) and protein targets (low attomolar, 10^{-18} M) (Fig. 12.24b). The good amplification of the technique is due to the high ratio of barcode to target recognition elements. In addition, it has high-sensitivity barcode sorting and sensing capabilities through the chip-based scanometric method. The barcode detection system allows one to detect nucleic acids close to the sensitivity of PCR without the need of complicated enzymatic processes. It may have, however, its most significant scientific and clinical impact in protein marker-based

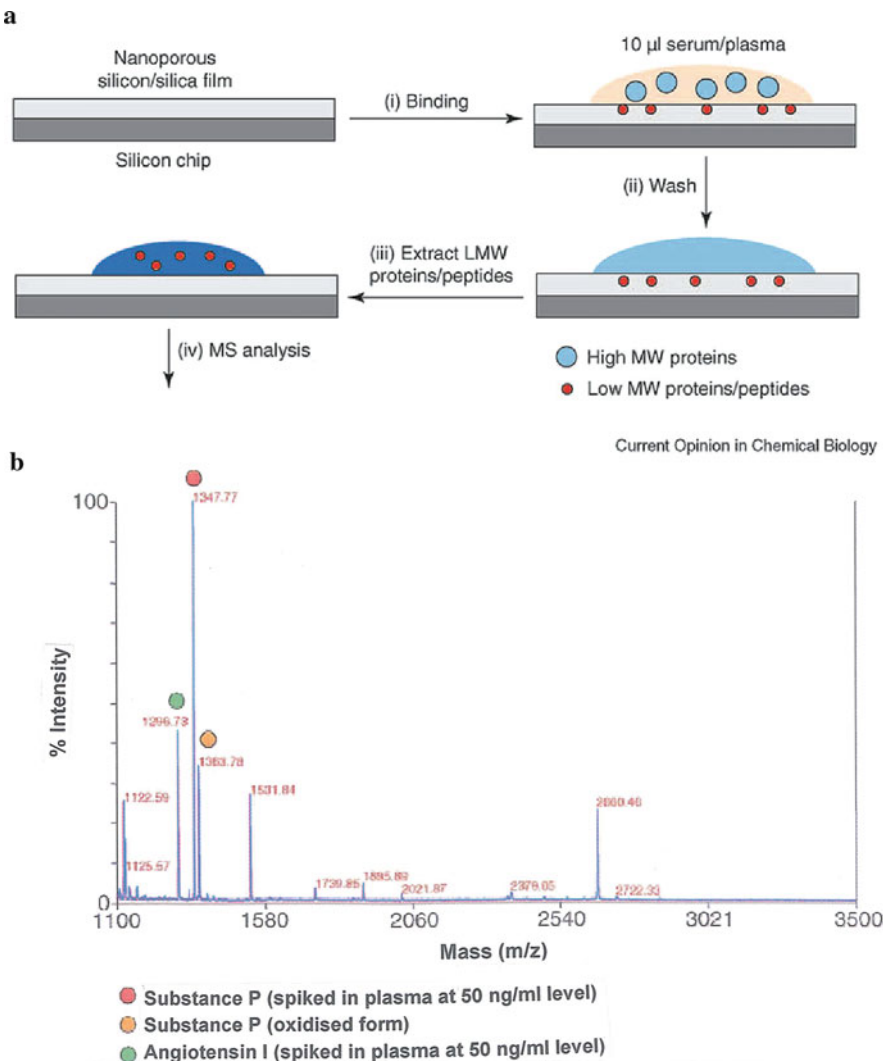


Fig. 12.23 (a) Procedure for low-molecular-weight (LMW) protein harvesting from plasma/serum with the capturing strategy on nanoporous surfaces. (i) Incubation of serum with nanoporous silica film; (ii) Washing of unbound substances; (iii) Release of LMW proteins by appropriate extraction solutions; (iv) MS analysis. (b) Mass spectrum of LMW peptides extracted by nanoporous harvesting of a 10 μ l human plasma sample. Standard peptide substance P and angiotensin I were spiked into the plasma at a 50 ng/ml level. (Reprinted with permission from [12.56]. © 2006 Elsevier)

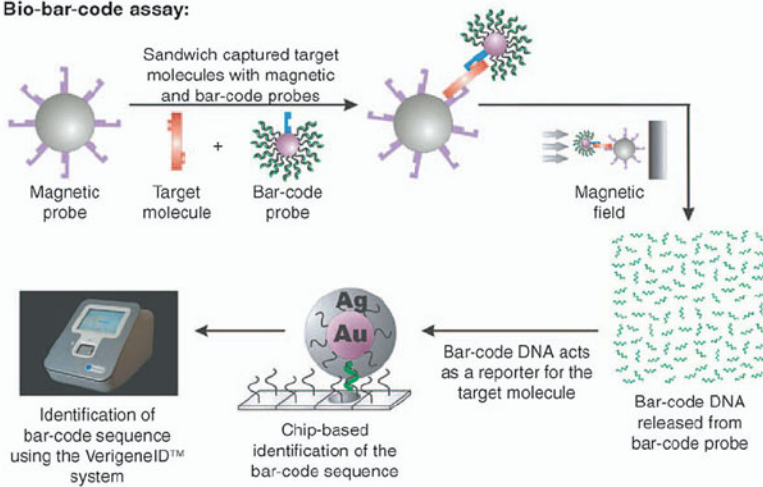
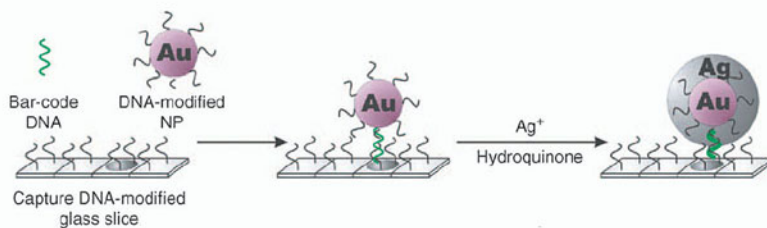
diagnostics because it is 10^6 times more sensitive than enzyme-linked immunosorbent (ELISA)-based technology. This offers (i) the ability to use new markers of low concentration for various types of diseases, (ii) the ability to use known markers via less invasive means, and (iii) the ability to use existing markers to sensitively

evaluate disease recurrence. An example is the use of the barcode assay to identify amyloid-derived diffusible ligands (ADDL, a marker initially linked to Alzheimer's disease in brain studies) in cerebral spinal fluid samples of Alzheimer patients [12.59]. This was the first time the ADDLs were identified in fluids outside the brain and, importantly, preliminary data showed a correlation between ADDL concentration and progression of the disease. Furthermore, the barcode assay is being evaluated for the early detection of the recurrence of prostate cancer after surgery because of its detection level much lower than in conventional tests (Fig. 12.24b). The barcode assay has also been used for serum-based prion detection in bovine spongiform encephalopathy (BSE; "mad cow disease").

Nanowires: label-free electronic sensors of genes and proteins. Semiconductor nanowire sensors operate on the basis that the change in chemical potential accompanying a target analyte binding event, such as DNA hybridization (the process whereby two complementary nucleic acid strands form a double helix), can act as a field-effect gate upon the nanowire, thereby changing its conductance. This is similar, in principle, to how a field-effect transistor operates. By superlattice nanowire pattern transfer (SNAP), large arrays of Si nanowires can be produced (Fig. 12.25a). Large-scale circuits can be constructed within very small (microfluidics) environments, thereby enabling measurements on large numbers of different genes and proteins from very small tissue samples, or even single cells [12.61]. The potential for both biological research and clinical applications is large. However, encoding the individual nanowires with single-stranded DNA (ssDNA) molecules or protein capture agents represents a serious challenge. Electrochemical methods have been applied to encode selected nanowires with proteins (see [12.56]). Data from Si nanowire sensors are shown in Fig. 12.25b which demonstrate the broad dynamic range (10^6) of sensing the nanowires can attain. Libraries containing up to 24 individual nanowire sensors have been constructed, and it should be possible to extend these libraries to 10^3 - 10^5 elements [12.62] for rapid, high-throughput highly multiplexed biomolecular detection.

Cantilevers: nanomechanical detection of biological molecules: It has been demonstrated that molecular adsorption to nanomechanical systems results in measurable mechanical forces which offers an exciting opportunity for the development of highly sensitive, miniature, and label-free biological sensors [12.63–12.65]. For example, micron-sized silicon cantilever beams undergo bending due to surface stresses created by single-side molecular adsorption. The molecular mass loading gives also rise to a variation of the cantilever's resonance frequency. These variations can, e.g., be measured optically or piezoresistively. The cantilevers can be cost-effectively mass-manufactured. Selective chemical recognition of target molecules is achieved by affinity binding reactions, where the cantilever is coated with self-assembled monolayers, DNA probes, antibodies, or peptides. The mechanical stresses bending the cantilever originate from the changes of the free energy by specific binding of biomolecules. Non-specific interactions of biomolecules do not cause cantilever bending (see [12.56]).

DNA hybridization on a cantilever coated with thiol-modified ssDNA probes (20-mers) gives rise to a bending of the cantilever [12.66, 12.67] (Fig. 12.26). The

a Bio-bar-code assay:**Scanometric method:****b**

	Concentration	Targets/50uL	Targets/diseases
10^{-3} = Millimolar	$\sim 3 \times 10^{16}$		Colorimetric/ enzymatic chemistry blood sugar (diabetes)
10^{-6} = Micromolar	$\sim 3 \times 10^{13}$		
10^{-9} = Nanomolar	$\sim 3 \times 10^{10}$		ELISA/ chemiluminescence Tropomin, CK-MB, BNP, β HCG
10^{-12} = Picomolar	$\sim 3 \times 10^7$		
10^{-15} = Femtomolar	$\sim 3 \times 10^4$		
10^{-18} = Attomolar	~ 30		
10^{-21} = Zeptomolar	~ 0.3		
			Bio-barcode technology Alzheimer's disease, nvCJD (Mad Cow), Ovarian, Breast and other cancers, Anthrax, HIV, Ebola, Small Pox

Fig. 12.24 (a) General bio-barcode assay scheme. A magnetic particle captures a target using either monoclonal antibodies (for proteins) or complementary oligonucleotides (for nucleic acids). Target-specific Au nanoparticles are conjugated to the target and account for target identification

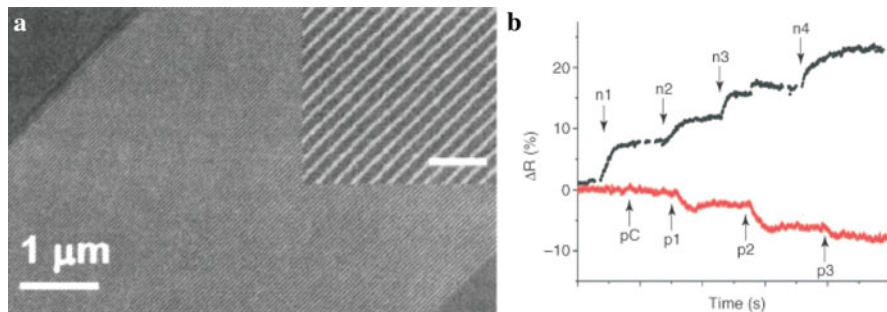


Fig. 12.25 (a) 128 12 nm wide Si wires. The *inset* reveals the structural fidelity of the nanowires at a higher resolution (scale bar, 150 nm) [12.60]. (b) Sensing results from n-type (*top*) and p-type Si nanowire sensors, demonstrating the sensitivity in the attomolar (10^{-18} M) range in buffer. The time axis is 0–600 s for n-type and 0–1400 s for p-type sensors. The nanowire sensing elements were coated with ssDNA, and oligonucleotides were flowed over the nanosensors using microfluidics. The various points indicated are n1 = 220 attoM cDNA; n2 = 22 femtoM cDNA; n3 = 2.2 picoM cDNA; n4 = 220 picoM cDNA; pC = 22 nanoM non-complementary ssDNA; p1 = 220 attoM cDNA; p2 = 22 femtoM cDNA; p3 = 2.2 picoM cDNA. Both p- and n-type nanosensors exhibit sensitivity over a broad dynamic range, with the response scaling logarithmically with concentration. (Reprinted with permission from [12.56]. © 2006 Elsevier)

extent of cantilever bending varies as a function of the length of the complementary ssDNA. The cantilever deflection is attributed to a reduction in surface stress due to conformational changes caused by double-stranded DNA formation.

The detection of proteins depends on reproducible and robust immobilization techniques for antibodies. Antigens successfully detected on cantilevers include PSA, and the biowarfare agents ricin and tularemia [12.68, 12.69]. Upon exposure to antigens, the antibody-immobilized cantilevers undergo bending, with the bending amplitude proportional to concentration and time of exposure. Mechanical label-free detection, although in its early days, has the potential as a platform for sensitive multiplexed sensors for biomolecules [12.56]. Microcantilevers were introduced for detecting prostate-specific antigen (PSA) at clinically relevant concentrations [12.70] and for detecting BRCA1 gene mutations [12.71].

Molecular cancer diagnosis. Semiconductor nanoparticle (quantum dots – QD) probes allow sensitive imaging of cancer cells in living animals. The use of near-infrared-emitting QDs should improve both the tissue penetration depth and

Fig. 12.24 (continued) and amplification. The barcode oligonucleotides are released and detected using the scanometric method. The target can be DNA, RNA, or protein. The Verigene ID™ is a commercial instrument (<http://www.nanosphere-inc.com>). (b) Biomolecule detection technology. The bio-barcode assay provides access to a target concentration range well below that of conventional enzyme-linked immunosorbent assays (ELISA). This ultrasensitivity provides the ability to utilize new, low-concentration markers for disease screening, or biodiagnostics. (Reprinted with permission from [12,56]. © 2006 Elsevier)

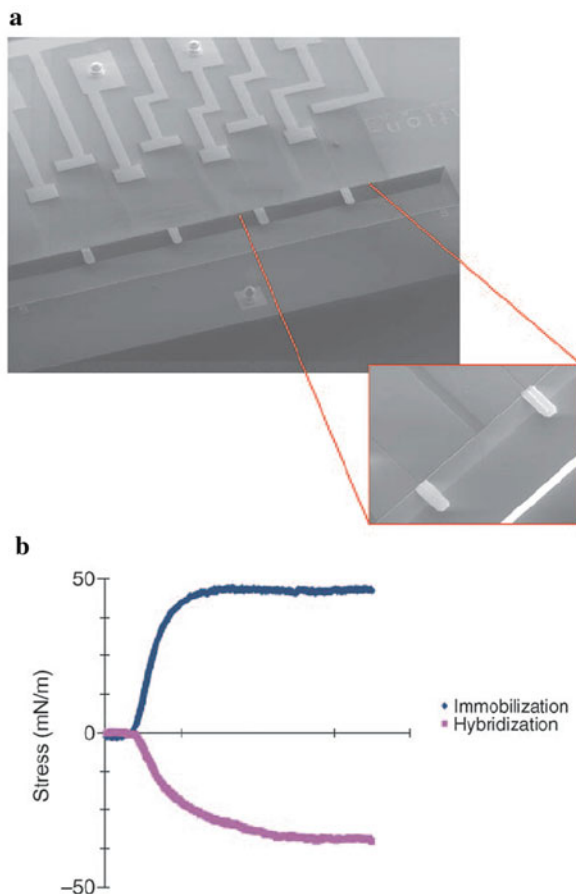


Fig. 12.26 Nanocantilevers for ssDNA detection. (a) An array of piezoresistive cantilevers in a fluidic well (Cantion Inc.). The cantilevers are 120 μm long and are separated by 470 μm . (b) Cantilever surface stress variation as a function of ssDNA probe (20-mer) immobilization and hybridization of fully complimentary 20-mers using a piezoresistive array. (Reprinted with permission from [12.56]. © 2006 Elsevier)

imaging sensitivity. Agents making use of QDs might be used for non-invasive diagnosis and treatment of cancer [12.72].

Bioconjugated QD probes have been developed for *in vivo* targeting and imaging of human prostate cancer cells growing in mice. This class of QD conjugates contains a triblock copolymer for *in vivo* protection, targeting ligands for tumor antigen recognition and multiple polyethylene glycol (PEG) molecules for improved biocompatibility and circulation [12.72]. The core–shell CdSe–ZnS QDs (2.5 nm radius) were covered with a 1 nm tri-*n*-octylphosphine oxide (TOPO) layer, a 2 nm thick polymer coating, and a 4–5 nm PEG antibody layer (Fig. 12.27a, b). Under *in vivo* conditions, QD probes can be delivered to tumors by both passive and active

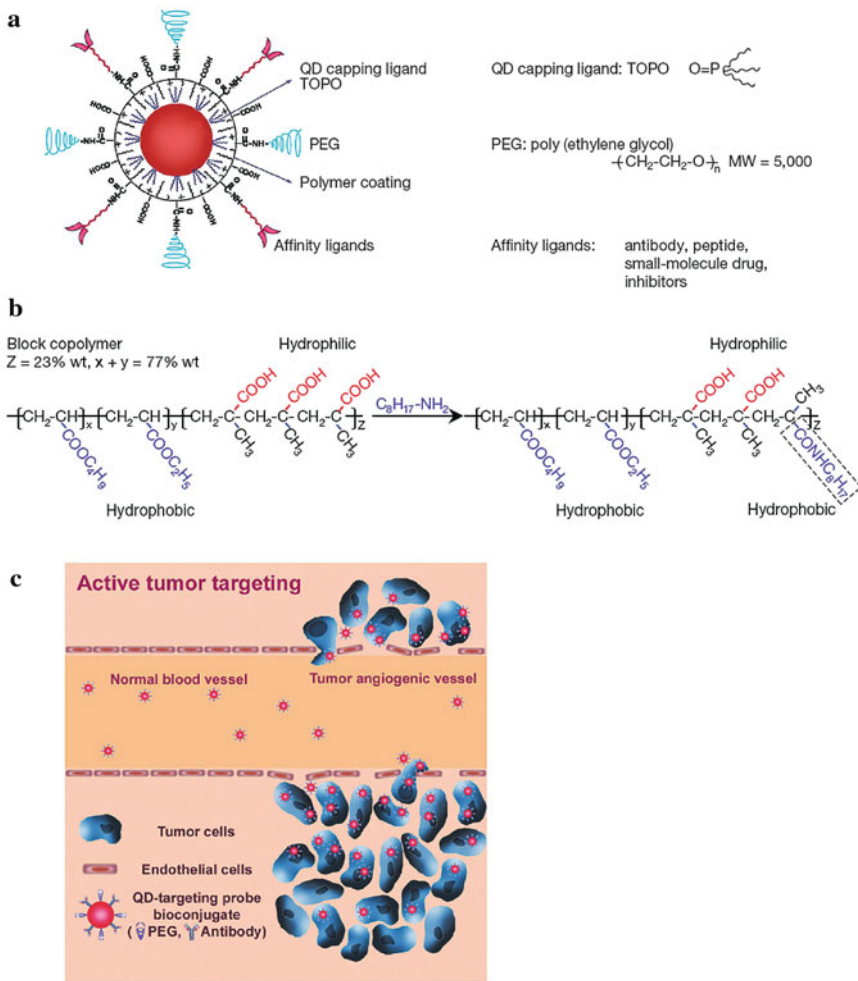


Fig. 12.27 Schematic of bioconjugated QDs for in vivo cancer targeting and imaging. **(a)** Structure of a multifunctional QD probe showing the capping ligand TOPO, an encapsulating copolymer layer, tumor-targeting ligands (peptides or antibodies), and PEG. **(b)** Chemical modification of a triblock copolymer with an 8-carbon side chain which interacts strongly with TOPO. **(c)** Permeation and retention of QD probes via leaky tumor vasculatures (passive targeting) and high-affinity binding of QD-antibody conjugates to tumor antigens (active targeting). (Reprinted with permission from [12.72]. © 2004 Nature Publishing Group)

targeting mechanisms (Fig. 12.27c). In the passive mode, nanometer-sized particles accumulate preferentially through an enhanced permeability and retention effect due to the hyperpermeabilization of the tumor-associated neovasculature and due to the lack of an effective lymphatic drainage system in the tumor. QD probes conjugated to a specific monoclonal antibody (Ab) exhibit a strong and specific binding to a

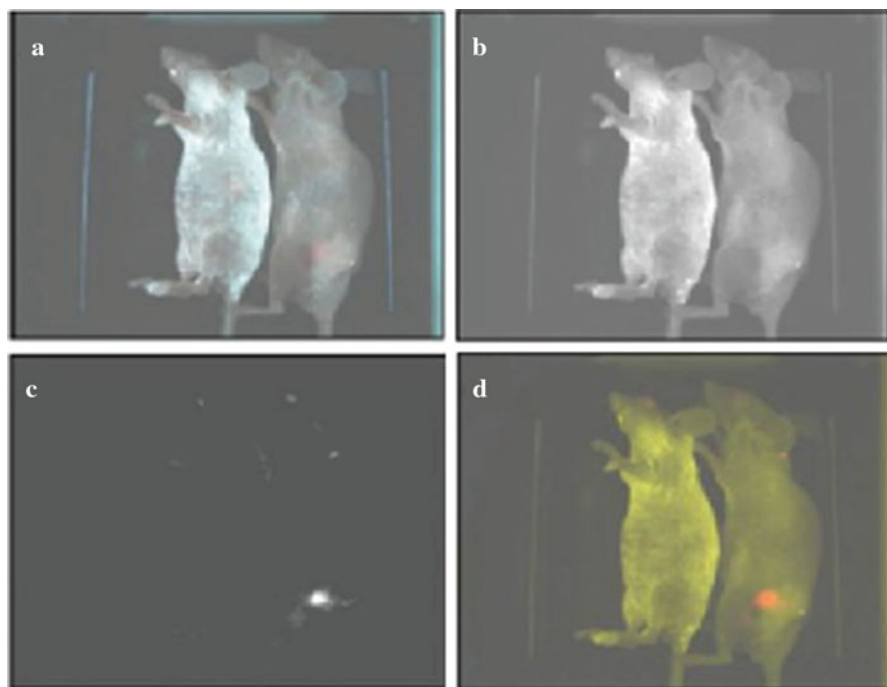


Fig. 12.28 Spectral imaging of QD-PSMA Ab conjugates in live mice harboring C4-2 human prostate tumor xenografts. Orange-red fluorescence signals indicate a prostate tumor growing in a live mouse (*right mouse*). Control studies using a healthy mouse (no tumor) and the same amount of QD injection showed no localized fluorescence signals (*left mouse*). **(a)** Original image; **(b)** unmixed autofluorescence image; **(c)** unmixed QD image; and **(d)** superimposed image. After *in vivo* imaging, histological and immunocytochemical examinations confirmed that the QD signals came from an underlying tumor. Note that QDs in deep organs such as liver and spleen were not detected because of the limited penetration depth of visible light. (Reprinted with permission from [12.72]. © 2004 Nature Publishing Group)

human prostate cancer cell line, C4-2, which is known to express prostate-specific membrane antigen (PSMA) on the cell surface.

Figure 12.28 depicts spectral imaging results obtained from QD-PSMA Ab probes injected into the tail vein of a tumor-bearing mouse (*right mouse*) and a control mouse (no tumor, *left mouse*). The original image (a) shows QD signals at one tumor site among an autofluorescence background of the mouse skin. Using spectral unmixing algorithms, the background signals (b) and the QD signals (c) were separated. The composite image (d) shows the tumor site in the whole animal.

The QD probes, which are highly stable *in vivo*, appear 10–20 times brighter than organic dyes. Due to the PEG shielding they circulate in blood for as long as 48–72 h. For deep tissue imaging (millimeters to centimeters) the use of far-red and near-infrared emitting QD in the spectral range 650–900 nm are required.

This wavelength provides a “clear” window for in vivo optical imaging because it is separated from the major absorption peaks of blood and water [12.73]. Based on tissue optical calculations it is estimated that near-infrared emitting QDs should improve the tumor imaging sensitivity to a detection limit of 10–100 cancer cells (see [12.72]). Semiconductor QDs of cadmium selenium telluride with fluorescence emission up to 850 nm have been developed [12.74].

In the absence of UV radiation, QDs with a stable polymer coating are essentially non-toxic to cells [12.72]. The polymer-protected QDs might be cleared from the body by slow filtration and excretion through the kidney.

Fluorescent nanoparticles could provide an early sign that apoptosis or programmed cell death is occurring as a result of anticancer therapy [12.75]. The fluorescent surface-enhanced Raman spectroscopic tagging material (F-SERS dots) are composed of silver nanoparticle-embedded silica spheres (diameter about 100 nm) with fluorescent organic dye and specific Raman labels for multiplex targeting, tracking, and imaging of cellular/molecular events in the living organism. The non-toxic F-SERS dots can monitor apoptosis through fluorescence signals as well as Raman signals in both cells and tissue with high selectivity [12.75].

Cholesterol sensor in blood based on Au nanowires in a microfluidic platform. Cholesterol and its fatty acids are important components of nerve and brain cells and are precursors of biological substances, such as bile acid and steroid hormones [12.76]. However, high cholesterol accumulation in blood serum is strongly correlated with coronary heart disease, arteriosclerosis, myocardial infarction, brain thrombosis, and hypertension (see [12.77]). Since, however, traditional cholesterol determination by non-enzymatic spectrophotometric techniques suffers from low specificity and high costs, convenient, rapid, sensitive, and cost-effective methods for the determination of cholesterol levels in blood are desirable.

Gold nanowires (175 nm in diameter; Fig. 12.29a) [12.77], based on a microfluidic platform (Fig. 12.29b), were covalently functionalized with thiol or carboxyl groups and further reacted with enzymes, such as cholesterol oxidase (COX) and cholesterol esterase (CE) for both monitoring the native and esterified cholesterol levels, which is important for the determination of the total cholesterol. The deposition of COX and CE globules from the blood on the gold nanowires is detected electrically (voltammetry) to concentrations up to 6 mM with an accuracy of $\pm 2\%$ [12.77] and a good linear response between current and cholesterol level. The increased sensitivity of the gold wire assay compared with the sensitivity of a conventional 2D detector is due to the high surface of the nanowire. Ascorbic acid (2 μM), uric acid (10 μM), and glucose (20 μM) which are usually available in blood serum do not interfere with the cholesterol detection.

Vaccines. Nanoparticles have been studied as a vaccine platform by targeting lymph node residing dendritic cells via interstitial flow and activating these cells by *in situ* complement activation. The complement is a complex system of proteins found in normal blood serum that combines with antibodies to destroy, e.g., pathogenic bacteria. After intradermal injection of the nanoparticles into mice, interstitial flow transported small nanoparticles (25 nm) highly efficiently into lymphatic capillaries and their draining lymph nodes, whereas 100 nm particles were much

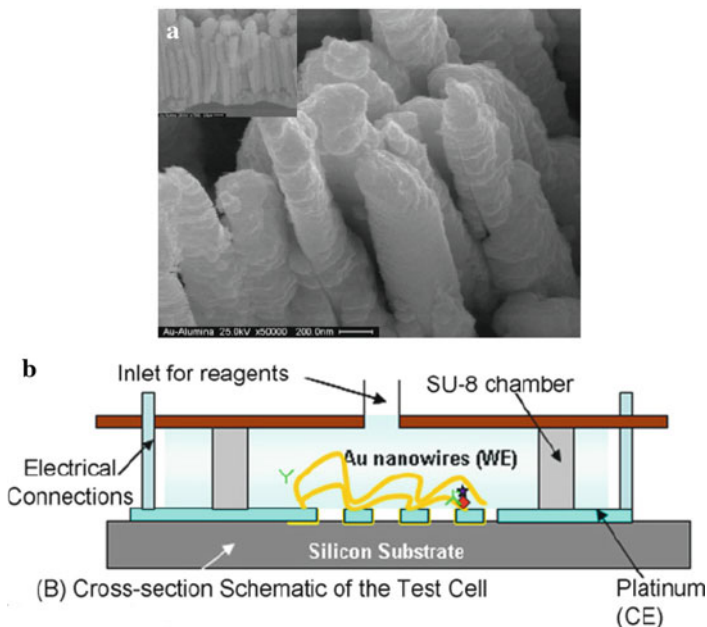


Fig. 12.29 (a) SEM images showing the top view and the cross-sectional view (*inset*) of the 175 nm Au nanowires; (b) Cross-sectional schematic of the test cell with nanowires aligned on the platinum “assembly lines” for dielectrophoresis. (Reprinted with permission from [12.77]. © 2007 Elsevier)

less efficient. The surface chemistry of these nanoparticles activated the complement cascade, generating a danger signal *in situ* and potently activating dendritic cells. Using nanoparticles conjugated to the model antigen ovalbumin in a strategy for vaccination, the generation of humoral and cellular immunity in mice was demonstrated in a size- and complement-dependent manner [12.78].

12.3 Nanoarrays and Nanofluidics for Diagnosis and Therapy

Microfluidic instrumentation can be applied to several diagnostic laboratory techniques, including blood chemistry, immunoassays, nucleic acid amplification test, biothreat detection [12.12], flow cytometry [12.79], and for biomarker-guided therapeutic targeting. Basic blood chemistry panels for analyzing enzymes, gases, electrolytes, lipids, thyroid indicators, and drugs consist of 12–20 tests and are routinely run on automated analyzers. Immunoassays allow quantification and monitoring of small molecules, large proteins, and even whole pathogens. Nucleic acid amplification tests, such as the polymerase chain reaction (PCR), can detect very small copy numbers of specific nucleic acid sequences. Test kits are commercially

available for tuberculosis, HIV, and sexually transmitted infections (STIs). Flow cytometry is the method of choice for counting cells with specific physical or chemical characteristics [12.79]. Microchips for drug delivery are microfabricated devices that incorporate micrometer-scale pumps, valves, and channels and allow controlled release of single or multiple drugs on demand [12.1, 12.80]. These devices are particularly useful for long-term treatment of conditions requiring pulsatile drug release after implantation in a patient.

12.3.1 *Lab-on-a-Chip*

The behavior of liquids changes when the volumes are reduced to below micro- or nanoliters. The corresponding micro- or nanofluidics govern the manipulation of small volumes of liquids of labs-on-a-chip which are being developed for medical, biological, and chemical application [12.81]. A lab-on-a-chip is a mini version of a chemical laboratory where chemical, biological, or medical analyses or diagnostic procedures should shrink to thumbnail size. The reason why chemical, biological, or medical procedures are scaled down to micro- and nanoliters is partly because small amounts of agents are cheaper and less toxic, but many materials are only available in small quantities as, for example, in the case of the determination of a genetic fingerprint which should be identified from a single hair or a tiny specimen of saliva. In addition, detection limits and times required for analyses are substantially reduced in the nanoliter regime.

In contrast to conventional hydrodynamics with large geometrical dimensions d , high flow velocities v , low viscosities η , and therefore high Reynolds numbers

$$Re = dv\rho/\eta,$$

where ρ is the mass density, the Reynolds numbers Re in nanofluidics are low due to small d , low v , and often enhanced η values. The transition from the macroscopic to the nanofluidic behavior is thought to occur at $Re = 1000$ [12.81]. In small tubes where the ratio of contact surface between fluid and tube wall and fluid volume is large, the interaction between fluid and tube wall (these adhesion forces may be of electrostatic nature) and the viscous forces dominates. In this situation, turbulence, appearing in macroscopic systems, is negligible, and laminar flow (Fig. 12.30a) prevails so that mixing of different fluid components is restricted to diffusive processes. The adhesion determines the wettability of a solid surface by a fluid which can be determined from the wetting angle of a drop on a surface (Fig. 12.30b). A wetting angle φ between 0° and 90° is characteristic for a wetting or hydrophilic interface, whereas $90^\circ < \varphi < 180^\circ$ characterizes a non-wetting or hydrophobic interface. Hydrophilicity can be employed for sucking a liquid into a narrow capillary which can be used for pumping a liquid.

Pumps are of particular importance for operating microfluidic chips. In addition to hydrophilicity, electrowetting (Fig. 12.30b) can be used for pumping because the

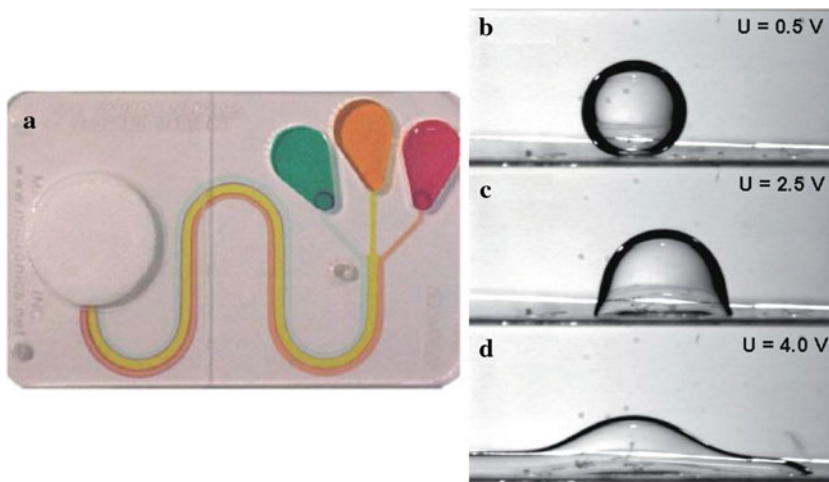


Fig. 12.30 (a) The lab-on-a-chip T-Sensor® Access™ LabCard by Micronics (credit card size) makes use of laminar flow for chemical analysis. (b–d) Water droplet in oil on an electrode substrate for deformation of the droplet by application of an electrical voltage. (Reprinted with permission from [12.81]. © 2007 Wiley-VCH)

adhesion forces between a capillary wall and a liquid are of electrostatic nature and, therefore, the wettability can be controlled by an electrical voltage. Furthermore, peristaltic pumps have been designed [12.82].

For mixing of nanofluids, the split-and-recombine technique can be used (Fig. 12.31a) where the nanofluid in a channel is separated into many smaller channels for diffusive mixing and then reunited in a larger channel. Furthermore, an alternating voltage for deformation of a droplet (Fig. 12.30b–d) or acoustic surface waves (Fig. 12.31b–c) can be applied for mixing nanofluids.

12.3.2 Microarrays and Nanoarrays

The use of miniaturized, chip-based, array detection methods, known as “*microarrays*,” has been prevalent in many health-related research areas. This biomolecular assay allows for parallel processing of a variety of targets in a small area and a reduction in processing times. Such high-throughput detection systems have been most valuable in genomics and proteomics research [12.83, 12.84]. To fabricate such an array, nanoliter volumes of protein samples are delivered to a microscope slide in spots of approximately $200\text{ }\mu\text{m}$ in diameter and yielding 1600 spots per cm^2 [12.83] (Fig. 12.32a). Additional miniaturization and fabrication of nanoarrays would generate many orders of magnitude increase in multiplexed detection in the same area as a microarray. In addition, nanoarrays should allow for much smaller sample volumes and possibly lower detection limits. By dip-pen nanolithography

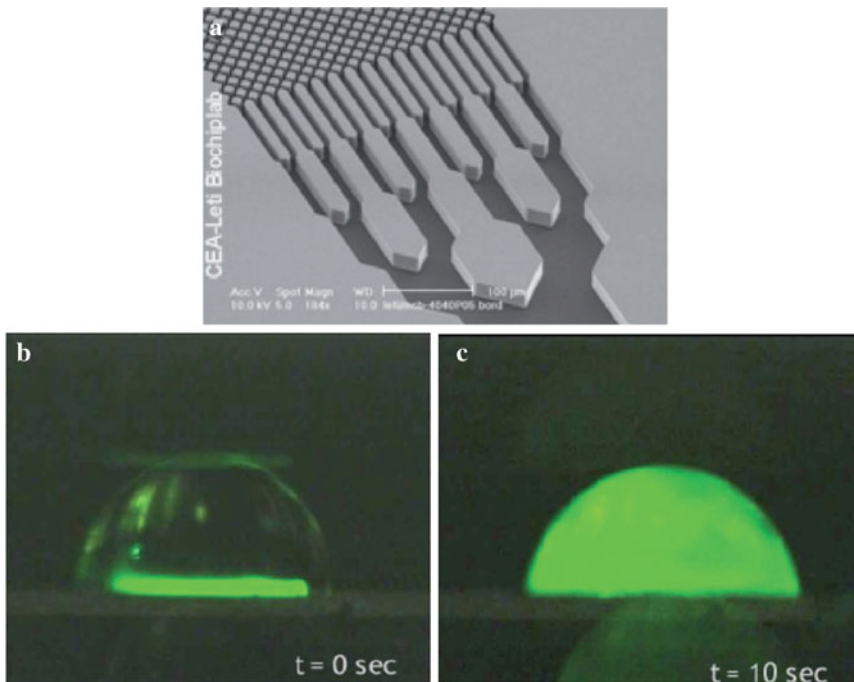


Fig. 12.31 (a) A microchannel can be sub-divided into smaller channels (split-and-recombine technique) for enhancing mixing by diffusion (scale bar, 100 μ m). (b–c) In a 50 nl droplet acoustic surface waves can be employed for mixing the fluorescence dye (b) with the water (c). (Reprinted with permission from [12.81]. © 2007 Wiley-VCH)

(DPN; see Sect. 3.10), oligonucleotides and proteins can be patterned onto surfaces with a dot size as small as 15 nm. An array fabricated by DPN would result in 100,000,000 spots in the area of a single $200 \times 200 \mu\text{m}$ spot in a conventional microarray (Fig. 12.32a). Using this technology, it is conceivable that some day the entire human genome could be screened for single-nucleotide polymorphism on a single chip [12.85] with an area of $2 \times 2 \text{ cm}^2$ and a spot size of 150 nm [12.86]. By DPN, nanoarrays were generated with monoclonal antibodies against human immunodeficiency virus-1. Coupled to nanoparticle probes, these arrays demonstrated the detection of human immunodeficiency virus from samples of human plasma with a detection sensitivity that exceeded that of conventional ELISA (see Fig. 12.24) by more than 1000-fold [12.87].

12.3.3 Microfluidics and Nanofluidics

By multilayer elastomer microfluidics, integrating many pumps, valves, and channels within an easily fabricated microchip [12.61], multiple operations can be

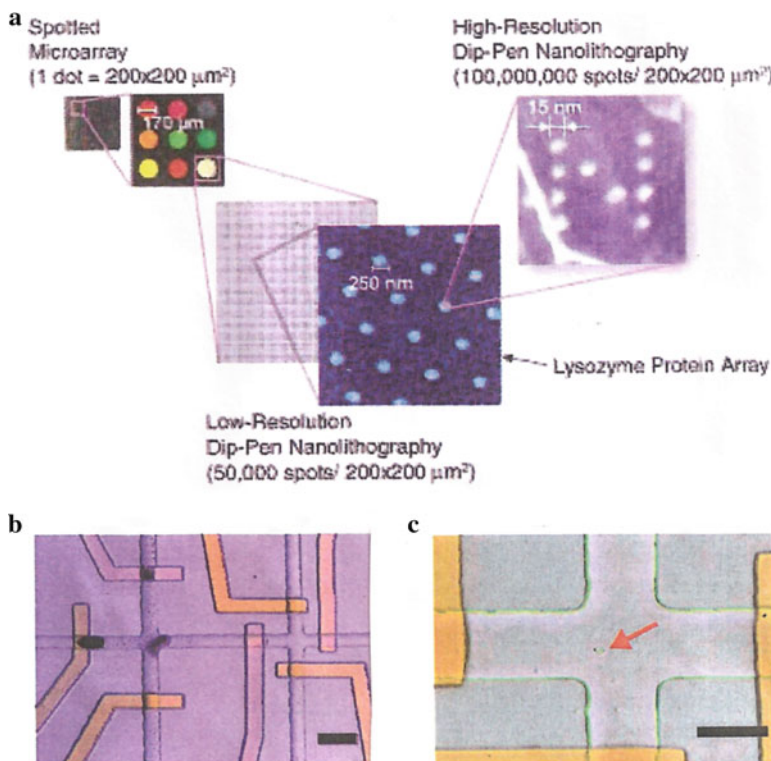


Fig. 12.32 (a) Conventional microarray versus a nanoarray fabricated by dip-pen nanolithography (DPN). In a microarray, spot sizes are typically $200 \times 200 \mu\text{m}^2$. Using low-resolution DPN, 50,000 250 nm spots can be generated in the same area. Remarkably, high-resolution dip-pen nanolithography (DPN) can generate 100,000,000 spots in the $200 \times 200 \mu\text{m}^2$ area [12.86]. (b, c) DNA purification microfluidic chip; (b) photograph of a portion of the chip showing multilayer elastomer microfluidic technology. The *orange-colored* regions are valves separating an empty chamber at the right from a region on the left, in which an affinity column for the target of interest is constructed (*dark regions*). (c) A single cell is loaded into a “cell chamber” before a lysis step. Scale bars, 100 μm [12.88]. (Reprinted with permission from [12.86] (a) and [12.88] (b) (c). © 2004 Wiley-VCH (a) and © 2004 Nature Publishing Group (b))

performed in parallel, such as cell sorting, DNA purification, and single-cell genetic profiling [12.88, 12.89]. This technology offers large-scale multiparameter analysis with several potential applications including single-cell dissection and analysis (e.g., from needle biopsies) and multiparameter disease detection from tissues and blood (Fig. 12.32b, c). Currently, integrated microfluidic systems that process only nanoliters of sample material are emerging that can be termed “*nanofluidic systems*” [12.90]. A microfluidic chip can demonstrate automated nucleic acid purification from small numbers of bacterial or mammalian cells including cell isolation, cell lysis, DNA or mRNA purification, and recovery, on a single microfluidic chip in nanoliter volumes without any pre- or postsample treatment. Measured amounts of

mRNAs were extracted from a single mammalian cell and recovered from the chip (Fig. 12.33). The achievement of extensive analysis on a single chip represents significant progress toward the realization of the “*lab-on-a-chip*,” where a complete analysis system is fully integrated, automated, and portable [12.14].

Biological serum markers for the early detection of most cancers are not available. The markers that are in clinical use, such as the prostate-specific antigen (PSA) and carcinoembryonic antigen (CEA), are non-specific and have widely different baseline expressions in the population and, therefore, are of limited effectiveness for early detection. The goal of developing reliable early detection approaches from serum or non-invasive procedures remains of paramount importance [12.91]. The applicability of microcantilevers for the quantitation of PSA at clinically significant

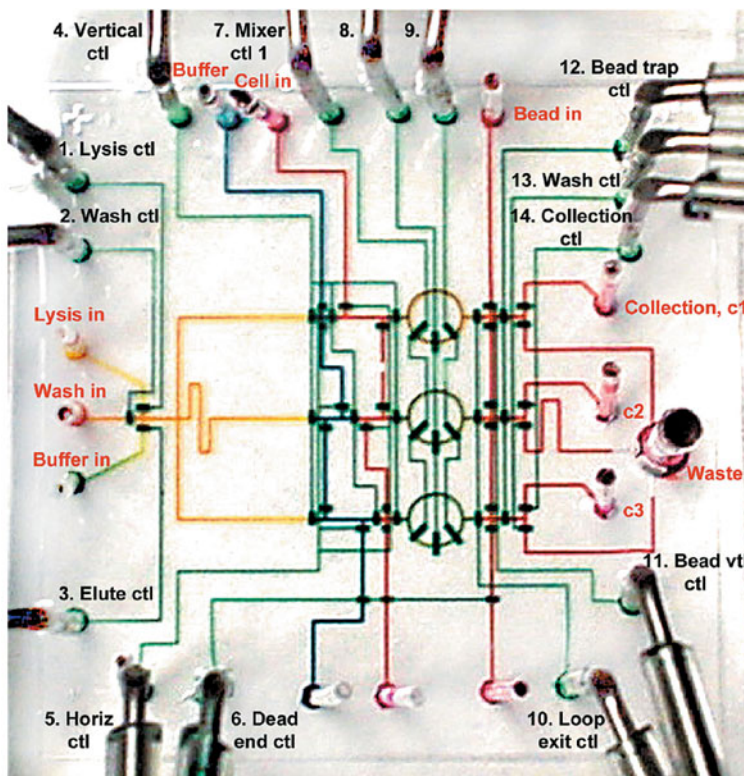


Fig. 12.33 Integrated nanoliter scale DNA processor chip with parallel architecture. The chip has two layers: the fluidic layer and the actuation layer. The actuation channels (100 μm wide) are filled with green food coloring and the fluidic channels with yellow, blue, and red food coloring, depending on their functionalities. A bacterial cell culture can enter through the “cell in” port (upper left corner) followed by various lysis and buffer solutions. Multiple parallel processes of DNA recovery from living bacterial cells are possible in three processors. The chip contains 26 access holes and 54 valves within $2 \times 2 \text{ cm}^2$. (Reprinted with permission from [12.88]. © 2004 Nature Publishing Group)

concentrations has been demonstrated [12.70] and it is realistic to envision arrays of thousands of cantilevers constructed on individual centimeter-sized chips allowing the simultaneous reading of proteomic profiles or the entire proteome for high early-detection reliability. The many similarities that these protocols share with the fabrication of microelectronic components indicate that they will be suitable for production scale-up at low cost and with high reliability (see [12.92]).

12.3.4 Integration of Nanodevices in Medical Diagnostics

In addition to the functionalization of nanowires, nanotubes, or nanocantilevers, these devices can be fabricated in arrays, enabling multiple detection assays to be performed in parallel [12.93]. Moreover, these technologies can be combined with nanoparticle probes to increase sensitivity [12.94] and can be integrated with elastomer micro- and nanofluidics to create miniaturized and automated *microfluidics/nanotechnology platforms* [12.95] (Fig. 12.34). These types of platforms may emerge within the next few years with the ability to integrate multiple operations, such as cell sorting and serum purification, as well as the ability to detect and quantify 5–10 biomarkers from single cells or from very small sample fluid volumes [12.14, 12.61].

In a *magnetic lab-on-a-drop* “laboratory device” (Fig. 12.35), a single droplet of an aqueous suspension of antibody-coated superparamagnetic particles sealed in mineral oil can be moved, merged, mixed, and split by an external magnetic field. A 25 μL blood sample containing 30 human leukemia cells expressing a green fluorescent protein (CD15-bound GFP-transfected THP-1) was placed on the chip and anti-CD15-coated superparamagnetic nanoparticles bound to the target cells, which then could be extracted within a smaller droplet for 100-fold preconcentration. This droplet was purified and added to reagents for polymerase chain reaction (PCR). The magnetic droplet is finally moved clockwise (Fig. 12.35) through four different temperature zones while a fluorescence detector indicates the presence and quantity of the desired gene sequence within a total 17 min whereas bench-scale PCR typically takes hours [12.98].

12.3.5 Implanted Chips

A nanotechnology-enhanced objective for the near-term future is to realize delivery implants for the constant-rate release of a broad spectrum of agents. The constant-rate delivery of the hormonal agent leuprolide from an osmotic pump-powered implant is already in clinical use for the treatment of prostate cancer and exemplifies the potential benefits associated with controlled-release modalities: therapeutic advantages, reduction of side effects, regularity of dosing, localization of therapeutic action, and patient compliance. However, not many drugs can be delivered by osmotic pumps and time-variable drug delivery may be desirable. To address

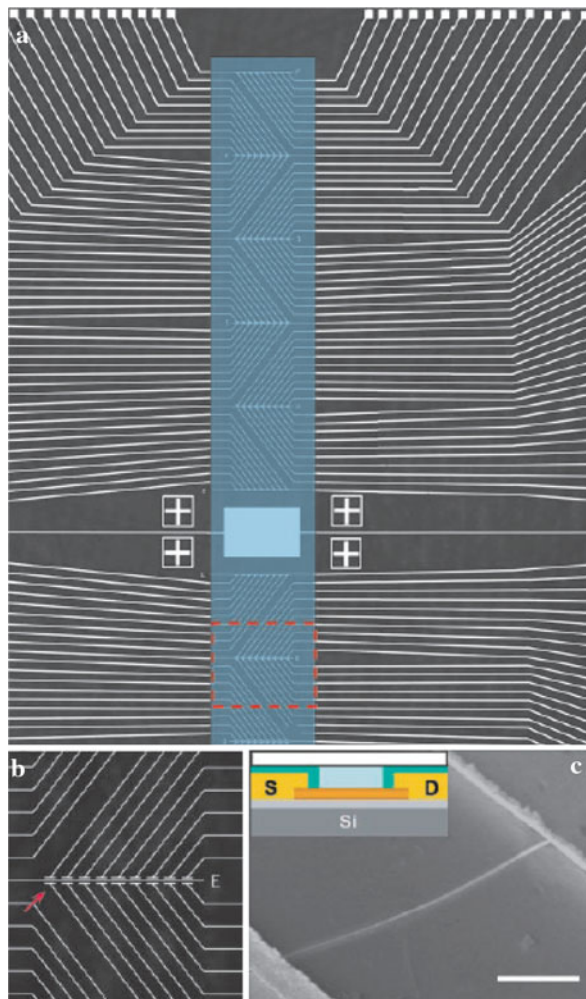


Fig. 12.34 Integrated platform: Nanowire-based biosensor incorporating nanoarray and microfluidic technology. (a) Portion of the device array with *white lines* corresponding to metal electrodes that connect to individual nanowire devices. The section colored in *blue* represents a microfluidic channel used to deliver sample material to the nanowire sensors and has a total size of $6 \text{ mm} \times 500 \text{ }\mu\text{m}$. (b) One row of nanowire devices from the *red box* in (a) with an image field of $500 \times 400 \text{ }\mu\text{m}^2$. (c) Scanning electron micrograph of a single nanowire sensor device indicated by the *red arrow* in (b). The silicon nanowire stretches between the electrode contacts visible in the *upper right* and the *lower left* regions of the image (scale bar: 500 nm). *Inset*: schematic of a single device. The nanowire (*orange line*) is connected to source (*S*) and drain (*D*) gold electrodes that are insulated by a layer of silicon (*green*). The microfluidic channel is indicated (*blue*). (Reprinted with permission from [12.96]. © 2004 National Academy of Sciences USA)



Fig. 12.35 Surface-functionalized superparamagnetic particles emulsified in mineral oil turn a free-standing droplet into a flexible virtual laboratory with (sub)-microliter volumes. By using magnetic forces, rare acute monocytic leukemia cells are extracted from blood, preconcentrated, purified, lysed, and subjected to real-time polymerase chain reaction (PCR) in minutes. The PCR works like a clock work by rotating the drop over different temperature zones. (Reprinted with permission from [12.97]. © 2008 Elsevier)

these issues, silicon membranes with nanofabricated channels of well-controlled dimension (5–100 nm) were developed [12.99] for desired release rates for any drug. Based on the nanochannel technology [12.100], controllable systems are being developed for programmable, remotely controlled, and self-regulating implants.

12.4 Targeted Drug Delivery by Nanoparticles

An early approach to drug delivery was made by Paul Ehrlich (1854–1915; Nobel prize in medicine in 1908), who proposed that if an agent could selectively target a disease-causing organism, then a toxin for that organism could be delivered along with the agent of selectivity (see [12.101]). The potential of drug delivery systems nowadays, based on the use of nano- and microparticles, stems from significant advantages such as (i) the ability to target specific locations in the body; (ii) the reduction of the quantity of drug needed to attain a particular concentration in the target; and (iii) the reduction of the concentration of the drug at non-target sites, minimizing severe side effects. This is why the number of publications dealing with nanoparticles (NPs) for drug delivery applications grew exponentially (Fig. 12.36).

Nanoparticles can act at the tissular or cellular level. They can reach beyond the cytoplasmic membrane or beyond the nuclear membrane (i.e., transfection applications). Tumor targeting with NPs may use passive or active strategies. Passive targeting occurs as a result of extravasation at the disease site where the microvasculature is leaky, leading to the selective accumulation of NPs in tumor tissue, a

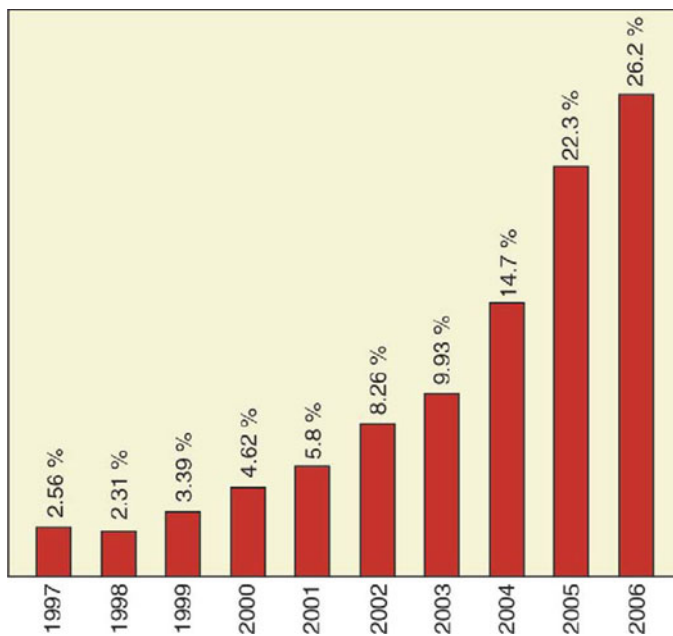


Fig. 12.36 Temporal evolution in the number of scientific papers published involving drug delivery using nanoparticles [12.101, 12.102]. (Reprinted with permission from [12.101]. © 2007 Elsevier)

phenomenon known as enhanced permeation and retention (EPR). The majority of solid tumors exhibit a vascular pore size between 380 nm and 780 nm, and NPs of this size can easily flow through the narrowest capillaries (5 μm wide). Active targeting is based on the exclusive expression of different epitopes (specific region of an antigenic molecule that binds to an antibody) or receptors in tumor cells or, alternatively, on overexpressed species such as low-molecular-weight ligands (folic acid, thiamine, sugars), peptides, proteins (transferrin, antibodies), polysaccharides, and DNA. [12.101].

New drug delivery systems with nanoparticles that can be targeted to specific cells or tissues are thought to be available by 2020 [12.103].

In the following we will discuss porous silica nanoparticles as drug carriers, gelatin nanoparticles for gene therapy, liposomes and micelles for drug delivery, and finally magnetic nanoparticles as vehicles for drugs.

12.4.1 Porous Silica Nanoparticles for Targeting Cancer Cells

Mesoporous silica nanoparticles (MSNs) show promise as novel drug delivery systems. They have been used as agents for administering the anticancer drug camptothecin (CPT) [12.104] or the protein cytochrome *c* [12.105] directly into

human cancer cells. Camptothecin induces cell death by poisoning DNA topoiso-merase I, an enzyme capable of removing DNA supercoils [12.106]. Cytochrome *c* is a membrane-impermeable protein involved in apoptosis or controlled cell death, a mechanism that can fail in cancer cells. Fluorescent MSNs with a diameter of 130 nm and with a MCM-41-like structure (see Sect. 3.9) of 2 nm diameter channel pores (Fig. 12.37) were filled with CPT (a molecule 1.3 nm × 0.6 nm in size), one of the most promising cancer drugs of the 21st century (see [12.104]). Clinical application of CPT in humans has, however, not been achieved to date because of the poor water solubility of this drug. The MSNs can be used to overcome this insolubility problem.

A suspension of the CPT-loaded MSN was added to the human cancer cell lines PANC-1, AsPC-1, Capan-1 (pancreatic), MKN45 (gastric), and SW480 (colon) to determine if the nanoparticles were able to transport the hydrophobic CPT into the cancer cells. As shown in Fig. 12.37c, the cells that were treated with CPT-loaded MSNs showed strong blue fluorescence typical for CPT, while those that were treated in a control experiment with a suspension of CPT in phosphate-buffered

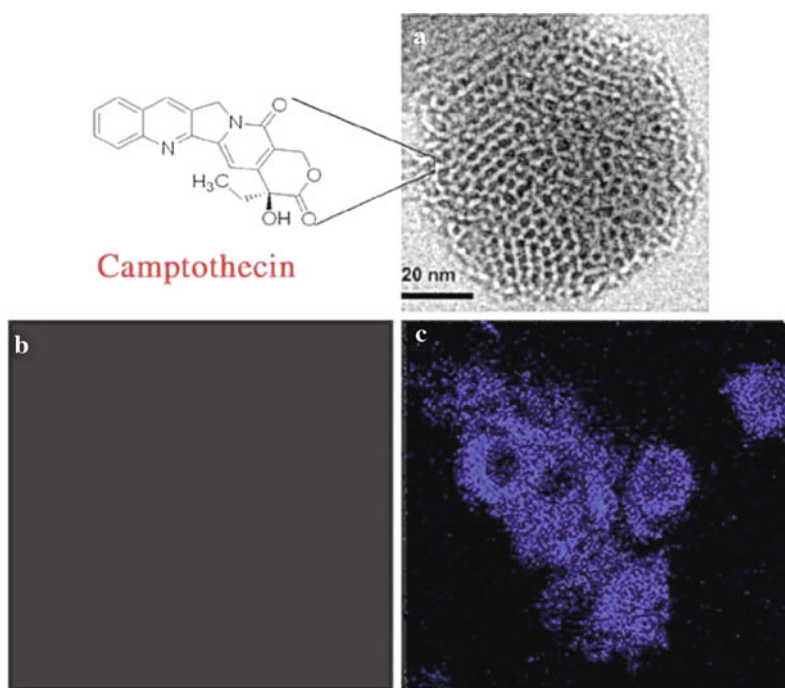


Fig. 12.37 (a) Transmission electron micrograph of a mesoporous silica nanoparticle (MSN). Blue fluorescence of camptothecin (c) after uptake of the camptothecin (CPT) loaded MSNs into the PANC-1 human pancreatic cancer cells after incubation for 3 h. No fluorescence was observed (b) within the cells that were incubated with a suspension of CPT in phosphate-buffered saline (PBS) solution. (Reprinted with permission from [12.104]. © 2007 Wiley-VCH)

saline (PBS) solution remained non-fluorescent (Fig. 12.37b). This observation indicates that the MSNs were able to transport and deliver CPT inside the cancer cell. CPT remained inside the nanoparticles during cell penetration and was then released in the hydrophobic regions of the cell compartments.

The cytotoxic effect of CPT-loaded MSNs leading to growth inhibition and cell death was demonstrated on pancreatic cell lines (PANC-1, ASPC-1, Capan-1), a colon cancer cell line (SW480), and a stomach cancer cell line (MKN45). By contrast, CPT suspended in phosphate-buffered saline (PBS) did not show any cytotoxicity to cancer cells [12.104]. These results show that mesoporous silica nanoparticles loaded with CPT can circumvent the problem of insolubility of cancer drugs in aqueous solutions in order to make use of their full efficiency.

Mesoporous silica nanoparticles can, furthermore, not only serve as vehicles for introducing membrane-impermeable proteins, such as the apoptosis-involved cytochrome *c*, into the cells, but they are also able to escape the endolysosomal entrapment so that the protein can be efficiently released into the cytoplasm [12.105]. In order to demonstrate this, cytochrome *c* was tagged with the green fluorescent dye fluorescein isothiocyanate (FITC), loaded into MSN, and efficiently introduced into the HeLa human cervical cancer cell cultures. In order to determine whether or not the cytochrome *c*-loaded MSNs could escape the endosomal entrapment, the endosomes were stained with the red fluorescent endosome marker FM4-64 (see [12.105]). In Fig. 12.38b, exclusively separate green and red dots are seen. This means that the MSNs loaded with cytochrome *c* can quantitatively escape the endosomes to efficiently deliver the drug in the cytoplasm. If the MSNs (green)

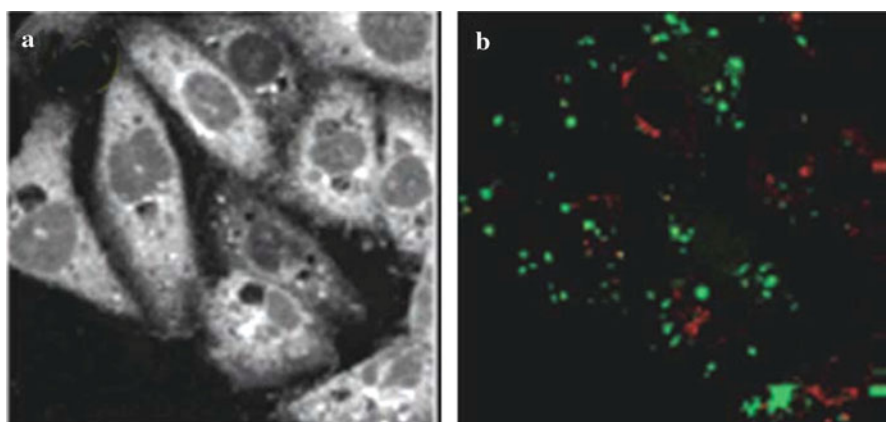


Fig. 12.38 Uptake of the mesoporous silica nanoparticles (MSNs), loaded with the dye fluorescein isothiocyanate (FITC) and the apoptosis-inducing protein cytochrome *c*, by HeLa human cervical cancer cells as observed by confocal fluorescence microscopy after incubation for 24 h. (a) Auto-fluorescence image of the cells. (b) Fluorescence images of the cytochrome *c* protein (green) and of the cellular endosomes (red). The separation of the green and red dots demonstrates that the protein is not entrapped in the endosomes but is delivered to the cytoplasm. (Reprinted with permission from [12.105]. © 2007 American Chemical Society)

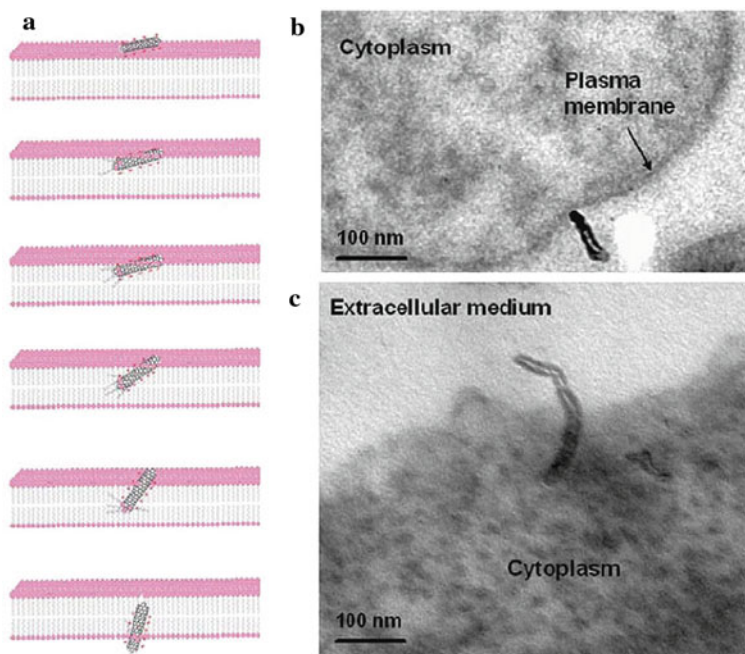


Fig. 12.39 Carbon nanotubes acting as nanoneedles. (a) Schematic of a CNT crossing the plasma membrane; (b) Transmission electron micrograph (TEM) of multiwalled carbon nanotubes functionalized with NH_3^+ (MWNT- NH_3^+) interacting with the plasma membrane of A549 cells; and (c) TEM of MWNT- NH_3^+ crossing the plasma membrane of HeLa cells. (Reprinted with permission from [12.107]. © 2007 Elsevier)

would be entrapped in the endosomes (red), this would result in yellow dots as a result of green-red superposition which is not observed [12.105].

Biocompatible functionalized carbon nanotubes can be internalized by a wide range of cell types (Fig. 12.39) and their high surface area can potentially act as a template for cargo molecules such as peptides, proteins, nucleic acids, and drugs. The application of carbon nanotubes includes vaccine delivery, gene delivery, cancer therapy, and HIV/AIDS therapy [12.107].

12.4.2 Gene Therapy and Drug Delivery for Cancer Treatment

If cancer can be detected early enough, statistics have shown that the burden of the disease is drastically reduced. The use of nanofunctional materials can significantly transform the way the disease is diagnosed, imaged, and treated [12.108, 12.109, 12.110]. Early detection of cancer can be achieved by using nanoparticles for magnetic resonance imaging (MRI) [12.111]. Normal, cancerous, and metastatic cells can be detected and differentiated by making use of nanoparticle sensor arrays [12.112].

Personalized cancer therapy will in the future require genetic testing to select the best treatment. The sequencing of the whole genome of a tumor (see [12.113]) that had spread from a patient's mouth to his lung demonstrated mutations in a tumor-suppressor gene called *PTEN*, and an abnormally high expression of a gene downstream of *PTEN*, called *RET* [12.114]. This explained why the patient had not responded to the drug erlotinib, to which patients with active *PTEN* respond better. Instead, the patient has been put on a drug called sunitinib, which inhibits the protein made by *RET*, and the patient's cancer subsequently regressed (see [12.114]). The sequencing of a tumor genome cost US \$1 million in 2008 but could drop to \$50,000 per tumor in 2010 (see [12.114]).

Breast tumor xenografts treated by gene therapy [12.115]. Gene therapy strategies for solid tumors can be divided into methods that restore cellular growth control, confer drug sensitivity, induce antitumor immunity, or inhibit angiogenesis. The major difficulty in systemic gene therapy, however, is the need for safe and effective vector systems that can deliver the gene to the target tissue and cells and allow for the expression of the protein of interest. For anti-angiogenic gene therapy, the vascular endothelial growth factor (VEGF) is one of the most important regulators of tumor neovascularization and is overexpressed by most types of cancers (see [12.115]). The pro-angiogenic effects of VEGF can be suppressed by binding to the high-affinity tyrosine kinase receptors present on the endothelial cells. The soluble form sFlt-1 of the VEGF receptor can be used as a potent agent for anti-angiogenic gene therapy. The plasmid ps Flt-1/pc DNA3 contains the gene sequence encoding for the extracellular domain sFlt-1 of the VEGF receptor. When expressed in cells, the sFlt-1 plasmid results in the formation of soluble FMs-like tyrosine kinase receptor 1, a variant of the VEGF receptor. The expressed sFlt-1 has shown angiostatic activity by sequestering VEGF produced by tumor cells.

Successful use of adenoviral vectors (DNA-carrying viruses that cause conjunctivitis and upper respiratory tract infections in humans) for sFlt-1-expressing plasma DNA delivery to tumor-bearing animals has been reported [12.116]. However, although viral vectors are efficient they have been plagued with serious toxicity concerns [12.117]. In contrast, it has been demonstrated that non-viral nanoparticles, such as gelatin nanoparticles, can safely and successfully transfect tumor mass *in vivo*.

Poly(ethylene glycol) (PEG)-modified thiolated gelatin nanoparticles (PEG-SHGel) were found to have the longest circulation time ($t_{1/2} > 15$ h) in plasma upon intravenous administration. The systemic delivery and the transfection potential of sFlt-1 expressing plasmid DNA in PEG-SHGel nanoparticles with a diameter of 320 nm has been examined *in vitro* in MDA-MB435 human breast adenocarcinoma cells and *in vivo* in human breast tumor bearing mice [12.115]. Anti-angiogenic efficacy studies (Fig. 12.40) indicate the capability of PEG-SHGel nanoparticles as vehicles for therapeutic gene delivery to human breast adenocarcinoma implanted in mice. In animals treated with PEG-SHGel nanoparticles loaded with DNA, the tumor volumes after 25 days were similar to those in the beginning of the studies, whereas the tumor volumes in untreated mice grew substantially. From the images of the excised tumors shown in Fig. 12.40, it is clear that the expressed sFlt-1 is

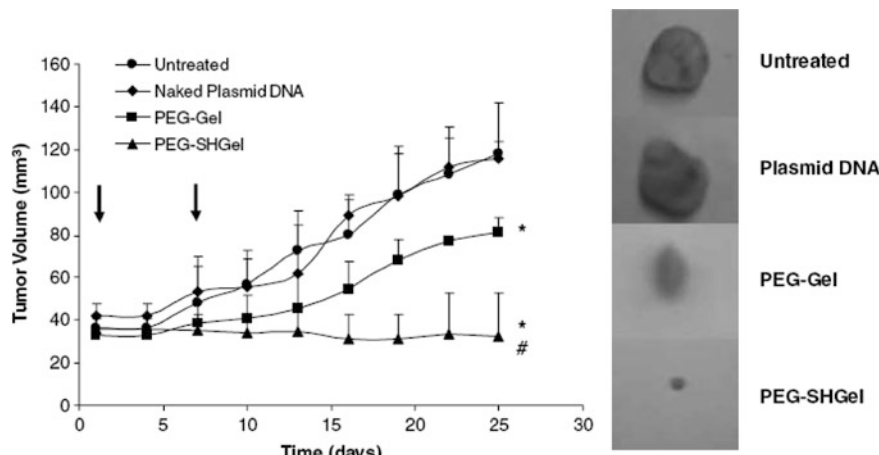


Fig. 12.40 In vivo antitumor efficacy study of expressed sFlt-1 in MDA-MB-435 human breast adenocarcinoma-bearing mice by tumor volume measurements. PEG-SHgel and PEG-Gel nanoparticles with sFlt-1 encoding plasmid DNA were administered intravenously to the mice. Untreated animals and those receiving naked plasmid DNA served as controls. After killing the mice 40 days posttherapy, the tumor masses from control and test animals were surgically excised showing the smallest tumor volume after PEG-SHgel treatment. (Reprinted with permission from [12.115]. © 2007 Nature Publishing Group)

effective in suppressing tumor growth in the MDA-MB-435 xenograft model. The nanoparticles with a diameter of 320 nm could be accumulated in the tumor mass by the enhanced permeability and retention (EPR) effect because the diameter is still smaller than the 400–600 nm vascular pore size [12.118], with additional accumulation only in the liver [12.115]. It, furthermore, should be emphasized that in the gelatin nanoparticles the plasmid DNA structure is maintained in the supercoiled state for efficient nuclear import. As the nuclear membrane pore diameter is <20 nm, supercoiled plasmid can penetrate the nucleus more effectively than a linear or open circular plasmid [12.115].

Oligonucleotide-modified gold nanoparticle complexes have been used as probes to control gene expression in cells [12.119].

Prostatic hyperplasia and prostate cancer has been studied in mice [12.120]. More than half of men in the United States over the age of 60 suffer from the effects of an enlarged prostate (benign prostatic hyperplasia – BPH). In addition, prostate cancer is the most common cancer diagnosed in the United States. Current prostate therapies are often accompanied by serious side effects that impact on the quality of life. Often these side effects result from the damage to healthy tissues in close proximity to the prostate. Thus, there is a need for an improved therapy that is more effective and safer than existing treatments.

In a gene therapy study [12.120], biodegradable C32 nanoparticles (poly(butane diol diacrylate co amino pentanol)) were used for delivering DNA which encodes a suicide gene that expresses the diphtheria toxin A chain (DT-A), a potent toxin that

arrests protein synthesis, resulting in cell death by apoptosis. In addition to delivering DNA to a specific site, a prostate-specific human PSA (prostate-specific antigen) promoter was used to regulate the gene DT-A expression. Extensive apoptosis was observed in prostate epithelial cells and prostate tumors, but not in the surrounding tissues, following local injection of C32 nanoparticles delivering PSA/DT-A DNA. This strategy may have applications in the treatment of BPH and prostate cancer.

Gross morphological abnormalities were observed in the ventral/lateral lobes of mice injected with C32-PSA/DT-A nanoparticles (Fig. 12.41a), while there was no evidence of an increased number of apoptotic smooth muscle cells and other stromal cells in the inter-acini (between the saclike dilatations of a compound gland) spaces. In contrast, only a few apoptotic cells were observed in prostates injected with phosphate buffer saline (PBS; Fig. 12.41b). Cell death in surrounding tissues and organs following intraprostatic injection of C32-PSA/DT-A nanoparticles did not appear to increase above the low normal levels. In mice injected with C32-PSA/DT-A nanoparticles no abnormalities were observed in the level

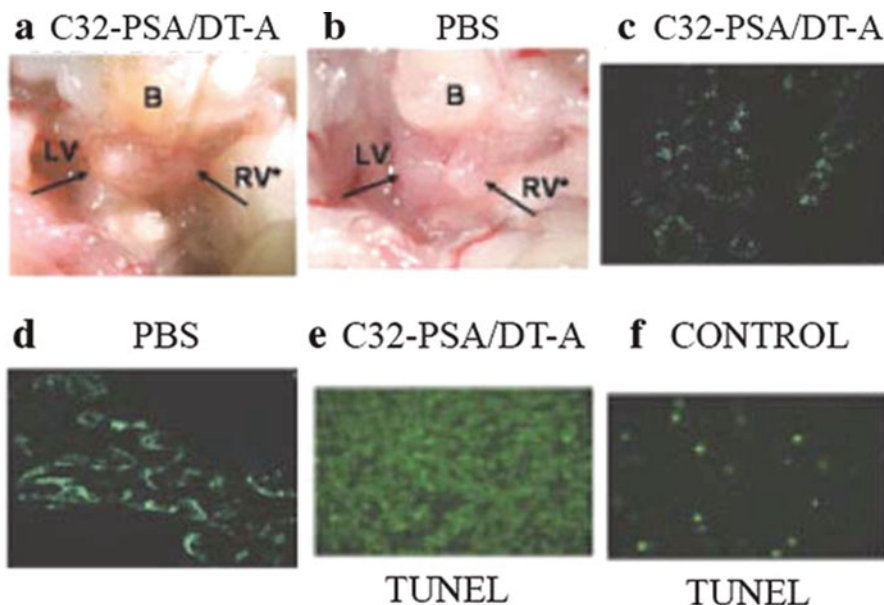


Fig. 12.41 (a, b) Morphological evidence for cell death following intraprostatic injection of (a) C32-PSA/DT-A nanoparticles (see text) and (b) phosphate-buffered saline (PBS) in mice. (c, d) Targeted death of luminal cells in the prostate following intraprostatic injection of C32-PSA/DT-A nanoparticles in mice. Basal cells (blue CFP fluorescence dye) have disappeared in the prostate epithelium after C32-PSA/DT-A injection (c) while they are visible after control PBS administration (d). (e, f) TUNEL (terminal deoxynucleotidyltransferase biotin–deoxyuridine triphosphate nick-end labeling) staining of sections of prostate tumors of mice following intratumoral injection of C32-PSA/DT-A nanoparticles. Upon TUNEL staining, apoptotic cells in the C32-PSA/DT-A treated tumor appear green (e) whereas after a control injection (f) no green apoptotic cells are visible. (Reprinted with permission from [12.120]. © 2007 Wiley Interscience)

of serum markers, liver function, or muscle damage. Likewise, no histological abnormalities were detected upon analysis of sections of organs, including bladder, testis, epididymis (tubular spermatic duct from a testicle), small intestine, large intestine, liver, spleen, pancreas, kidney, adrenal glands, lungs, thyroid, heart, skeletal muscle, skin, bone with marrow, and brain.

Experiments performed in order to explore the specificity, with which nanoparticle-delivered PSA/DT-A DNA kills basal or luminal prostate cells, demonstrate a reduction in green fluorescent protein (GFP) expression in PSA/DT-A injected prostate lobes of mice (Fig. 12.41c, d), reflecting the shutdown of protein synthesis in PSA-expressing luminal cells, resulting in their death.

The intratumor injection of C32-PSA/DT-A nanoparticles into transgenic mouse models that develop prostate tumors revealed that ~80% of the tumor cells at the site of injection had undergone apoptosis, as compared to < 5% of tumor cells in uninjected tumors (Fig. 12.41e, f). These results show that local injection of nanoparticle-delivered DT-A kills both normal prostate cells and prostate tumor cells. Locally administered nanoparticles with a transcriptionally regulated suicide gene payload may thus offer a distinct advantage over existing therapies for BPH and cancer that lack specificity and often damage neighboring tissue and cause unwanted side effects.

Nanoparticles (NPs) of poly(D, L-lactic-co-glycolic acid) (PLGA) – poly(ethylene glycol) (PEG) were conjugated with the prostate-specific membrane antigen (PSMA) targeting A10 2'-fluoropyrimidine RNA aptamers (Apt) and used as a vehicle to transport the platinum (IV) compound c, t, c-[Pt(NH₃)₂(O₂CCH₂CH₂CH₂CH₂CH₃)₂Cl₂] (Fig. 12.42) to the prostate cancer cells. Within the cell, a lethal dose of the cancer drug cisplatin is released upon reduction of the platinum (IV) precursor. The effectiveness of PSMA targeted Pt-NP-Apt nanoparticles against the PSMA⁺ LnCaP prostate cancer cells is approximately an order of magnitude greater than that of free cisplatin, because prostate cancer is resistant to chemotherapy with free cisplatin due to poor targeting [12.121].

Multifunctional nanoparticles with CdSe quantum dot (QD) cores and polymeric coatings were used for efficient short-interfering RNA (siRNA) delivery [12.122]. RNA interference is a powerful technology for sequence-specific suppression of

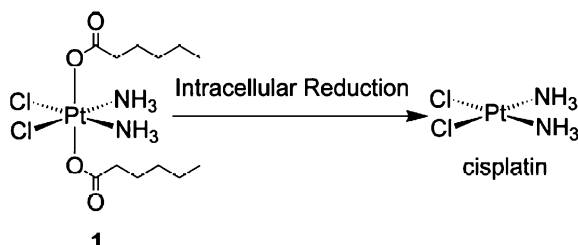


Fig. 12.42 Chemical structure of the hydrophobic platinum (IV) compound **1** and the chemistry by which the active drug, cisplatin, is released, after reduction in the cell. (Reprinted with permission from [12.121]. © 2008 National Academy of Sciences USA)

genes and has broad applications ranging from functional gene analysis to targeted therapy [12.122]. These QD–siRNA nanoparticles are simultaneously optical and electron microscopy probes and can be used for real-time tracking and localization of QDs during delivery and transfection. The results demonstrate improvement in gene silencing efficiency by 10–20-fold and simultaneous reduction in cellular toxicity by fivefold to sixfold, when compared directly with existing transfection agents for MDA-MB-231 cells [12.122]. For the delivery of siRNA (TERT) into tumor cells for silencing the TERT gene, which is critical for the development and growth of tumors, also carbon nanotubes have been used [12.123].

12.4.3 Liposomes and Micelles as Nanocarriers for Diagnosis and Drug Delivery

Pharmaceutical nanocarriers with an enhanced drug reservoir, such as liposomes (artificial nanoscopic vesicles, 70–200 nm in size, consisting of an aqueous core enclosed in phospholipid layers) or micelles (nanoscopic aggregation of molecules) can be equipped with a broad variety of useful properties, such as longevity in blood allowing for their accumulation in pathological areas; specific targeting to disease sites due to targeting ligands attached to the nanocarrier surface; enhanced intracellular penetration due to appropriate surface-attached cell-penetrating molecules; contrast properties due to carrier loading with contrast materials for *in vivo* visualization; stimuli sensitivity allowing for drug release from carriers under particular physiological conditions [12.19].

In vivo longevity is most frequently imparted to drug carriers, such as liposomes, by coating them with a protective layer of poly(ethylene glycol) or PEG, typically with a molecular weight from 1–20 kDa. The thus protected nanocarriers show a sharp increase in blood circulation time and a decrease in liver accumulation. The anticancer agent doxorubicin incorporated in PEG-liposomes has already demonstrated very good clinical results [12.124]. From a pharmacokinetic point of view, the association of drugs with nanocarriers has the pronounced effects of delayed drug absorption, spatially restricted drug biodistribution, decreased volume of drugs, etc.

Targeting vectors (antibodies, peptides, sugars, folates) can be attached to the nanocarriers for specific recognition of the surface characteristics of the target cells. Nanoparticles made of gelatin and human serum albumin were modified with the HER2 receptor-specific antibody trastuzumab (Herceptin[®]) via an avidin–biotin linkage [12.125]. These surface modified nanoparticles were efficiently endocytosed by HER2-overexpressing SK-BR-3 breast cancer cells (Fig. 12.43a). PEG-liposomes were targeted by peptides specific for integrins of tumor vasculature and, being loaded with the anti-cancer agent doxorubicin, demonstrated increased efficiency against C26 colon carcinoma in murine models [12.126].

Stimuli-sensitivity functions can be added to PEGylated pharmaceutical nanocarriers which allows for the detachment of the protecting polymer (PEG) chains under

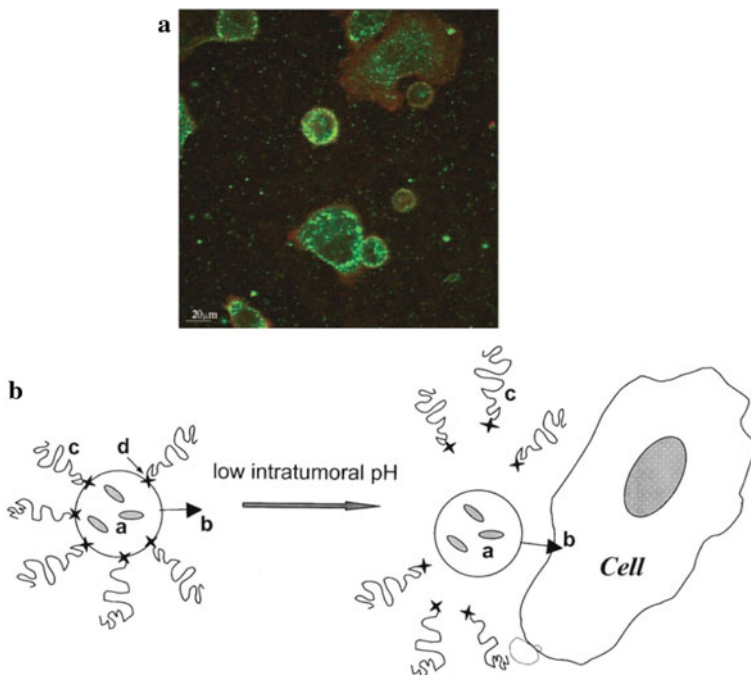


Fig. 12.43 (a) Cellular uptake and intracellular distribution of gelatin nanoparticles (green) modified with antibodies in SK-BR-3 breast cancer cells [12.125]. (b) Schematic representation of a “double-targeted” pharmaceutical nanocarrier (a – loaded drug; b – temporarily “hidden” function, e.g., cell-penetrating peptide; c – “shielding” polymeric coat providing longevity in the blood and preventing the hidden function from premature interaction with target cells; polymeric chains are attached to the carrier surface via d, which represent low pH degradable bonds) and its interaction with a tumor cell after the pH-dependent de-shielding of the hidden cell-penetrating function when already inside the tumor. (Reprinted with permission from [12.19]. © 2006 Elsevier)

the action of local stimuli in pathological areas, such as decreased pH value or increased temperature characteristic for inflamed or neoplastic areas. This detachment may be favorable for drug delivery. Labile linkage of PEG to a liposome can be based on diortho esters, double esters, vinyl esters (see [12.19]) that are quite stable at pH around 7.5 but are hydrolyzed rapidly at pH values of 6 and below, such as in tumors, infarcts, cell cytoplasm, or endosomes. By such a stimuli-sensitive technique a nanoparticulate drug delivery system can be prepared capable to accumulate in the required organ or tissue, and then penetrate inside target cells delivering there its drug or DNA load (see Fig. 12.43b).

Functionalization for intracellular delivery may facilitate the therapeutic action of nanocarriers inside the cell unto the nucleus or other specific organelles, such as mitochondria. The delivery of DNA into somatic cells is the important step in gene therapy to supplement defective genes or provide additional biological functions (see [12.127]). Compared with viral vectors for gene therapy, synthetic cationic

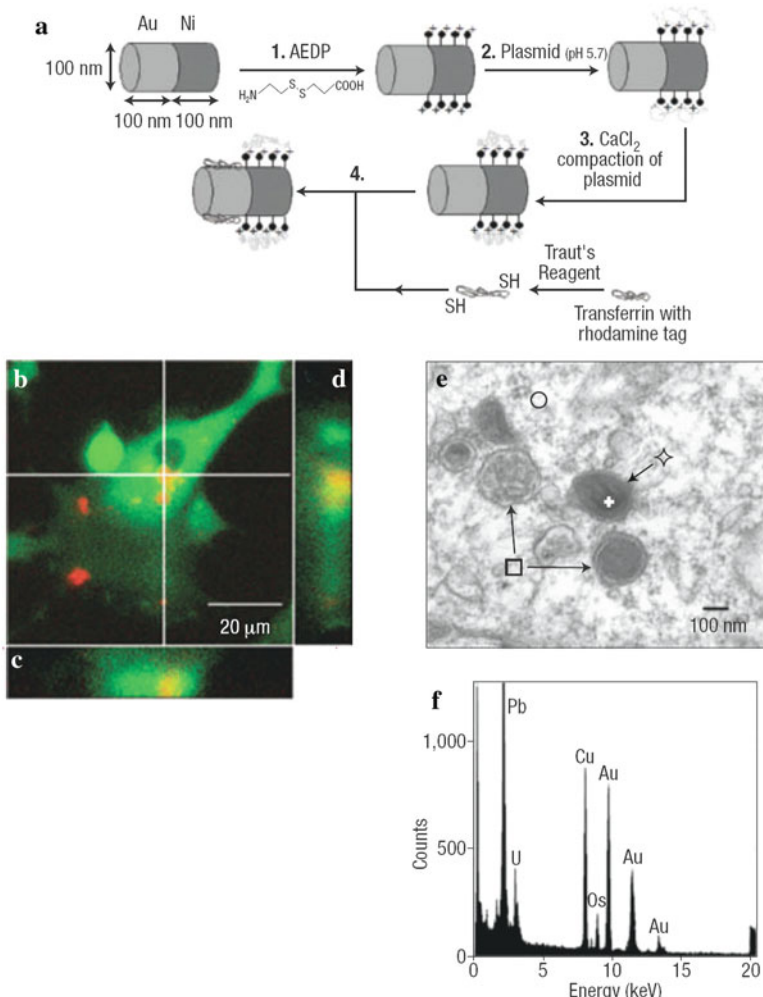


Fig. 12.44 Efficient DNA transfection by means of transferrin-conjugated Au/Ni nanorods. **(a)** Schematic representation of the spatially selective binding of DNA plasmids and transferrin to bimetallic nanorods. Illustration of the nanorod functionalization. *1.* Nanorods are incubated in the AEDP linker. The carboxylate end groups bind to the Ni segment. The cleavable disulfide linkage promotes DNA release within the reducing environment of the cell. *2.* Plasmids are bound by electrostatic interactions to the protonated amines on the Ni surface. *3.* CaCl_2 compacts the plasmids. *4.* Rhodamine-conjugated transferrin is selectively bound to the gold segment of the nanorod. **(b)** Laser scanning confocal microscopy images of transfected cells. Live HEK 293 cell with the *red* rhodamine (633 nm) fluorescence identifying the subcellular location of the nanorods while the *green* fluorescent GFP expression (543 nm) confirms the transfection. **(c, d)** Orthogonal sections confirm that the nanorods are within the cell. **(e)** TEM image showing the presence of the nanorods in one of the vesicles (\diamond); \circ denotes the cytoplasm of the cell and \square the empty vesicle. **(f)** TEM-EDX spot analysis (white cross on Fig. 12.44e) confirming that the nanorod is in the vesicle. The U, Pb, Cu, and Os are from grid and TEM sample preparation. (Reprinted with permission from reference. (Reprinted with permission from [12.127]. © 2003 Nature Publishing Group)

non-viral gene delivery systems reduce, e.g., the risk of cytotoxicity. In a recent approach for a non-viral gene delivery system in vitro and in vivo [12.127], bimetallic Au/Ni nanorods are used that can selectively bind DNA plasmid on the Ni section and a cell targeting protein, transferrin, on the Au section (Fig. 12.44a). Transferrin functionalization is favorably used because all metabolic cells take in iron through receptor-mediated endocytosis of the transferrin–iron complex. By means of a rhodamine tag on the transferrin, the intracellular distribution of the transfected DNA-conjugated nanorods can be observed.

In vitro transfection experiments on the human embryonic kidney (HEK 293) cell line show the green fluorescent protein (GFP) emission of the cells as a result of transfection (Fig. 12.44b). Superimposed is the red emission from the rhodamine conjugated together with the transferrin to the Au segments of the nanorods. Electron dispersive x-ray (EDX) analysis on the image of Fig. 12.44c shows the engulfment of the nanorods in a vesicle (Fig. 12.44c, d). This suggests that the transfection is due to DNA plasmids released or cleaved from the nanorods prior to nuclear entry. Nanorod-mediated DNA transfection making use of transferrin conjugation is substantially increased in comparison with naked DNA.

Increased anticancer activity of micelles loaded with the anticancer agent paclitaxel was achieved by coating the micelles with PEG-PE (PE-phospholipid) and Lipofectin® lipids (LL) [12.128] where Lipofectin® is a mixture of cationic lipids. The addition of LL facilitating the intracellular uptake and cytoplasmic release of paclitaxel-containing PEG-PE/LL micelle nanocarriers resulted in a substantially increased death of A2780 cancer cells (IC₅₀ value = 1.2 μ M paclitaxel) compared to that under action of LL-free PEG-PE micelles with paclitaxel (IC₅₀ = 5.8 μ M) or free paclitaxel [12.128].

12.4.4 Drug Delivery by Magnetic Nanoparticles

A drug can be bound to a magnetic nanoparticle, introduced in the body, and then concentrated in the target area by means of a magnetic field (using an internally implanted permanent magnet or an externally applied field). The main advantages of magnetic nanoparticles are that they can be (i) visualized (superparamagnetic NPs are used in MRI; see Sect. 12.2); (ii) guided by means of a magnetic field; and (iii) heated in a magnetic field to trigger drug release or to produce hyperthermia (see Sect. 12.6) of the tissue.

Superparamagnetic behavior of nanoparticles, which occurs for Fe-based NPs at sizes <25 nm, is needed in medical applications to avoid magnetic agglomeration and the possible embolization of capillary vessels (which could occur with ferromagnetic particles) once the magnetic field is removed. In superparamagnetic NPs without external magnetic field, the magnetization of each crystallite fluctuates, so that the magnetic moment of individual crystallites compensate for each other and the overall magnetic moment disappears. When an external field is

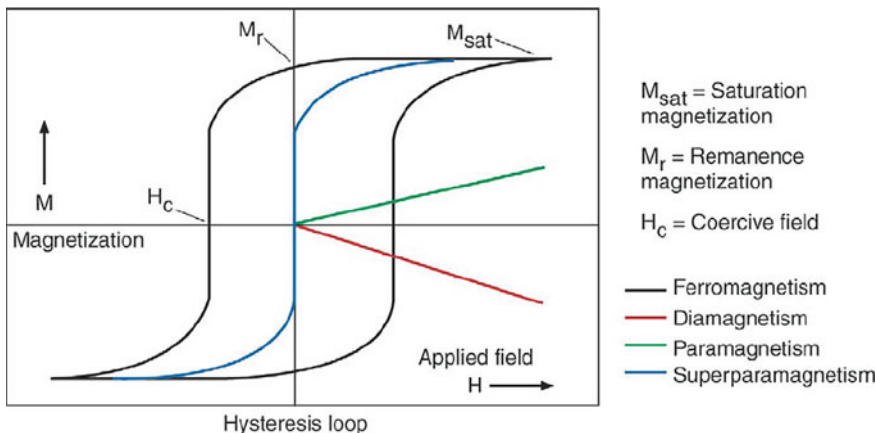


Fig. 12.45 Magnetization versus applied magnetic field (hysteresis loop) characteristic for ferromagnetic and superparamagnetic NPs. For comparison, para- and diamagnetic behaviors are also shown, as well as the values of remanence, M_r , and of coercive field, H_c . (Reprinted with permission from [12.101]. © 2007 Elsevier)

applied, the magnetic moment of entire crystallites aligns with the magnetic field (Fig. 12.45).

A wide variety of molecules has been loaded on nanoparticles, including cell-penetrating peptides for MRI applications [12.129], genes for transfection [12.130], anti-cancer agents [12.131], [12.132], and non-steroidal anti-inflammatory drugs [12.133]. Chemicell GmbH currently commercializes the anti-cancer agent Target MAG doxorubicin nanoparticles (50 nm) involving a multidomain magnetic core and a cross-linked starch matrix with terminal cations that can be reversibly exchanged by the positively charged doxorubicin [12.134]. These NPs loaded with mitoxantrone have already been used in animal models with successful results [12.135]. Other magnetic drug delivery systems, that have already been commercialized, are MagNaGel® [12.136] and FluidMag® (see [12.101]).

The main limitation of magnetic drug delivery relates to the availability of strong external magnetic fields for generating the magnetic field gradient to control the residence time of NPs in the desired area. Obviously the geometry of the magnetic field is extremely important for designing a magnetic targeting process. With respect to the high magnetic fields it may be mentioned here that human exposure to static magnetic fields up to 8 T has not shown any clinically relevant adverse physiological or neurocognitive effects [12.137], and human imaging at fields in excess of 10 T is now being planned (see [12.101]).

As a means to elude the limitations of an external magnetic field, internal magnets, e.g., permanent Nd–Fe–B magnets, can be located in the vicinity of the target by using minimally invasive surgery [12.138] together with simulation studies [12.139].

12.4.5 Nanoshells for Thermal Drug Delivery

Nanoshells for thermal drug delivery can be used in combination with an extra-corporal low-power diode laser. Here, infrared absorbing gold nanoparticles can be integrated into a drug-entrapping polymeric hydrogel and, after interstitial implantation, drug release is initiated by a temperature increase (above the solution temperature of the polymer), induced with laser light at 800–1200 nm wavelengths, which is transmitted through tissue with little attenuation and no local damage [12.140].

12.4.6 Photodynamic Therapy

Photodynamic therapy, which is based on the use of photo-sensitive drugs, is another technique for tumor treatment [12.141]. Molecules called photosensitizers (e.g., 9,10-bis[4'-(4''-aminostyryl) styryl]anthracene – BDSA) are activated with light for fluorescence resonance energy transfer (FRET) to the energy acceptor (2-devinyl-2 (1-hexyloxyethyl) pyropheophorbide – HPPH) to promote the local formation of highly reactive species – such as singlet oxygen – to attack diseased tissue. Aggregates of fluorescent dye molecules BDSA and HPPH were shown to produce singlet oxygen in water dispersions upon 850 nm illumination as monitored by the oxidation of the disodium salt of 9,10-anthracenedipropionic acid (ADPA) [12.141]. In vitro studies show that the nanoparticles are taken up by HeLa (human cervix epitheloid carcinoma) cells (Fig. 12.46a) and give rise to cell necrosis due to singlet oxygen production by 850 nm illumination (Fig. 12.46e).

12.5 Brain Cancer Diagnosis and Therapy with Nanoplatforms

Brain cancer is a life-threatening disease in which a minority of patients survive (only 5% for glioma brain tumor after 5 years) and which accounts for at least 13,000 deaths in the United States annually [12.142]. Late diagnosis and limitations of conventional therapies, which may result from inefficient delivery of the therapeutic or contrast agents to brain tumors, due to the blood–brain barrier (BBB; see Sect. 12.7) and non-specificity of agents, are major reasons for this unsolved clinical problem. The nanoparticle-based delivery has emerged as a potential method to improve the efficacy of the existing detection and treatment armamentarium due to the non-toxicity and the “engineerability” of nanoparticles. The desirable properties such as high payload, controlled drug release profile, tumor-specific targeting, long blood circulation time, and the ability getting across the BBB can be achieved by the nanoparticle delivery system. Multifunctionality is another advantage which could integrate detection, treatment, and tracking of tumor response, leading to informed decisions about further treatment [12.142].

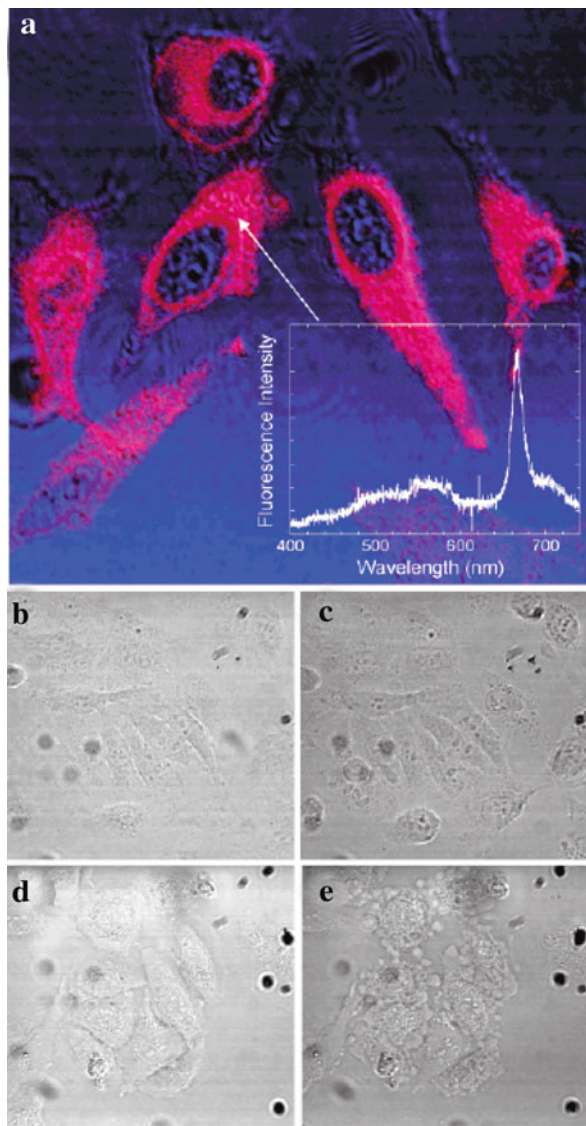


Fig. 12.46 (a) Transmission (blue) and 850 nm two-photon excited fluorescence (red) images of HeLa cells, stained with nanoparticles containing 1.1 wt% HPPH/20 wt% BDSA (see text). (b, c) Transmission images of HeLa cells treated overnight with nanoparticles containing 20 wt% BDSA and (d, e) 1.1 wt% HPPH and 20 wt% BDSA. *Left column (b, d):* before irradiation; *right column (c, e):* 15 min after 90 s of irradiation with femtosecond pulsed laser at 850 nm. (Reprinted with permission from [12.141]. © 2007 American Chemical Society)

12.5.1 General Comments

In the brain, the BBB cannot be overcome by other than passive diffusion (by which only small, lipid-soluble molecules can penetrate the brains), such as carrier/receptor-mediated influx or transcytosis (see [12.142]) for receiving essential metabolites such as glucose, aminoacids, and lipoproteins. These carrier/receptors can be used to deliver drugs to the central nervous system (CNS). It requires the discovery and development of receptor specific ligands, which can be attached directly to the drug of interest or the drug delivery system such as nanoparticles or liposomes. A “rule of thumb” suggests that nanoparticles less than 100 nm in diameter can enter cells, those with diameters below 40 nm can enter the cell nucleus and those that are smaller than 35 nm can pass through the blood–brain barrier and enter the brain [12.143]. In fact, some nanoparticles have been found to successfully cross the BBB. These nanoparticles are often coated with a surfactant (e.g., polysorbate) or are covalently linked to peptides. The exact mechanism of nanoparticle transport into the brain is not fully understood, but relies most likely on receptor-mediated endocytosis or passive leakage of nanoparticles across defects in the BBB [12.144]. Successful transport across an in vitro blood–brain barrier (BBB) has been shown for CdSe/CdS/ZnS quantum rods as targeted probes [12.145].

Several nanoparticle formulations have been clinically approved for MRI. Endorem® is approved for liver and spleen disease detection and Sinerem® (or Combinex®) is in phase III stage for the detection of metastatic disease in lymph nodes [12.142]. For cancer therapy, liposome-encapsulated formulations of doxorubicin were approved in 1995. A polymeric nanoparticle-based drug, albumin–paclitaxel was approved for breast cancer [12.146].

Nanoparticle sizes of 10–100 nm are believed to provide the best option because they are too large to undergo renal elimination and too small to be recognized by phagocytes (see [12.142]).

The amount of drugs such as Photofrin® for photodynamic therapy (PDT) or doxorubicin for cancer chemotherapy can be obtained by comparing the absorbance of the prepared nanoparticle sample solution with the calibration curve constructed from the mixture of free drug and blank nanoparticles of known concentration [12.142].

12.5.2 MRI Contrast Enhancement with Magnetic Nanoparticles

The magnetic resonance imaging (MRI) of the CNS is usually performed with short-lived gadolinium-based contrast agents, which gives rapid and transient imaging of brain and spinal permeability. Ultrasmall superparamagnetic iron oxide (USPIO) nanoparticles, with a 5–6 nm iron oxide core size surrounded by a dextran coating to give a 20–30 nm diameter, show also excellent potential for brain imaging. Unlike the pattern of enhancement with Gd chelate, which occurs immediately and decreases within hours, the contrast enhancement with USPIO occurs gradually, with a peak at 24–48 h after iron oxide administration [12.142].

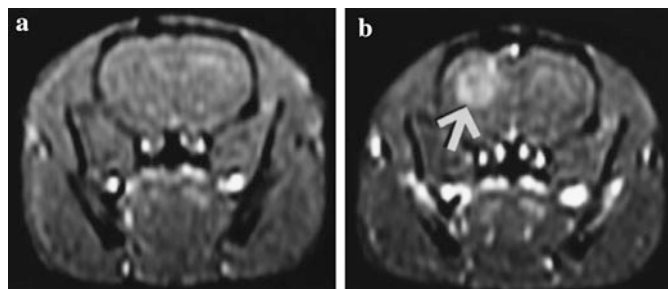


Fig. 12.47 Transverse gradient-echo magnetic resonance images (MRI) of a rat with 9L gliosarcoma tumor. The images were taken (a) before and (b) 24 h after intravenous administration of long-circulating dextran-coated iron oxide nanoparticles. After nanoparticle administration, the tumor (arrow) in the right hemisphere of the brain is enhanced because of nanoparticle accumulation and is clearly delineated against adjacent normal brain. Also note vascular enhancement. (Reprinted with permission from [12.147]. © 2000 Radiology Society of North America)

In vivo studies on rats bearing implanted 9L gliosarcoma or C6 glioma cells were performed after injection of dextran-coated iron oxide nanoparticles by MRI in a 1.5 T field with T_1 -weighted and T_2 -weighted imaging (Fig. 12.47). Accumulation of the nanoparticles in the brain, preferentially in the tumor periphery, was low (0.11% of the injected dose per gram of tumor tissue) but 10-fold higher than in the brain tissue adjacent to the tumor. The mechanism of MR enhancement by iron oxide nanoparticles appears to be leakage across the breached BBB, followed by intracellular trapping by reactive cells (e.g., astrocytes, macrophages) in and around the tumor, rather than by tumor cells [12.148].

Iron oxide nanoparticles tagged with the near-infrared fluorescent (NIRF) molecule Cy5.5 could potentially be used for both MRI and optical imaging in order to determine the brain tumor margins both during the presurgical planning phase (MRI) and during surgical resection (optical imaging) [12.149].

12.5.3 Nanoparticles for Chemotherapy

Chemotherapy of brain cancer has shown a poor outcome of most anti-cancer agents due to the low permeability through BBB. Nanoparticle delivery systems have emerged as promising brain cancer therapy tools due to the evidence for their ability to cross the BBB (see above), as discussed in the following.

Solid lipid nanoparticles (SLNs) loaded with the anticancer drugs paclitaxel or doxorubicin were studied. The SLNs with sizes below 100 nm to be loaded with paclitaxel were prepared from an emulsifying wax of an oil phase, water, and a surfactant [12.142]. The results of brain uptake in rats suggest that the paclitaxel uptake was significantly increased by the use of the nanoparticle delivery system. Another type of SLNs was loaded with the anti-cancer agent doxorubicin that inhibits DNA and RNA synthesis and cleaves DNA. Doxorubicin is a polar molecule that is not

known to be able to cross the BBB by normal intravenous injection. However, the doxorubicin concentration in liver, lung, or brain of rats was by a factor of 5–7 higher when the doxorubicin was administered in SLNs, compared to doxorubicin solution (see [12.142]).

Nanoparticles of poly(butylcyanoacrylate) (PBCA) were reported to achieve successful delivery of drugs to the brain by means of the surface-coated surfactant, polysorbate 80 (Tween®80). The favored transport of the polysorbate 80-coated particles has been suggested to be a receptor-mediated endocytosis by the brain endothelial cells. The studies on rats showed that the polysorbate 80-coated PBCA nanoparticles loaded with doxorubicine (DOX-NP/PS) produced a very high doxorubicin concentration in the brain whereas this concentration was below the detection limit in control preparation with unconjugated doxorubicin and doxorubicin-loaded uncoated PBCA nanoparticles. This suggests that polysorbate 80-coated PBCA nanoparticles could be an efficient delivery system for chemotherapy of brain cancer. The survival rates of rats, intracranially implanted with 101/8 glioblastoma in their brains and treated with DOX-NP/PS [12.150], showed a significant increase compared to control groups without treatment or with doxorubicin solution treatment. Biodistribution studies of PBCA nanoparticles showed highest concentrations in the brain after DOX-NP/PS treatment and significantly higher brain concentrations in rats 10 days after tumor implantation than in healthy rats. This demonstrates the selective delivery of appropriate nanoparticles to a tumor via the “leaky” tumor vasculature which is called the enhanced permeability and retention (EPR) effect (see [12.142]). The studies, in addition, indicate the therapeutic potential of DOX-NP/PS nanoparticles for the treatment of human glioblastoma.

12.5.4 Targeted Multifunctional Polyacrylamide (PAA) Nanoparticles for Photodynamic Therapy (PDT) and Magnetic Resonance Imaging (MRI)

It has been shown that the use of nanoparticles in PDT is a promising approach for killing tumor cells [12.151]. PDT for brain cancer treatment has been investigated using PAA nanoparticles [12.152]. Specifically, a targeted multifunctional nanoplatform [12.153, 12.154] combining PDT and MRI has been designed for synergistic cancer detection, diagnosis, and treatment (Fig. 12.48). The non-toxical PAA core particle carries the following components: (1) PDT agent Photofrin® which is a photosensitizer approved for clinical use in the United States; (2) MRI-detectable iron oxide nanoparticle contrast agent for good in vivo MRI efficacy; (3) vascular targeting ligand (e.g., F3 peptide). Systemic PDT, i.e., optical generation of singlet oxygen to attack diseased tissue, is particularly effective when it leads to complete ischemia of solid tumors through localization in the vascular space. Vascular targeting of a photosensitizer is required for irreversible damage of the tumor vascular system resulting in tumor necrosis [12.155]. The F3 peptide

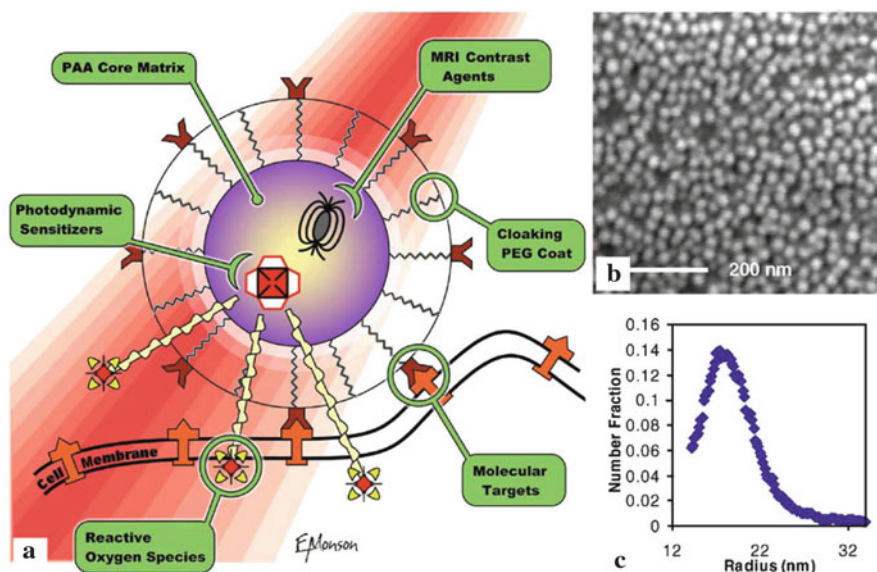


Fig. 12.48 Nanoparticle platform for magnetic resonance imaging (MRI) and photodynamic therapy (PDT) of brain cancers. (a) Schematic nanoparticle with photodynamic dye, MRI contrast enhancing agent, PEG cloaking, and molecular targeting. (b) SEM image of polyacrylamide (PAA) nanoparticles. (c) Nanoparticle size distribution derived from light scattering. (Reprinted with permission from [12.152]. © 2005 Elsevier)

is a 31-amino acid fragment of human high-mobility group protein 2 (HMGN2), which targets to and gets internalized into tumor endothelial cells and cancer cells through the nucleolin receptor [12.156]; (4) polyethylene glycol (PEG) providing longevity of the nanoparticle. The typical size of the PAA nanoparticle is 30–70 nm [12.142].

The *in vivo* PDT therapeutic activity of the targeted and untargeted nanoparticles containing Photofrin® was evaluated by diffusion MRI of rats bearing intracerebral 9L gliosarcoma tumors. Diffusion MRI relies upon the ability of MRI to quantify the diffusivity of water molecules in tissues and examines the changes of the apparent diffusion coefficients (ADC) within the tumor tissue [12.157]. The increase in tumor diffusion values corresponds to a loss of tumor cellularity within the region under study. The administration of F3-targeted Photofrin®-encapsulated nanoparticles resulted in the most significant increase in mean tumor ADC values, well correlated to the animals survival periods. Gliomas treated by Photofrin®-containing nanoparticles (Fig. 12.49b), followed by laser irradiation for PDT, produced massive regional necrosis, demonstrated by huge “bright” regions in the images, resulting in shrinkage of the tumor mass. The untreated 9L gliomas continued to grow over the life span of the animals (Fig. 12.49a). The mechanism of the efficient PDT activity appears to result from efficient targeting of the nanoparticles to the tumor vascular cells (see [12.142]).

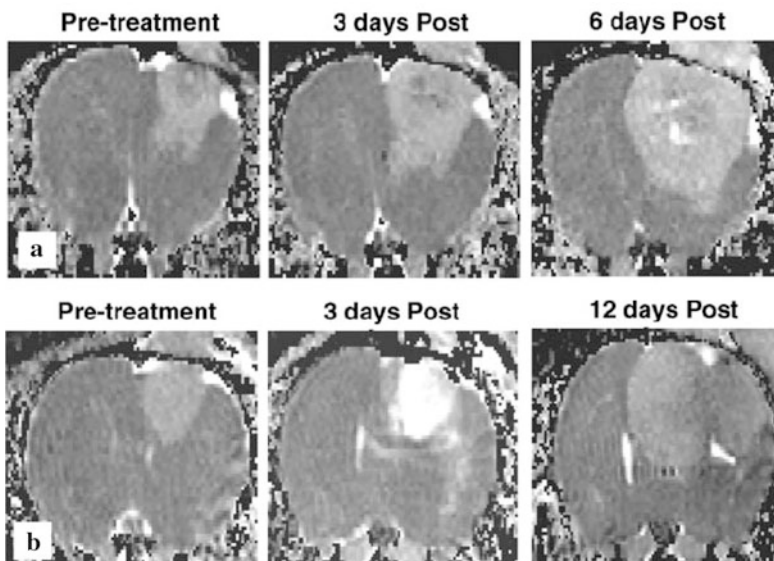


Fig. 12.49 Time series of water diffusivity maps by magnetic resonance imaging (MRI) images of a 9L glioma rat tumor after *in vivo* PDT: (a) untreated; (b) treated with laser light and Photofrin[®]-containing PAA nanoparticles. The images shown here are not diffusion-weighted images but rather computer-generated quantitative diffusion maps where the intensity of each pixel (voxel) is proportional to the diffusivity values. (Reprinted with permission from [12.152]. © 2005 Elsevier)

In future clinical application, total eradication of brain cancer by nanoparticle-based PDT may be possible at an early or intermediate stage and the detection could be made by the same multifunctional nanoparticle. The option of non-invasive direct illumination from outside the skull may need the development of a photosensitizer with a longer absorption wavelength than Photofrin[®], for deeper photon penetration [12.142].

The nanomaterial is clearing at two different rates over a 90-day sampling interval, through a complex process of degradation and elimination of the nanoparticle constituents [12.142].

12.6 Hyperthermia Treatment of Tumors by Using Targeted Nanoparticles

The potential of hyperthermia and thermal ablation in cancer therapy has been well noted [12.158]. Temperatures between 42 and 46°C lead to inactivation of normal cellular processes, whereas above 46°C, extensive necrosis occurs [12.159]. The inability to safely induce a therapeutic response, because of difficulties in inducing selective tumor heating and facilitating heat dose determination, has limited its

widespread use in clinical therapy [12.159]. In the following the tumor treatment by heating of tumor-targeted nanoparticles by means of (i) an alternating magnetic field [12.159], by (ii) a radiofrequency field [12.160], or by (iii) near-infrared light [12.161, 12.162] will be discussed.

12.6.1 Alternating Magnetic Fields for Heating Magnetic Nanoparticles

Tumor cell immunotargeted magnetic nanoparticles can be heated to cytotoxic temperatures due to their response to an externally applied alternating magnetic field (AMF). For an *in vivo* study [12.159] of the therapy of a human breast cancer xenograft (HBT 3477) in mice, superparamagnetic iron oxide nanoparticles (Fig. 12.50a) were conjugated to human–mouse chimeric antibodies (ChL6 mAb) for tumor targeting. These antibodies react with a membrane glycoprotein highly expressed in human breast carcinomas and to the ^{111}In isotope (half-life 2.8 days) for pharmacokinetic and blood clearance studies. The iron oxide nanoparticles were coated with dextran and impregnated with poly(ethylene glycol) (PEG) (Fig. 12.50a). Pulsed alternating magnetic fields with an oscillation frequency of 153 kHz and an amplitude of ~ 0.1 T (see Fig. 12.50b) applied for 20 min (total heat dose 13–21 J/g tumor) to the mice subcutaneously injected with the conjugated nanoparticles (power absorption rate ~ 70 W/g) gave rise to a substantial tumor growth delay in response to the heat dose (Fig. 12.51a). In addition, electron microscopy showed normal appearance of the tumor cells after nanoprobe

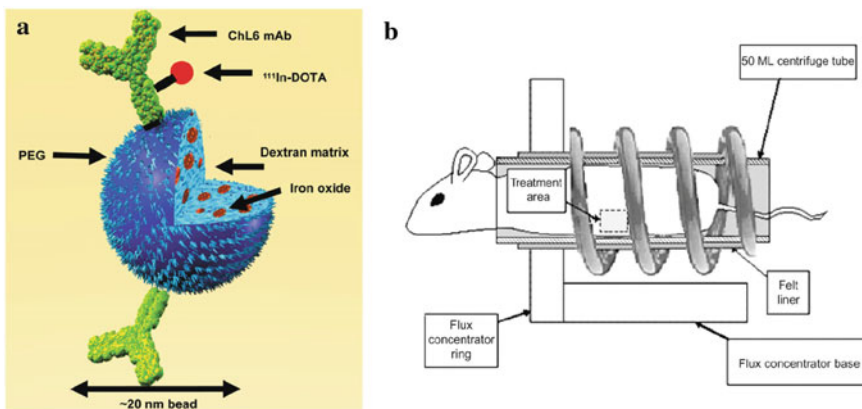


Fig. 12.50 (a) Schematic of a bioprobe for alternating magnetic field heating of tumors: ^{111}In -ChL6 conjugated to poly(ethylene glycol) (PEG) on iron oxide impregnated dextran 20 nm nanoparticles. (b) Coil for the delivery of the alternating magnetic field (AMF) to treat mice-bearing human xenograft tumors. AMF is focused in a 1 cm band in which the subcutaneous tumor located on the abdomen of the mouse was positioned. (Reprinted with permission from [12.159]. © 2007 Society of Nuclear Medicine)

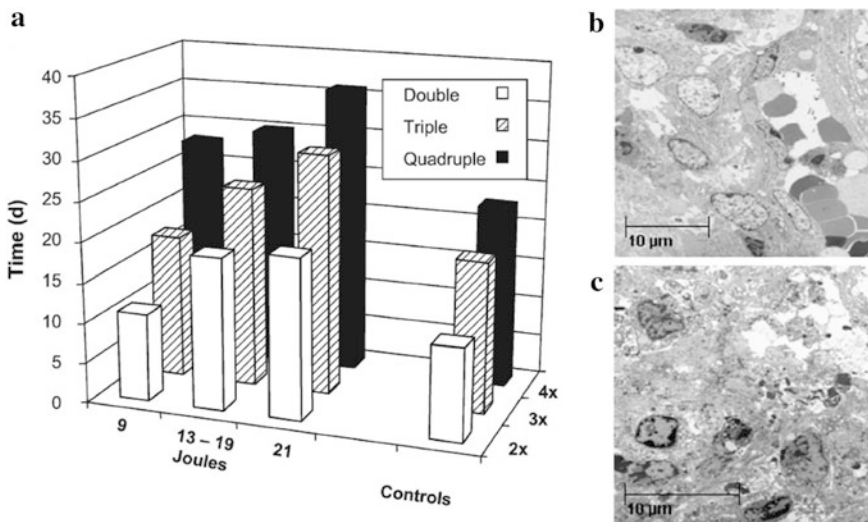


Fig. 12.51 (a) Relationship of tumor response to bioprobe AMF (alternating magnetic field) tumor-specific thermal therapy. The therapeutic response is reflected by the increased time to double, triple, or quadruple the tumor volume in mice with the tumor total heat dose (J) indicated, with a relationship between response and heat dose, compared with controls (tumor growth of AMF treatment alone, untreated control groups). (b, c) Electron micrographs of ultrathin osmium tetroxide-fixed epoxy-embedded HBT 3477 xenografts that had been excised from mice at time of sacrifice, 48 h after bioprobe injection, no AMF (b), and 48 h after AMF tumor-specific thermal therapy 18 J/g; (c) Viable tumor cells (b) contrast with evidence for cell necrosis at 48 h after AMF tumor-specific thermal therapy (c). (Reprinted with permission from [12.159]. © 2007 Society of Nuclear Medicine)

uptake prior to AMF treatment, however, progressive tumor cell necrosis after AMF treatment with no effect on the normal tissue [12.159].

In a first clinical application, interstitial hyperthermia employing 15 nm superparamagnetic ferrite nanoparticles with an aminosilane coating was applied for the treatment of prostate cancer [12.163] with guidance by computer tomography (CT) and transrectal ultrasound (TRUS) imaging. According to the individual anatomy of the prostate with a normal volume of 20 ml and the specific absorption rate (SAR) of the magnetic fluid (~ 0.3 W/g), the number and positions of magnetic fluid depots were calculated, while rectum and urethra were spared. The nanoparticle suspensions were injected transperineally into the prostate under ultrasound guidance (see Fig. 12.52a). For invasive thermometry, fiberoptic thermometry probes were positioned in the prostate, urethra, rectum, perineum, scrotum, and left ear, yielding in a 0.005–0.0063 T AC field maximum temperatures of 48.5°C in the prostate (thermoablative range; see Fig. 12.53), of 42.2°C in the urethra, and 42.1°C in the rectum. Selective uptake of nanoparticles into prostate cancer cells [12.164] offers the perspective of tumor cell selective hyperthermia. These first clinical results prompted a phase I study to evaluate the feasibility, toxicity, and quality of life during hyperthermia using magnetic nanoparticles in patients with local recurrence of

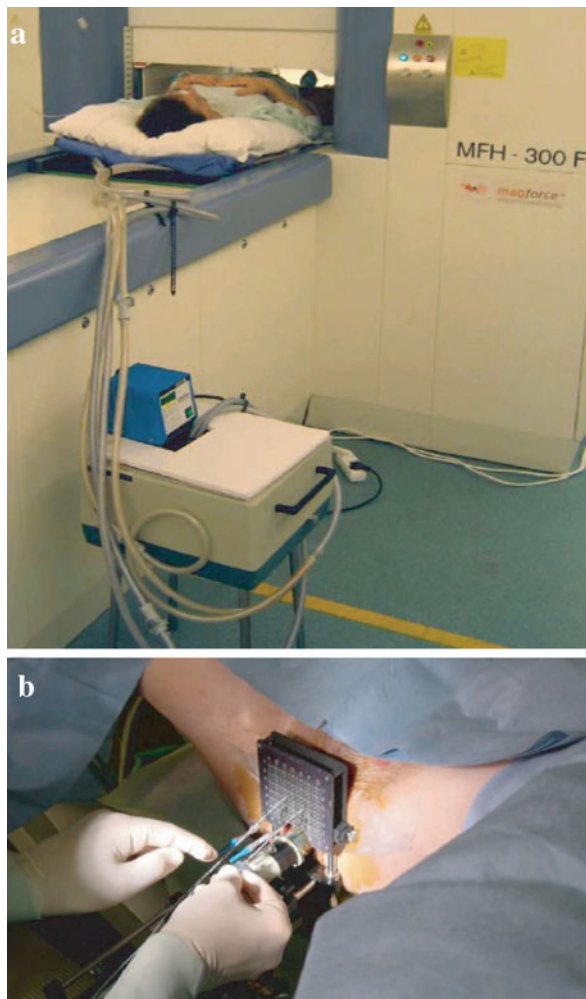


Fig. 12.52 (a) AC magnetic field applicator (MFH300F, MagForce[®] Nanotechnologies GmbH, Berlin). For cooling, hoses with circulating cold water are placed around the patients inner thigh, perineum, and the groin on both sides. An AC magnetic field with a frequency of 100 kHz and amplitudes of 0–0.023 T are used. Thermometers are positioned in the prostate, urethra, rectum, perineum, scrotum, and left ear. Hyperthermia is monitored online, so that the AC field amplitude can be kept constant or adjusted to a constant temperature in the tumor. (b) The administration of the nanoparticle suspension into the prostate is carried out transperineally with the patient in a lithotomy position. At the center, the template used for magnetic fluid injection as well as implantation of catheters to house the thermometry probes can be seen. (Reprinted with permission from [12.163]. © 2005 Taylor and Francis)

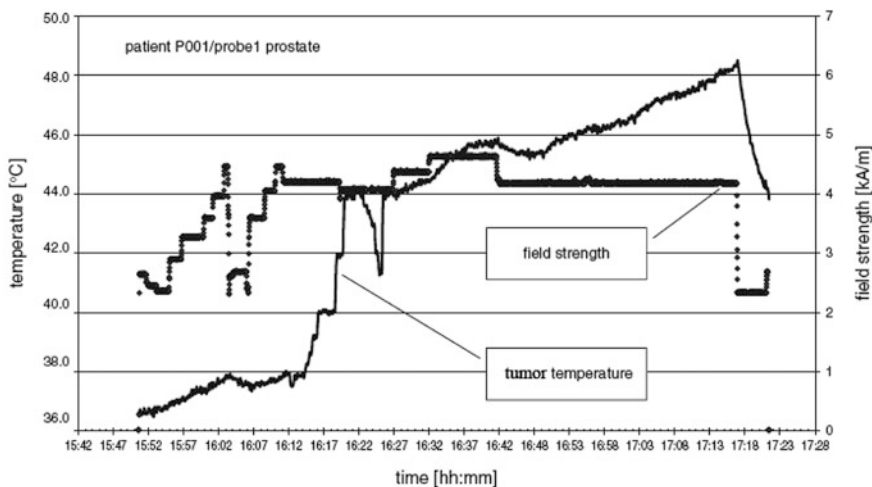


Fig. 12.53 Variation of the AC magnetic field strength and of the prostate temperature with time. (Reprinted with permission from [12.163]. © 2005 Taylor and Francis)

prostate cancer [12.163]. A clinical trial of magnetic field hyperthermia is performed with 69 patients [12.165].

12.6.2 Radiofrequency Heating of Carbon Nanotubes

Radiofrequency ablation (RFA) of malignant tumors [12.166] is currently an invasive treatment that requires the insertion of needle electrodes directly into the tumor to be treated; incomplete tumor destruction occurs in 5–40% of the treated lesion, with thermal necrosis in both malignant and normal tissues surrounding the needle electrode [12.160]. Conversely, it is known that the tissue penetration by radiofrequency (RF) fields is excellent. Thus, non-invasive RF treatment of malignant tumors at any site in the body should be possible if agents that convert RF energy into heat can be delivered to the malignant cells. In order to study this approach, direct intratumoral injection of single-walled carbon nanotubes (SWNTs) was performed followed by RF field treatment. This was tolerated well by rabbits bearing hepatic VX2 tumors which are particularly aggressive and resistant to standard cancer therapies [12.167]. At 48 h after RF treatment, all SWNT-treated tumors demonstrated complete necrosis, whereas control tumors treated with RF without SWNTs remained completely viable. Tumors that were injected with SWNTs but were not treated with RF were also viable. The remaining liver after histopathology section of the liver tumor and all other organs that were assayed had no evidence of thermal injury or other abnormalities [12.160] (Fig. 12.54).

The SWNTs, functionalized with Kentera [12.160], a polymer based on polyphenylene ethynylene for water solubility, were injected into an intrahepatic VX2 tumor (greatest dimension, 1.0–1.3 cm) with a subsequent treatment for 2 min

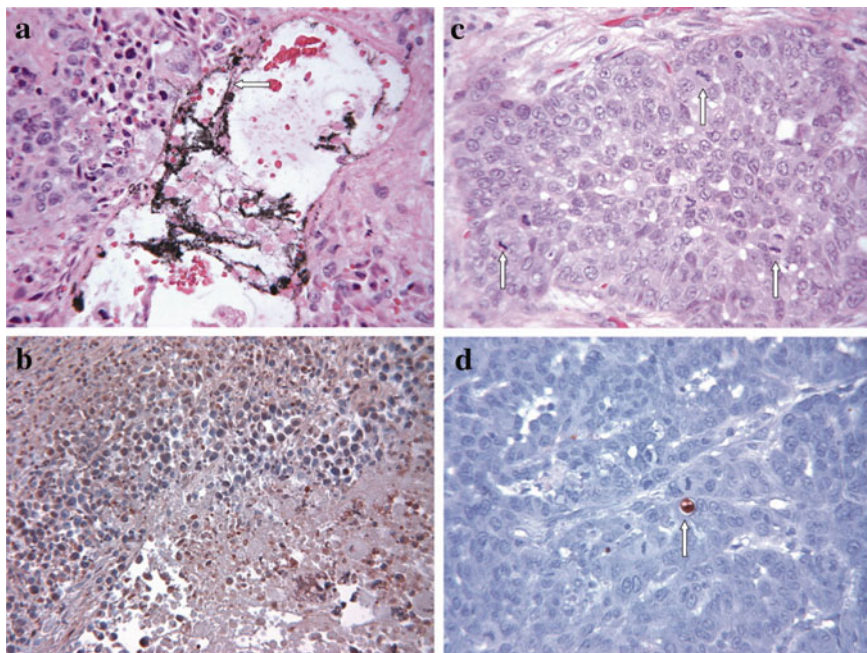


Fig. 12.54 (a, b) Photomicrographs of hepatic VX2 tumors from rabbits that received intratumoral injection of Kentera single-walled carbon nanotubes (SWNTs) followed by 2 min of radiofrequency (RF) field treatment. (a) Necrotic tumor cells, inflammatory cells, and black strands of SWNTs (arrow), standard hematoxylin and eosin staining – H&E; magnification \sim x400. (b) Characteristic brown staining observed with apoptotic and necrotic cells (stained with terminal deoxynucleotidyltransferase biotin–deoxyuridine triphosphate nick-end labeling – TUNEL; magnification \sim x250). (c) Hepatic VX2 tumors after intratumoral injection of Kentera polymer alone (no SWNTs) followed by RF treatment showing completely viable tumor cells with numerous mitotic bodies (arrows, standard H&E staining, magnification \sim x400). (d) Viable cells with only a rare brown apoptotic cell-TUNEL staining; magnification \sim x400). The rate of apoptosis in untreated VX2 tumors was 2–3%, and the control tumors treated with RF but no SWNTs had a similar 2–3% incidence of apoptotic cells. (Reprinted with permission from [12.160]. © 2007 Wiley Interscience)

in an RF field of 13.56 MHz for heating of the SWNTs. This frequency produces minimal heating of mammalian tissue [12.168]. The efficient RF heating of the SWNTs may be based on their resistive conductivity [12.169]. The development of cell-specific delivery and uptake of appropriately functionalized SWNTs is desirable for the future [12.160]. The absence of SWNT-related toxicity and no or minimal growth inhibition in three human cancer cell lines [12.160] is consistent with other reports [12.170, 12.171]. Nevertheless, for the assessment of the complete safety of SWNTs in animals or humans, long-term studies are required.

Treatments by heating carbon nanotubes inside cells by near-infrared laser light [12.172] are restricted to tissue depth of 2–3 cm. The specific power deposition in carbon nanotubes (75000 W/g) in RF fields exceeds that of iron oxide nanoparticles

in alternating magnetic fields (500 W/g) (see [12.160]), so that in the former case less nanomaterial is required for treatment.

12.6.3 Light-Induced Heating of Nanoshells

Light-induced heating of nanoshells has also been demonstrated for efficient destruction of tumors [12.161] where, in contrast to nanoparticle heating in a alternating magnetic field [12.159], lower quantities of nanoparticles are required. In metal nanoshells (Fig. 12.55), the plasmon resonance and the resulting optical absorption can be adjusted from near-UV to mid-infrared [12.162] for exploitation in photothermal ablation of cancer cells *in vivo*. The plasmon resonance and, therefore, the light-induced heating of silica nanoparticles (110 nm in diameter) with a 10 nm gold shell is maximum in the near-infrared (NIR) range (820 nm) where optical transmission through tissue is optimal, so that deep tissue treatment (~ 1 cm) is feasible. These nanoshells are far less susceptible to chemical/thermal denaturation and photobleaching effects than conventional NIR dyes and exhibit a 1 million times higher absorption cross section ($\sim 4 \times 10^{-14} \text{ m}^2$) than those dyes (see [12.161]). After injection of the nanoshells into a canine transmissible venereal

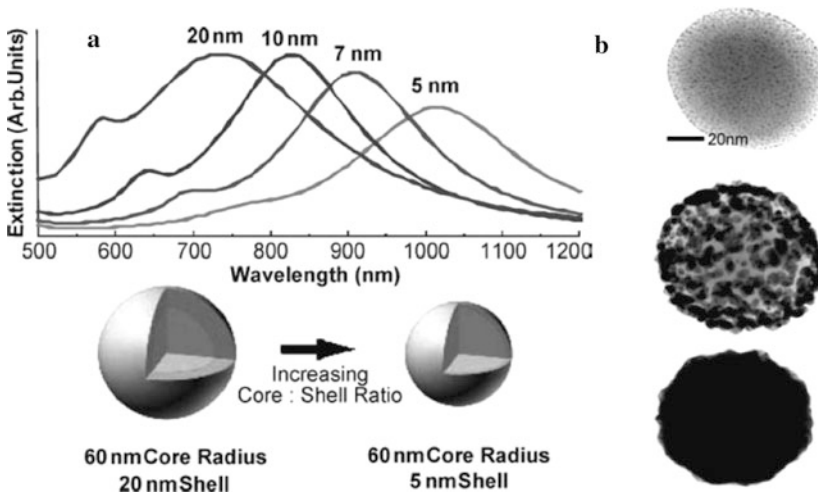


Fig. 12.55 Plasmon resonance of SiO₂-Au core-shell nanoparticles. (a) The optical tunability is demonstrated for nanoshells 5, 7, 10, and 20 nm thick on a 50 nm radius silica core. The plasmon resonance (extinction) of the particles red shifts with decreasing thickness of the Au shell. Nanoshells with resonances in the near infrared (NIR; 800–1200 nm) can be easily fabricated, with still greater tunability making use of multilayered structures. (b) Series of TEM images of gold colloids (dark dots) growing into a complete shell on a silica core structure. (Reprinted with permission from [12.162]. © 2003 National Academy of Sciences USA)

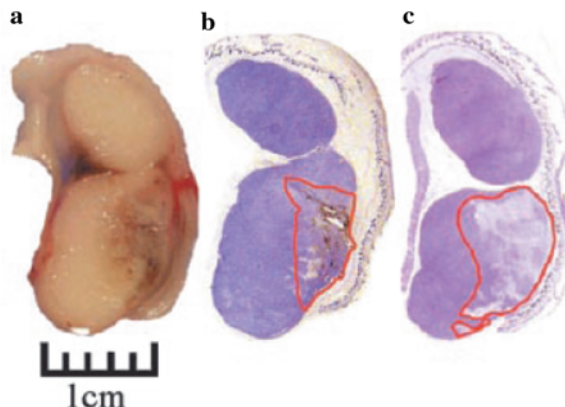


Fig. 12.56 (a) Gross pathology of a canine transmissible venereal tumor (TVT) in a mouse after nanoshell injection and NIR illumination reveals hemorrhaging. (b) Silver staining of the tissue section reveals the region of localized nanoshells (outlined in red). (c) Hematoxylin/eosin staining within the same plane clearly shows tissue damage within the area occupied by nanoshells. (Reprinted with permission from [12.161]. © 2003 National Academy of Sciences USA)

tumor (TVT) xenograft in a mouse, the tumor was exposed to external NIR light (820 nm, 20 W/cm², < 6 min) irradiation, giving rise to irreversible tissue damage (Fig. 12.56) due to radiation-induced temperature increase by ~37°C. This temperature increase was measured by magnetic resonance temperature imaging (MRTI) based on the temperature dependence of the proton resonance frequency shift [12.173]. The above laser dose is more than 10-fold less than that used in earlier studies examining indocyanine green dye [12.174]. Nanoshell-free control experiments with the same light irradiation saw average temperature increases of ~9°C leading not to tissue damage. The findings of the tumor tissue damage due to light absorbed in nanoshells correlate well with gross pathology (Fig. 12.56a), in which defined zones of edema were observed in the nanoshell-treated tumors in the region where MRTI suggested that there should be irreversible tissue damage. Histology also identified common markers of thermal damage in NIR/nanoshell-treated tumors (Fig. 12.56c). In addition, in regions of thermal damage, nanoshells were found by using a silver enhancement stain that amplifies the size of the nanoparticles for examination by optical microscopy (Fig. 12.56b). Due to the preferential accumulation of nanoshells in the tumor because of the enhanced permeability and retention effect [12.175], only the tumor regions within the tissue are destroyed, leaving surrounding tissue intact. Furthermore, nanoshells may be conjugated with antibodies targeting surface oncoproteins overexpressed within the tumor (see [12.161] and Fig. 12.57).

Tumor cells can also be selectively killed *in vitro* by specifically targeting them by single-walled carbon nanotubes which are heated by the absorption of near-infrared light [12.177].

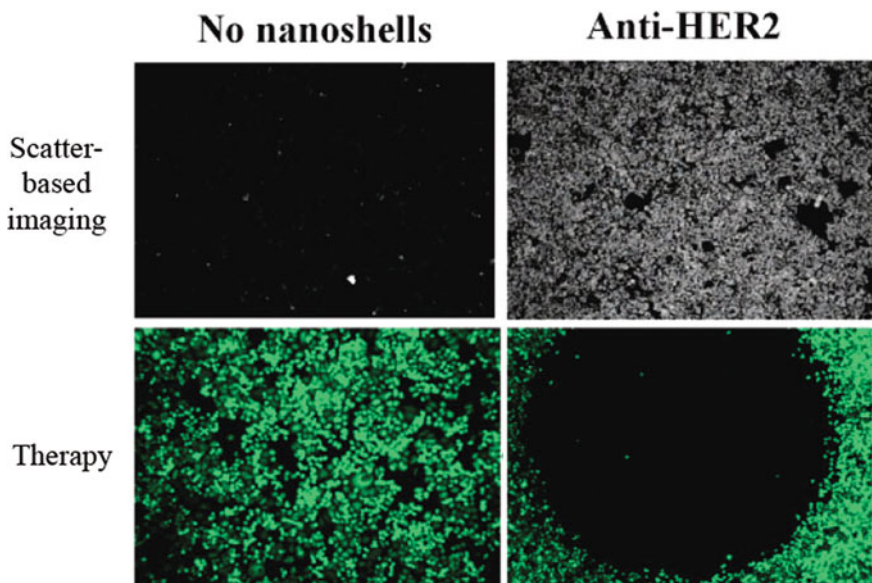


Fig. 12.57 Combined imaging and therapy of SKBr3 breast cancer cells using Au nanoshells targeted against HER2 expressed by the cancer cells. Scatter-based dark-field imaging of HER2 expression enabled by nanoshells conjugated to the cancer cells (top row, right). The cell viability is assessed via calcein staining (bottom row). Cytotoxicity (dark spot; bottom row, right) is observed only in cells heated by the Au nanoshells absorbing the near-infrared light of laser illumination compared to the control without nanoshells (bottom row, left). (Reprinted with permission from [12.176]. © 2005 American Chemical Society)

12.7 Nanoplatforms in Other Diseases and Medical Fields

12.7.1 Heart Diseases

Heart failure is a highly prevalent form of cardiovascular disease with ~300,000 deaths in 2004 in the United States and annual costs associated with diagnosis, monitoring, and therapy estimated to be >US \$25 billion in the United States (see [12.178]). Clinical biomarkers are of particular importance for diagnosis and prognosis of heart diseases. A nanotechnology for detecting cardiac troponin I (cTnI) – a principal biochemical marker of acute myocardial infarction [12.179] – has been reported [12.180] in addition to conventional techniques developed earlier [12.181, 12.182].

In the heart, cTnI forms a protein complex with troponin T and troponin C. The troponin complex is broken up following myocardial damage, and the individual protein components are released into the bloodstream [12.183]. For the detection of cTnI, the electrode of an electrochemical immunoassay (voltammetry), which is a biosensor with antibodies as biological elements, is functionalized with the

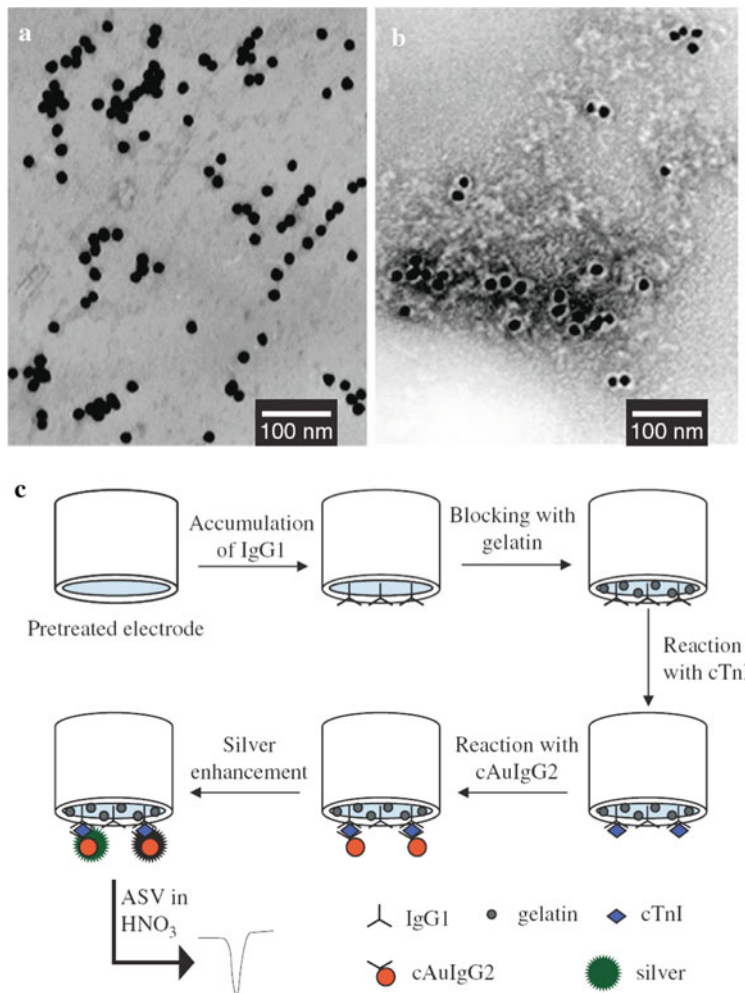


Fig. 12.58 TEM images of (a) unlabeled and (b) gold nanoparticles labeled with IgG2 detection antibodies. (c) Protocol format in the analytical procedure for the diagnosis of acute myocardial infarction by the detection of the cTnI biochemical marker via Au nanoparticles conjugated to IgG2 antibodies (cAuIgG2). (Reprinted with permission from [12.180]. © 2005 American Scientific Publishers)

capture antibody IgG1 for immunoreaction with the cTnI sample (Fig. 12.58c). After that, the reaction with gold nanoparticles labeled with the detection antibody IgG2 (cAuIgG2; Fig. 12.58a, b) is performed with final catalytic deposition of silver on the gold nanoparticles, yielding a peak in the anodic stripping voltammogram (ASV). The magnitude of this peak reflects the amount of cTnI in the serum with a detection limit of 0.8 ng/ml of cTnI. The cTnI concentrations determined by this nanotechnology fully coincide with the values obtained by enzyme-linked

immunoadsorbent assays (ELISA) [12.180]. This nanotechnology for the diagnosis of acute myocardial infarction may be important in the early phase of the disease where the symptoms are ambiguous, may shorten the assay time, and reduce costs by decreasing reagent consumption [12.180].

Using virus-derived nanoparticles, a highly sensitive and specific assay system for the specific marker troponin I of acute myocardial infarction (AMI) has been developed [12.184]. This assay can detect troponin levels that are 6–7 orders of magnitude lower than those detected by conventional enzyme-linked immunosorbent assays (ELISA).

12.7.2 Diabetes

Diabetes mellitus comprises a group of metabolic disorders characterized by high blood glucose resulting from reduced insulin secretion, decreased glucose utilization, or increased glucose production. At least 20 million people have diabetes in the United States (see [12.185]). Diabetes can lead to serious vascular complications, which include coronary heart disease, cerebrovascular disease, as well as peripheral vascular disease, and microvascular complications like diabetic retinopathy (DR), which makes diabetes the leading cause of new cases of blindness among adults (see [12.185]).

Oral delivery of insulin is not an effective diabetes therapy because of its susceptibility to enzymatic degradation in the gastrointestinal (GI) tract and low permeability across the intestinal epithelium [12.186, 12.187]. However, polymeric vesicles are thought to be potentially advanced candidates for the oral delivery of insulin as briefly discussed in the following [12.188]. Block copolymers comprising commercial Pluronic® F127 (PEO-PPO-PEO) and poly(lactic acid) (PLA) have been synthesized to PLAF 127-29 vesicles (molecular weight 29 kDa) with a radius of 56 nm (Fig. 12.59a, b) to be loaded with insulin. The nanoparticles within this size range exhibit a high circulation time in the human body and a good bioavailability. A biphasic in vitro insulin release behavior was found for the insulin-loaded PLAF 127-29 vesicles (Fig. 12.59c) due to diffusion control in the vesicles [12.188]. After in vivo oral administration of insulin-loaded PLAF 127-29 vesicles to mice, a minimum blood glucose concentration of 25% of the initial concentration was observed after 5 h and this concentration was maintained for at least an additional 18.5 h which is in contrast to the behavior of free oral insulin or subcutaneous insulin administration (Fig. 12.59d). There could be two reasons for the prolonged hypoglycemic effect (reduced glucose concentration in the blood) of insulin-loaded PLAF 127-29 vesicles. First, the insulin is protected from degradation by enzymes in the GI tract due to the PLAF 127-29 coating of the vesicles, so that the insulin load could reach the specific regions for favorable insulin absorption and nanoparticle uptake in the distal jejunum and in the ileum where abundant Peyer's patches exist (important in the immune surveillance of the intestinal lumen). Second, both the small size and the strong interaction of PEO blocks in the PLAF 127-29 block copolymer with the intestinal wall should be responsible for the delayed GI transit

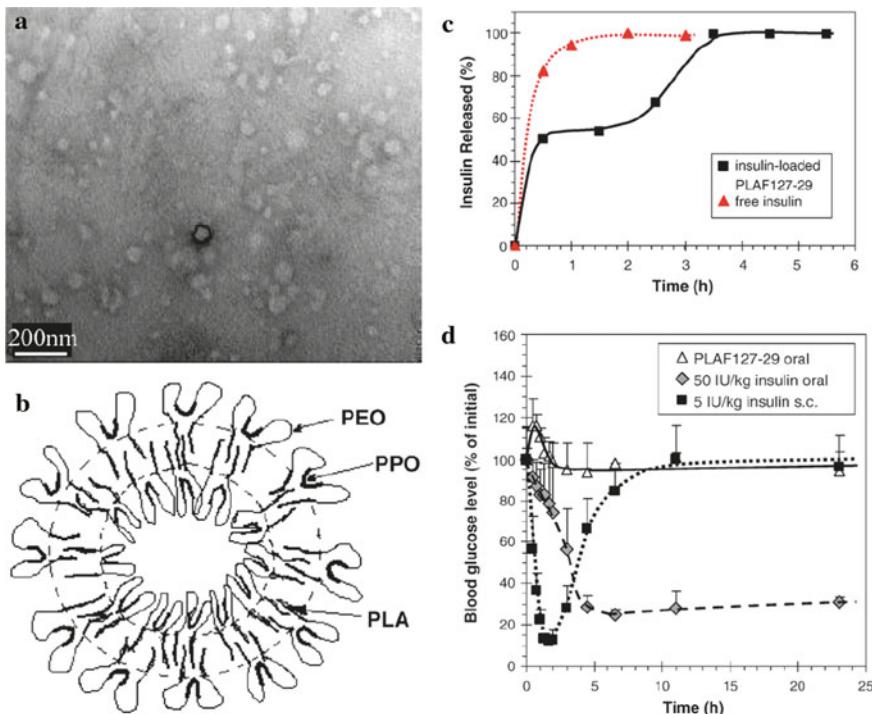


Fig. 12.59 (a) Transmission electron micrograph of PLAF 127-29 polymer vesicles (see text) and (b) possible microstructure. (c) The in vitro release behavior of insulin-loaded PLAF 127-29 vesicles in phosphate buffer saline. (d) Time dependence of the glucose level following oral administration of insulin-free PLAF 127-29 vesicles to control mice (PLAF 127-29 oral), insulin-loaded PLAF 127-29 vesicles (50 IU/kg), and subcutaneous injection of free insulin (5 IU/kg insulin s. c.). (Reprinted with permission from [12.188]. © 2007 Elsevier)

of the insulin – PLAF 127-29 vesicles, giving rise to the prolonged hypoglycemic effect. Therefore, the present nanoparticles may be promising carriers for oral insulin delivery [12.188].

12.7.3 Lung Therapy – Targeted Delivery of Magnetic Nanoparticles and Drug Delivery

Despite progress in optimizing aerosol delivery to the lung for the treatment of lung disorders such as asthma, cystic fibrosis, or lung cancer, targeted aerosol delivery to specific lung regions other than the airways or the lung periphery has not been achieved adequately to date [12.189]. However, it has been shown by simulation and experimentally in mice [12.190] that targeted delivery of aerosol droplets comprising superparamagnetic iron oxide nanoparticles can be achieved in combination with a target-directed magnetic field gradient. This may be useful

for treating localized lung disease, by targeting foci of bacterial infection or tumor nodules.

In simulative calculations of the magnetic field-gradient guided deposition of inhaled superparamagnetic iron oxide nanoparticles (SPIONs) in the lung, it turned out that the forces exerted by a field gradient (Fig. 12.60a) on a single 50 nm multidomain core SPION containing 5 nm single-domain magnetite nanoparticles would not be sufficient to efficiently guide the SPIONs [12.190]. In contrast, when a multitude of, e.g., 2930 SPIONs are assembled in an aqueous aerosol droplet, this is

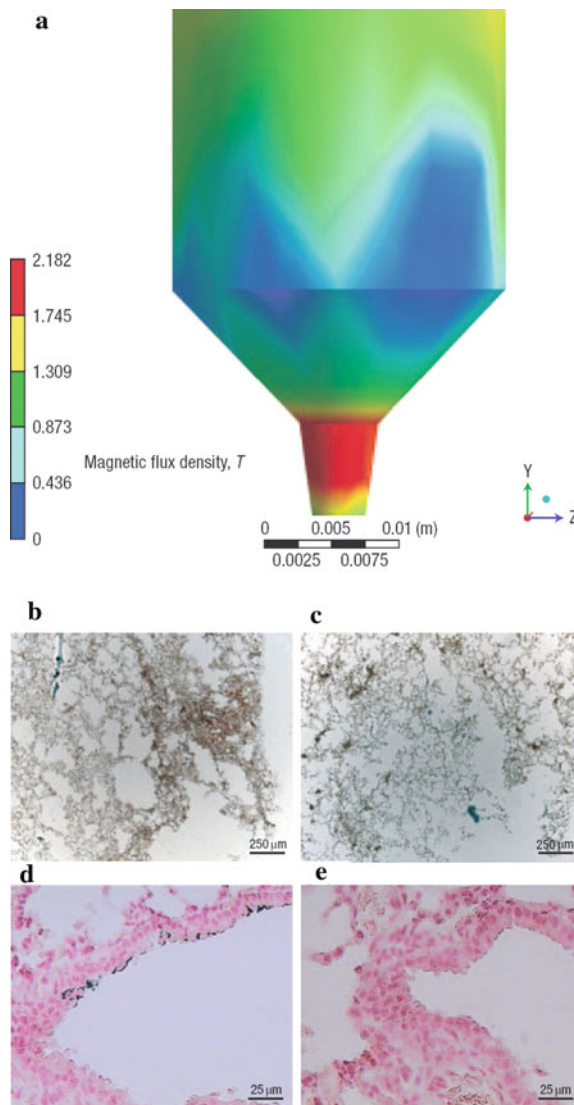


Fig. 12.60 (a) Iron–cobalt core tip surrounded by coil windings (not shown) for the generation of a high-gradient magnetic field for targeted delivery of superparamagnetic iron oxide nanoparticles (SPIONs). The magnetic flux density is shown in a multicolor representation. (b–e) Lung histology after inhalation of magnetic nanoparticles by a mouse with the magnetic tip (a) above the right lung lobe (b, d; left lung; c, e). The magnetic nanoparticles (brown color) accumulate in the focused area of a high magnetic field gradient in the right lung lobe (b, d) but not in the left lung tissue without a magnetic field (c, e). (d, e) Prussian blue staining of the SPIONs (d) and hematoxylin staining of the lung cells (d, e). (Reprinted with permission from [12.190]. © 2007 Nature Publishing Group)

predicted to result in aerosols guidable by technically feasible magnetic field gradients ($\nabla B > 100 \text{ Tm}^{-1}$) in the proximity of a magnetic tip (Fig. 12.60a). In a simple model calculation, the SPION concentration deposited in a magnetized lung airway exceeded that in an airway without a magnetic field by a factor of 3.

In experiments on mice [12.190] it could be shown by histology that SPIONs were accumulated in an eightfold higher concentration in the right lung lobe exposed to a field gradient, compared with the left lobe in zero field (Fig. 12.60b, c). SPIONs could be identified on the magnetized surface of alveolar cells and on airway epithelial cells exposed to a magnetic field gradient (Fig. 12.60d, e). In order to demonstrate the potentials for drug delivery, plasmid DNA (pDNA) was formulated in the SPION aerosol droplets and a twofold higher dose of pDNA was detected in the magnetized right mouse lung than in the left lung without magnetic field. Several drugs can be administered simultaneously and other pharmaceutically relevant nanocarriers could be co-delivered with the SPIONs. It should be emphasized here that the biocompatibility and clinical feasibility of SPIONs has been proven by their years of clinical use as contrast agents in magnetic resonance imaging [12.191]. Scaling up of the magnetic field gradient to address the size of the human lung represents the major challenge, although high field-gradient electromagnets for use in magnetic drug targeting in pigs are already available [12.192, 12.193].

12.7.4 Alzheimer's Disease (AD)

The prevalence of most neurodegenerative disorders increases dramatically with advancing age. For example, Alzheimer's disease – the most prevalent of these disorders – affects ~15 million people worldwide today [12.194] and will give rise to financial, societal, and emotional cost staggering in the future. The disease is caused by plaques and tangles of protein in the brain. However, therapeutic strategies to probe the central nervous system (CNS) are limited by the blood–brain barrier (BBB). This barrier can be overcome by polymeric nanoparticles as drug carriers [12.195].

Senile plaques and neurofibrillary tangles were discovered by Alois Alzheimer [12.196] in the neocortex and hippocampus of a woman with memory deficits and a progressive loss of cognitive function. Neurodegeneration affects the cognition (learning, abstraction, judgement, etc.) and the memory with behavioral consequences such as aggression, depression, delusion, anger, and agitation (see [12.195]).

According to the amyloid cascade hypothesis (see [12.197]) Alzheimer's begins with the build up of amyloid-beta (A-beta), which is carved from the amyloid-beta precursor protein (APP). In a first step [12.197], the enzyme beta-secretase cuts APP outside the cellular membrane with the help of aspartic acids that make water molecules more reactive. Then the presenilin protein, a component of the gamma-secretase enzyme, cuts the remaining stump inside the membrane, releasing A-beta [12.197]. The reason why cells make A-beta is unclear, but current evidence suggests that the process is part of a signaling pathway (see [12.197]). In the aqueous

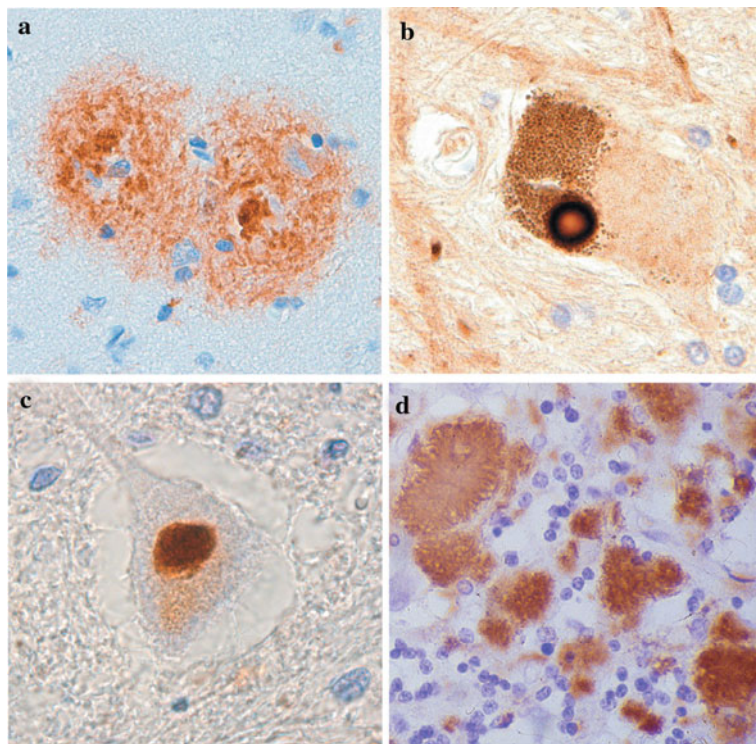


Fig. 12.61 Microscopy of protein aggregates in neurodegenerative diseases. (a) Senile plaques in neocortex of Alzheimer's disease. (b) Lewy body in substantia nigra of Parkinson disease. (c) Ubiquitinylated inclusion in spiral cord motor neuron in amyotrophic lateral sclerosis (ALS). (D) Protease-resistant prion protein (PrP) in cerebellum of Creutzfeldt–Jakob disease (CJD). (Reprinted with permission from [12.194]. © 2004 Nature Publishing Group)

environment between neurons, the A-beta peptides cling to one another, forming small soluble assemblies and long filaments ([12.197] and Fig. 12.61). Studies have shown that these assemblies and filaments can kill neurons cultured in Petri dishes and affect connections between neurons in mice (see [12.197]). It is not exactly understood how the A-beta assemblies and filaments kill neurons, but evidence suggests that aggregates of A-beta outside a neuron can initiate the alteration of the tau protein inside the cell and change the cellular activity of kinase enzymes that install phosphates into proteins. The affected kinases add too many phosphates to tau, which is connected to the intracellular microtubules, causing it to form twisted filaments. The altered tau proteins somehow kill the neuron, perhaps because they disrupt the microtubules that transport proteins and large molecules along axons and dendrites, and because the tau filaments and tangles clog the neuron's axons and dendrites. Thus, the formation of tau filaments is apparently a more general event leading to neuronal death, whereas A-beta is the specific initiator in Alzheimer's disease [12.197]. It is increasingly evident that aggregated disease proteins are not

simply neuropathological markers of neurodegenerative disorders but, instead, they almost certainly contribute to disease pathogenesis, thereby paving the way for the identification of rational therapeutic targets [12.194, 12.197]. But how amyloid contributes to the damage of Alzheimer's is not clear, and several anti-amyloid drugs have failed in phase III clinical trials [12.198].

The transition metals copper, iron, and zinc are implicated in the neurotoxicity of A-beta [12.195, 12.199]. A-beta Cu²⁺ catalyzes the generation of hydrogen peroxide (H₂O₂). The H₂O₂ permeates the cell membrane, and highly reactive hydroxyl radicals form, which disrupts the genetic material (DNA), and modify proteins and lipids. In addition, apoptosis is induced by the permeation of H₂O₂ throughout the cell membrane [12.200]. Zinc is redox-inert, and hence, inhibits the production of H₂O₂. Therefore, zinc's role in A-beta physiology is that of an antioxidant, but it is not concentrated enough in the brain to completely eliminate A-beta neurotoxicity (see [12.195]).

The strategies for fighting Alzheimer disease include to dissolve or clear toxic aggregates of A-beta from the brain, to block the activity of beta-secretase, to reduce the cutting of APP by gamma-secretase, or to block the kinases that place an excessive amount of phosphates onto the tau protein (see [12.197]). However, the diagnostic and therapeutic strategies to probe the central nervous system (CNS) are limited by the restrictive tight junctions at the endothelial cells of the blood-brain barrier (BBB; see Sect. 12.5). The cerebral endothelial cells (ECs) are distinguished from the ECs of the periphery (Fig. 12.62a). For instance, the brain ECs have fewer endocytotic vessels than peripheral ECs, which limits the transcellular flux at the BBB. The occluded tight junctions, with a high electrical resistance, join ECs of the brain. Furthermore, cerebral ECs have more mitochondria than peripheral ECs, which drives the increased metabolic workload necessary to maintain ionic gradients across the BBB (see [12.195]).

To overcome the impositions of the BBB, nanoparticulate drug carrier technology is being developed. Polymeric nanoparticles are promising candidates in the diagnosis and therapy of AD because they are capable of opening tight junctions [12.201] crossing the BBB [12.202], because of their high drug-loading capacities, and because of their targeting toward the mutagenic proteins of Alzheimer's [12.203]. A successfully used nanoparticle (NP) for the *in vivo* administration of drugs targeted to the brain is the rapidly biodegradable polybutylcyanoacrylate (PBCA; see Fig. 12.62b), where one of the suggestions how PBCA-NP (20 nm) pass through the BBB is the phagocytosis or endocytosis by the endothelial cells (see [12.195]). Novel PBCA-NP have been fabricated with clioquinol (5-chloro-7-iodo-8-hydroxyquinoline, CQ; Fig. 12.62c) encapsulated within the polymeric matrix. CQ is known to solubilize the A-beta plaques *in vitro* and inhibits the A-beta accumulation *in vivo* [12.204]. The PBCA-CQ-NPs freely cross the BBB and upon *in vivo* intravenous administration in mice, the PBCA-CQ-NP have a greater brain uptake than the free drug alone, so that this delivery system can be used as a prototype in the treatment of AD [12.195]. The recent discoveries may indicate that the quest for ways to prevent and treat Alzheimer's will not be in vain [12.197].

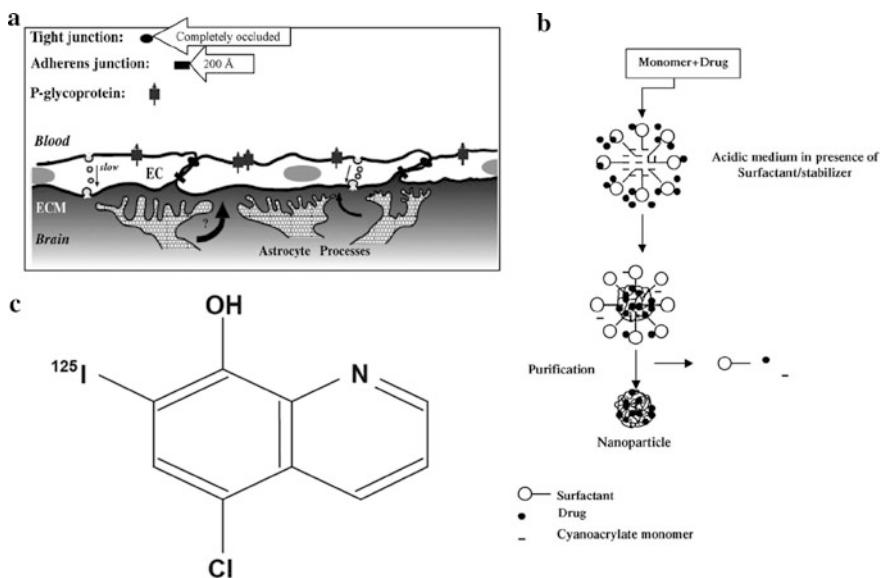


Fig. 12.62 (a) Features of the brain–blood barrier (BBB). The endothelial cells (EC) of BBB are coupled by tight junctions (TJ), that are completely occluded, and by adherens junctions (20 nm). The increased electrical resistance at the TJ strains paracellular movement of substances into the brain. Astrocytic processes (glial cells) in the extracellular matrix (ECM) envelop the capillaries and influence transport across the EC. Astrocytes do not participate in BBB because of the 20 nm gap between adjacent astrocytes. P-Glycoproteins (P-gp) on apical EC membranes let substances from the brain flow out into the bloodstream [12.195, 12.205]. (b) Emulsion polymerization of alkylcyanoacrylates [12.206]. (c) Structure of ^{125}I -clioquinol (CQ). The drug is radioiodinated for biodistribution studies [12.195]. (Reprinted with permission from [12.195]. © 2005 Elsevier)

Another strategy for Alzheimer therapy is to dissolve A-beta protein aggregates remotely in molecular surgery through the local heat delivered by metallic nanoparticles (NP) under gigahertz irradiation [12.207]. The 10 nm Au-NP, which are small enough to penetrate cell membranes, were linked to the peptide H-Cys-Leu-Pro-Phe-Phe-Asp/NH₂ (Cys-PEP). The sequence PEP selectively attaches to the A-beta aggregates, where it is believed that the peptides recognize a particular (hydrophobic) domain of the β -sheet structure of A-beta (i.e., amino acids 17–20 of the hydrophobic core of A-beta [12.208]). The Au-NP–Cys-PEP conjugates were incubated with A-beta solution where fibrils spontaneously start growing and form precipitates. In a 12 GHz weak microwave field (0.1 W), the Au-NP – Cys-PEP conjugates attached to the fibrils, absorbed the radiation and dissipated energy, causing disaggregation of the amyloid aggregates (Fig. 12.63). This effect is opposite to microscopic heating, where an increase in temperature results in an increased aggregation rate. Thus, attaching metallic Au-NP to a target and applying microwave fields allows a selective supply of energy to the system to remotely and non-invasively dissolve aggregates and deposits without post-irradiation reprecipitation,

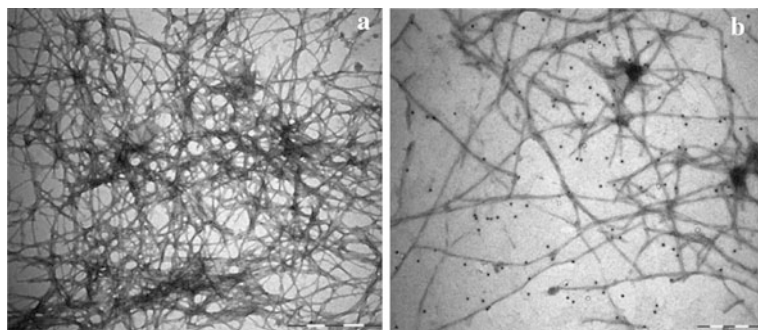


Fig. 12.63 (a) Electron microscopy of control A-beta alone incubated for 48 h and irradiated for 8 h (scale bar, 500 nm). (b) Au-NP-Cys-PEP + A-beta incubated for 48 h after 10 min of irradiation. Chopped fibrils and detached Au-NP can be seen (scale bar, 200 nm). (Reprinted with permission from [12.207]. © 2006 American Chemical Society)

which indicates that the *in vitro* amyloidogenic potential has been significantly decreased.

In the pursuit of diagnostic tools of AD, the analysis of cerebrospinal fluid (CSF) for potential biomarkers is of particular interest [12.209]. Several ELISA-based studies have shown that total tau protein and phosphorylated-tau protein (P-tau) levels are increased in Alzheimer's whereas the levels of A-beta with 42-amino acids (A-beta 42) are decreased in the CSF of patients at early stages of AD, compared to healthy controls (see [12.209]). However, these changes are not unique to AD and present tests diagnose only ~80% of AD correctly.

Nanoparticle-based assays can detect target protein levels many orders of magnitude lower than concentrations detected by ELISA (see Fig. 12.24 and Sect. 12.2). For a sensitive diagnosis of Alzheimer's disease the barcode assay for the detection of amyloid-derived ligands (ADDL), a marker oligomer linked to AD has been developed [12.79]. Furthermore, localized surface plasmon resonance (LSPR) on Ag nanoparticles has been utilized to monitor the interaction of ADDLs and specific anti-ADDL antibodies for the possible diagnosis of AD [12.210]. In the efforts to use NPs to detect, prevent, and treat protein misfolding diseases such as Alzheimer's [12.207, 12.211], it should be taken into account that uncoated NPs can promote fibrillation [12.212]. Indeed, designing coatings that limit or prevent protein adherence may prove to be of critical importance to safe application of NPs in medicine [12.213].

New treatment strategies for Alzheimer's could arise from the discovery [12.214] of interactions between beta-amyloid (A-beta), the toxic misfolded protein behind Alzheimer's, and prion protein (PrP), which itself forms aggregates in prion diseases like Creutzfeldt–Jakob disease (CJD). In this study [12.214], PrP has been identified as the surface protein needed for A-beta to disrupt functions of neurons. Screening for small molecules to block the interaction between A-beta and PrP could be straight forward for Alzheimer's therapy.

12.7.5 Ophthalmology

Human cataract lens cell membrane investigated at sub-nanometer resolution. Since human pathologies often originate from molecular disorder, imaging technologies with sub-nanometer resolution are required for the understanding of these pathologies. Malfunction of proteins in the eye lens gives rise to cataract, a disease leading to opacity of the lens, causing impairment of vision or blindness.

The lens of the eye has developed remarkable adaptions to ensure its transparency and to change its shape for focusing on different distances (accommodation). The lens is avascular, which minimizes light scattering. The cells are tightly packed with intercellular distances smaller than the wavelength of visible light. An internal microcirculation model that maintains a flow of water, ions, and metabolites can explain why cells located deep inside the lens are nourished (see [12.215]). In this microcirculation system, solutes flow in the extracellular space and flow through cell-to-cell channels back to the lens periphery. Two types of membrane proteins, aquaporin-0 (AQP0) and connexins (Cx), form the cell-to-cell junctions assuring metabolite transport, waste evacuation, water homeostasis, and intercellular adhesion. Six connexins form a connexon or half-channel and docking of two connexons from adjacent cells creates a cell-to-cell gap junction channel [12.216].

After cataract surgery from the eye of a 82-year-old male human, high-resolution atomic force microscopy (AFM) images (Fig. 12.64a, b) revealed only AQP0 in the AQP0 array borders, which is in contrast to healthy lens cell membranes where the arrays were edged by densely packed regions of connexons. In agreement with the AFM data, no molecules of the weight of connexon molecules could be detected by matrix-assisted laser desorption/ionization time-of-flight (MALDI-TOP) mass spectrometry [12.215]. Since the patient did not suffer from visual problems earlier, he must have disposed of connexons that were degraded with time and cataract formation has occurred by a progressive breakdown of the internal microcirculation system. Proteolytic degradation is considered as the most likely explanation for the absence of the connexons.

Based on these results, a model is suggested [12.215] for the molecular membrane protein organization in microdomains, in healthy and pathological cases (Fig. 12.64c–f). In the healthy lens membrane, connexons surround AQP0 arrays, control the size of the arrays, and assure together with the AQP0 arrays cell adhesion and the flow of water, ions, and metabolites. In the pathological case, when connexons are lacking, no metabolite or ion flow occurs, and an increased area of non-adhering membrane may result in lens opacification (Fig. 12.64d, f). The patient's cataract lens cells suffer from malnutrition, accumulation of waste products, diminished water flow, and inhomogeneously distributed cell adhesion over the cell surface. It is assumed that in the absence of connexons the internal microcirculation system of the lens collapses, resulting in the formation of cataract. The study shows the power of the AFM as a nanomedical imaging tool.

Cerium oxide nanoparticles to prevent retinal disorders. Retinal diseases that lead to partial or complete loss of vision cause misery for hundreds of millions of people throughout the world. Although the causes of these disorders are complex,

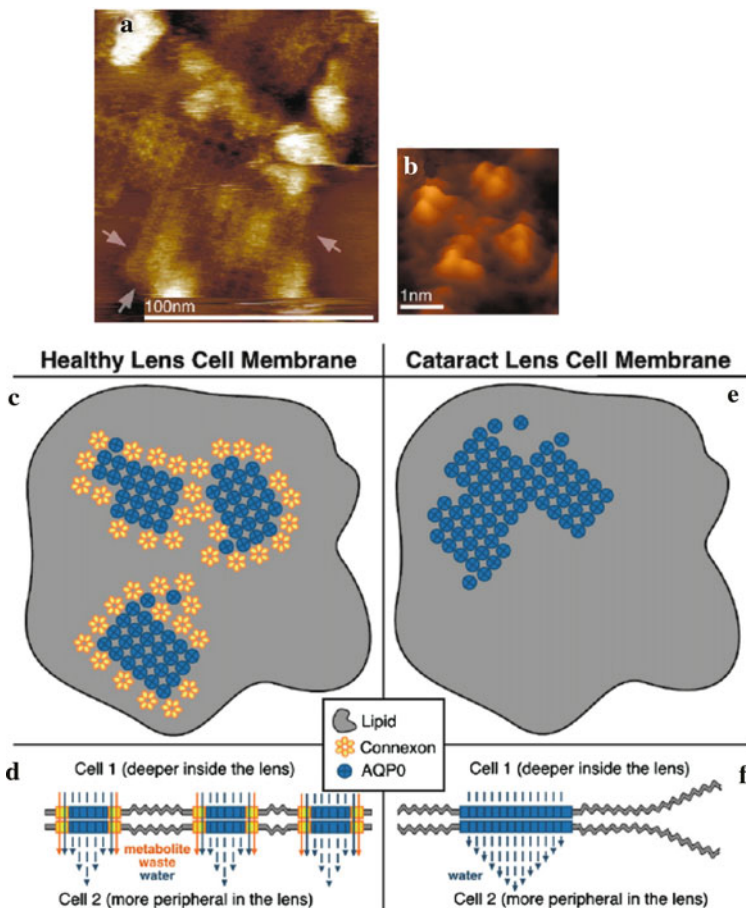


Fig. 12.64 High-resolution AFM images of aquaporin-0 (AQP0) junction arrays in the cataract lens cell membranes. (a) Medium-resolution topograph of AQP0 arrays. No connexons were found at the AQP0 microdomain edges (arrows). (b) Individual AQP0 in junctional conformation within the microdomain. (c) Top view at a healthy assembly with AQP0 square arrays edged by connexons [12.217]. (d) Top view of a pathological assembly in a senile cataract without connexons and larger AQP0 arrays. (e) Side view of a healthy assembly with water and metabolite transport and efficient cell adhesion where the non-adhering membrane areas are small. (f) Side view of a pathological assembly of a senile cataract. Fusion of AQP0 into large arrays favors the formation of large non-adhering membrane areas. According to the microcirculation model, the cell-to-cell flow of metabolites, waste (orange arrows), and water (blue arrows) is directional from the lens interior to the periphery [12.215]. (Reprinted with permission from [12.217] (a-c) and [12.215] (d-f). © 2007 Nature Publishing Group (a-c) and © 2007 Elsevier (d-f))

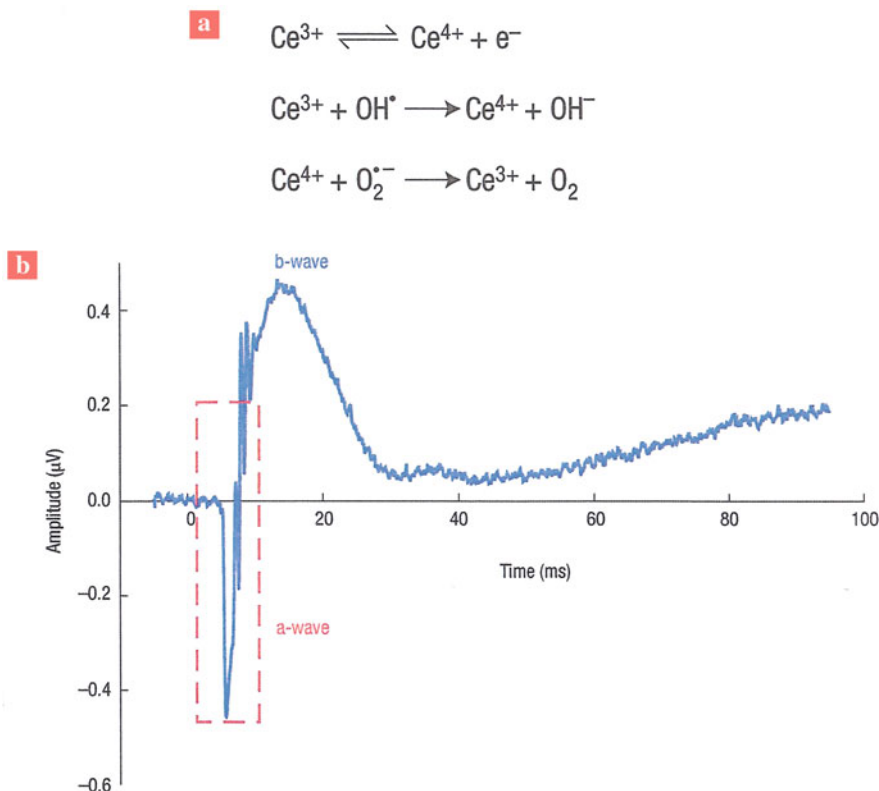


Fig. 12.65 (a) By switching between +3 and +4 valence states (top), nanoceria particles can reversibly scavenge free electrons from the reactive oxygen species (OH^\cdot and O_2^\cdot) to produce less harmful molecules (OH^- and O_2). This makes them attractive for treating diseases caused by reactive oxygen species. The \cdot symbol represents an unpaired electron which makes the molecule highly reactive. (b) A typical mammalian electrography wave forms in response to a flash of white light at $t = 0$. The “a-wave” (red box) indicates the initial part of the photoreceptor response, whereas the “b-wave” includes information about the response of the photoreceptor and other neural cells in the retina to light. (Reprinted with permission from [12.219]. © 2006 Nature Publishing Group)

oxygen radicals that damage the sensitive cells in the retina are thought to play a central role [12.218, 12.219]. Cerium oxide nanoparticles (nanoceria) can protect the retina from the “oxidative stress” caused by reactive oxygen species (Fig. 12.65). The rods and cones in our retina (Fig. 12.66) are specialized neurons that convert incoming light into a neurochemical signal. They are subjected to particularly high levels of oxidative stress, because, first, they are exposed to higher partial pressure of oxygen and possess a higher metabolic rate than other cell types. The high metabolic demands are met by the production of significant amounts of adenosine triphosphate (ATP) by the mitochondria in the cell which involves the reduction of oxygen to water, generating a small fraction of electrons which can form toxic

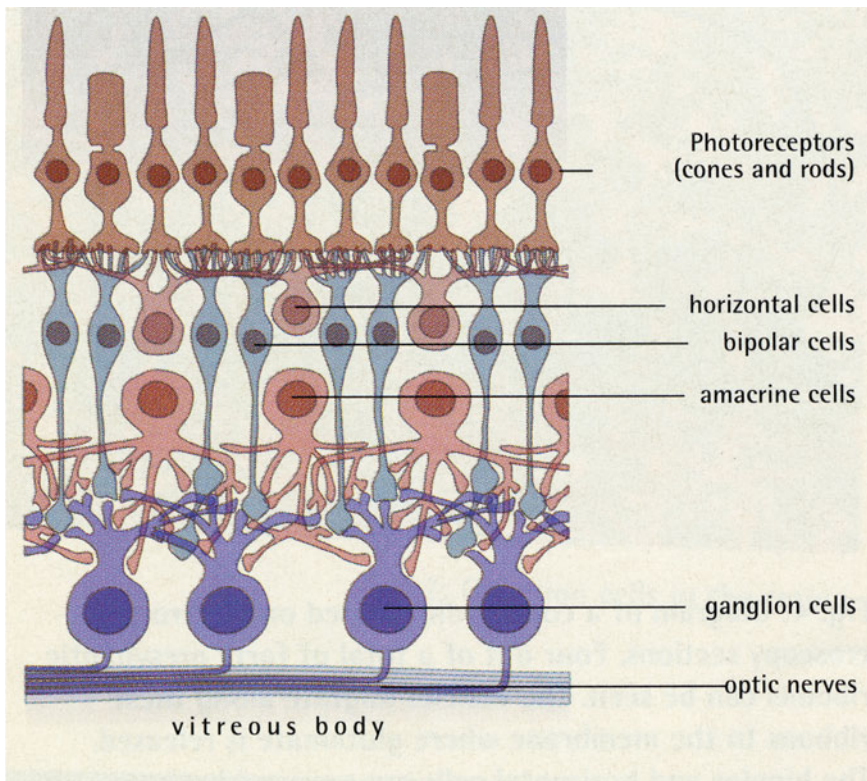


Fig. 12.66 Nerve cells and their connections with the retina. At the top there are the photoreceptors of which there are four types – rods for seeing in the dark and three types of cones with different color sensitivities. The receptors have a contact point (synapse) at their lower end with each of the two subsequent nerve cells, the bipolar and horizontal cells. The *lower part* shows complex contact points between bipolar, amacrine, and ganglion cells. Each ganglion cell sends a process to the brain in the optic nerve. (Reprinted with permission from [12.220]. © 2001 Max-Planck Society)

reactive molecules, known as superoxides, in the cell. Second, photons of visible light can produce highly reactive “singlet” oxygen species, and overproduction of the reactive species can overwhelm the natural defences to finally kill cells. Cerium, which can exist in both a +3 and a +4 state, can scavenge the free electrons from reactive oxygen species making them non-reactive (Fig. 12.65a).

Reducing the diameter of nanoceria to about 5 nm results in more oxygen vacancies (see [12.219]) which makes it even a better scavenger. When retinal cells are treated *in vitro* with hydrogen peroxide – a source of reactive oxygen molecules – and incubated with nanoceria, the nanoparticles protect the cells by preventing them from reactive molecules [12.218]. For *in vivo* studies nanoceria was injected into the eye vitreous body of albino rats which have retinas highly susceptible to photodamage. The retinas pretreated with nanoceria experienced

significantly less light-induced damage and cell death, compared with controls [12.218]. For studying the recovery from light-induced damage, the non-invasive test known as electroretinography exhibiting an “a-wave” and a “b-wave” was employed (Fig. 12.65b). The eyes pretreated with nanoceria showed ~80% of the a-wave and the b-wave amplitudes after light exposure compared to controls without light exposure, which is much higher than the ~23% after light exposure without nanoceria. Although it is unclear how the nanoceria protects the retina, it is speculated that the nanoparticles enter the photoreceptors because reactive oxygen species are naturally formed within these cells when exposed to light and only exist over a very short distance.

It has been demonstrated that a hybrid bionanodevice can be fabricated that links nerve cells and photovoltaic nanoparticle films where the properties of nanoparticles can be applied to light-stimulated nerve signaling devices, including the possibility of synthesizing a nanoparticle-based artificial retina [12.221].

Glaucoma drug conjugated to ceria nanoparticles. Many individuals suffer from the ocular disease glaucoma (see [12.222]). This condition describes a destruction of optic nerve cells and deterioration of eye sight as a result of increased intraocular pressure. The pressure is partially caused by the formation of carbon dioxide produced by the enzyme human carbonic anhydrase II (hCA II; Fig. 12.67a), a Zn^{2+} – containing metalloenzyme that catalyzes the reversible hydration of carbon dioxide to bicarbonate. Sulfonamide compounds, such as 4-carboxybenzene sulfonamide (CBS; Fig. 12.67b), have been shown to selectively inhibit hCA II which involves coordination of the sulfonamide group (as the anion) to the Zn atom in the active site of hCA II to form a complex. Since the ocular bioavailability of many drugs is significantly enhanced by binding to nanoparticles, the CBS drug has been

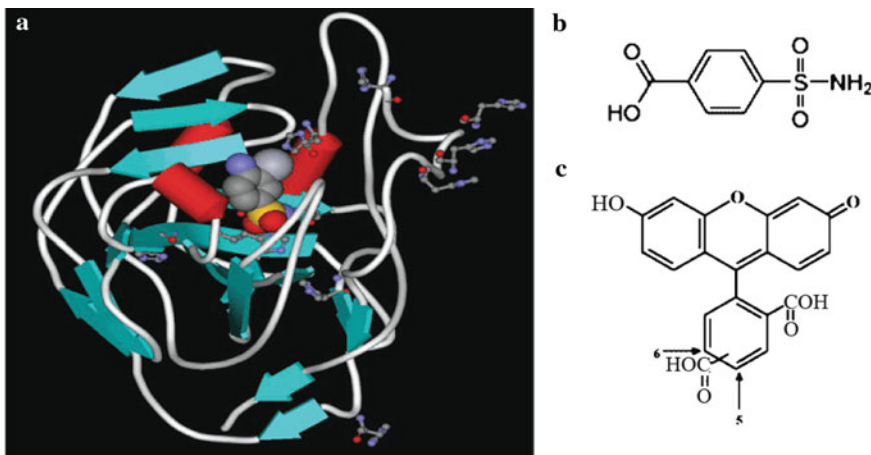


Fig. 12.67 (a) Cartoon diagram showing the structure of human carbonic anhydrase. (b) Molecular structure of carboxybenzene sulfonamide and (c) of carboxyfluorescein. (Reprinted with permission from [12.222]. © 2007 American Chemical Society)

conjugated to ~15 nm nanoceria using epichlorohydrin as an intermediate linkage, and carboxy fluorescein (Fig. 12.67c) as a conjugate for fluorescence imaging. The efficiency of the functionalized nanoparticles was tested by observing the effect of the nanoparticles on the rate of hCA II-catalyzed hydrolysis of 4-nitrophenyl acetate to form 4-nitrophenolate. The change in the spectroscopic data [12.222] with the concentration of functionalized nanoceria indicated the inhibiting effect. More studies will likely evolve into an inhibition of hCA II in living cells and an effective treatment of glaucoma.

12.7.6 Viral and Bacterial Diseases

HIV inhibitor saquinavir delivered into cells by nanoparticles. The human immunodeficiency virus (HIV) is a retrovirus which causes the widespread disease acquired immune deficiency syndrome (AIDS), a severe immunological disorder. The Nobel Prize in medicine 2008 has been awarded to F. Barre-Sinoussi and L. Montagnier for the discovery of the HIV virus. It is known that the HIV infects peripheral mononuclear phagocytic cells and the central nervous system in the early stages [12.223]. The phagocytic monocyte/macrophage cells (Mo/Mac) also act as shuttle for the viruses to go to other sites in the body and thrive there (see [12.224]). Saquinavir, the first HIV protease inhibitor to be marketed as Invirase® for the treatment of HIV, is a peptide derivative that inhibits HIV-1 and HIV-2 protease-mediated cleavage of the gag and pol polyproteins of the HIV genome, thus preventing the posttranslational processing required for virus maturation and spread [12.225]. However, the therapeutic use of anti-HIV protease inhibitors suffers from poor solubility and the oral bioavailability of a single dose of saquinavir is only 4% [12.225]. It has been shown [12.226] that at a concentration of 100 nM, free saquinavir was completely inactive in chronically HIV-infected Mo/Mac cells, but when bound to poly(hexylcyanoacrylate) nanoparticles, caused a 35% decrease in virus production.

It was hypothesized that the THP-1 human monocyte/macrophage (Mo/Mac) cell line derived from the blood of a 1-year-old boy with acute monocytic leukemia (see [12.224]) would endocytose a nanoparticulate formulation and provide optimal concentration of saquinavir in Mo/Mac cells as well as transport the drug to the central nervous system and other sites, which are potential reservoirs for HIV. The drug would be released at these sites and help in targeted and effective eradication of the viral load. Preliminary studies showed [12.224] that a poly(ethylene oxide)-modified poly(epsilon-caprolactone) (PEO-PCL) nanoparticulate system (Fig. 12.68a) with a particle size of 200 nm is an efficient delivery vehicle for the release of the saquinavir anti-HIV protease inhibitor and its intracellular delivery to the Mo/Mac cells (Fig. 12.68c). For optical detection of the PEO-PCL cell penetration, the hydrophobic fluorescent dye rhodamine 123 was encapsulated in the PEO-PCL nanoparticles (Fig. 12.68 c). Surface modification of PCL nanoparticles with PEO chains prevents aggregation and allows for efficient systemic delivery especially after intravenous administration [12.224]. For the

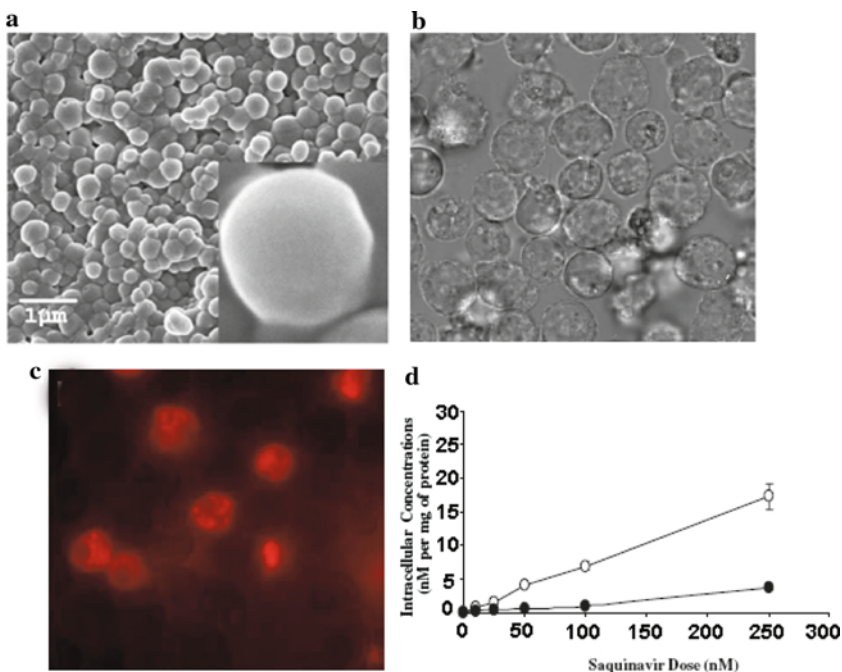


Fig. 12.68 Nanoparticles of PEO-PCL (poly(ethylene oxide))-modified poly(epsilon-caprolactone) for AIDS (acquired immunodeficiency syndrome) treatment. The PEO-PCL nanoparticles can be loaded with saquinavir, a HIV (human immunodeficiency virus) inhibitor for intracellular delivery of saquinavir to THP-1 human monocyte/macrophage (Mo/Mac) cells for AIDS treatment. **(a)** Scanning electron micrograph of PEO-PCL nanoparticles with the inset showing a nanoparticle at higher resolution. **(b)** Uptake of rhodamine 123 containing PEO-PCL nanoparticles by the THP-1 monocyte/macrophage cells incubated for 1 h at 37°C with bright-field **(b)** and corresponding fluorescent images **(c)**. **(d)** Intracellular concentration of tritiated [^3H]-saquinavir as a function of dose administered to THP-1 monocyte/macrophage cells. The concentrations for [^3H]-saquinavir administered in PEO-PCL nanoparticles (○) are much higher than when administered in aqueous solution (●). (Reprinted with permission from [12.224]. © 2006 Springer Verlag)

determination of the drug concentration inside the cells, nanoparticles loaded with tritiated [^3H]-saquinavir were prepared [12.224], showing substantially increased drug uptake in the cells by nanoparticle formulations compared to aqueous drug solutions (Fig. 12.68d). It had been shown earlier that PEO-PCL nanoparticles can efficiently encapsulate hydrophobic drugs, such as tamoxifen and paclitaxel, and deliver them in tumor cells and *in vivo*, and that the by-products of PCL degradation are not acidic and do not cause any toxicity *in vivo* [12.227]. Further studies [12.224] show that efficient nanoparticle formulations can be developed for saquinavir to ensure better encapsulation and release of the drug. A significant

uptake of drug-loaded nanoparticles was also observed in the THP-1 cells of the monocyte/macrophage origin (Fig. 12.68d), which are known to shuttle the infected virions.

It has been demonstrated that 2 nm gold nanoparticles transform a weakly binding and biologically inactive small molecule into a multivalent conjugate that effectively inhibits HIV-1 fusion to human T cells [12.228], a principle type of white blood cell that has various roles in the immune system.

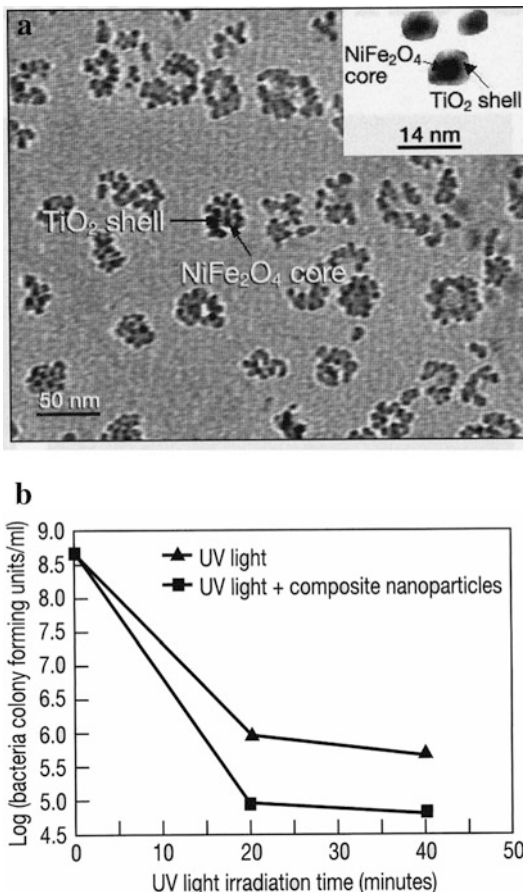
Viruses infect specific cells within host organisms, replicate, destroy the cells, and spread from cell to cell in infection cycles, thus causing disease (see [12.229]). These viral properties have inspired synthetic designs of various drug delivery vehicles. A synthetic nanosized polymer vehicle can mimic viral properties significantly. This virus-mimetic nanogel, loaded, e.g., with the model anticancer drug, doxorubicin, may prove valuable for treating diseases, such as tumors, with greater efficacy [12.229].

Antibacterial nanocomposites. Titanium dioxide (TiO_2) is an effective photocatalytic antimicrobial material when it is applied on an infected area of the human body or a contaminated area of the physical environment. However, it is difficult to remove from the treated surface. A removable, antimicrobial magnetic nanocomposite has been developed [12.230], consisting of a photocatalytic shell of anatase TiO_2 and a superparamagnetic core of nickel ferrite (NiFe_2O_4 ; Fig. 12.69a).

When TiO_2 nanoparticles in aqueous suspension are irradiated with UV light, free hydroxyl radicals (OH^-) are generated that are highly toxic to microorganisms. This concept has been explored to investigate the inactivation of *Escherichia coli* bacteria with radiation dose in a culture medium in the presence of UV-irradiated TiO_2 -coated NiFe_2O_4 nanoparticles (Fig. 12.69b). In the presence of the TiO_2 -coated nanoparticles the concentration of *E. coli* bacteria is much faster reduced than with UV light alone. The TiO_2 photocatalytic shell provides the antimicrobial capability to inactivate bacteria and remove organic pollutants, while the NiFe_2O_4 magnetic core enables controlled delivery of the nanoparticles through a small magnetic field. This supports their application as removable antimicrobial photocatalyst nanoparticles.

Nano silver-titanium dioxide for enhanced hygiene. Mass Transit Railway (MTR), the corporation that runs Hong Kong subway, considered to invest on nanotechnology to enhance hygiene levels in MTR stations and trains. Nano silver-titanium dioxide coating (NSTDC, a non-toxic disinfectant) will be applied to surfaces that passengers commonly touch, including escalator handrails, the buttons on ticket issuing machines, as well as buttons and handrails in lifts, grab poles, and strap hangers in trains. Developed in Japan, NSTDC is certified to be effective in killing a wide range of bacteria and viruses, including the H1N1 influenza virus A. It is used in hospitals, offices, and homes in Japan. NSTDC's main component, TiO_2 , has been approved for use in food by the United States Food and Drug Administration and under the Public Health and Municipal Service Ordinance in Hong Kong [12.231].

Fig. 12.69 (a) Transmission electron micrograph of TiO_2 -coated NiFe_2O_4 nanoparticles, with a closer view in the *inset*. (b) *E. coli* bacterial inactivation response to TiO_2 -coated NiFe_2O_4 nanoparticles as a function of UV irradiation time. The units of the *y*-axis represent the number of colonies of bacteria in 1 ml of solution. (Reprinted with permission from [12.230]. © 2006 Materials Research Society)



Single-walled carbon nanotubes (SWNTs) can kill bacteria like the common pathogen *E. coli* by severely damaging their cell walls [12.232]. It is projected that SWNTs could be used to create antimicrobial materials and surface coatings to improve hygiene, while their toxicity could be managed by embedding them to prevent their leaching into the environment.

12.8 Nanobiomaterials for Artificial Tissues

Nanotechnology can contribute to the development of biomaterials in medical fields including orthopedics, dentistry, cartilage treatment, vasculature, bladder therapy, central and peripheral nervous system therapy etc. [12.233]. In addition, first efforts to construct synthetic chromosomes have been undertaken [12.234]. The ultimate goal in tissue engineering [12.235] is to be able to draw stem cells to a scaffold in

vivo for controlled differentiation to the desired cell type to restore the functions of the diseased tissue [12.236].

12.8.1 Enhancement of Osteoblast Function by Carbon Nanotubes on Titanium Implants

The market for orthopedic implants is growing at a rapid rate due to the aging of our population. Each year, more than 600,000 joint replacements are performed in the United States alone with an estimated worldwide cost in excess of 3 billion dollars [12.237]. Orthopedic implants require the function of osteoblasts (see Sect. 11.7) to create new bone on their surface. Osteoblasts form the nanostructured organic matrix of the bone and produce proteins which play critical roles in the mineralization process. Critical in the design of successful implants is, therefore, the ability of implant materials to control protein adsorption and osteoblast adhesion after implantation. The degree to which proteins adsorb on implant surfaces depends on the chemistry, charge, wettability, and topography of the biomaterial (see [12.238]).

It has been shown [12.238] that osteoblasts closely interact with carbon nanotubes (CNT; Fig. 12.70c) which are grown on anodized Ti surfaces covered with

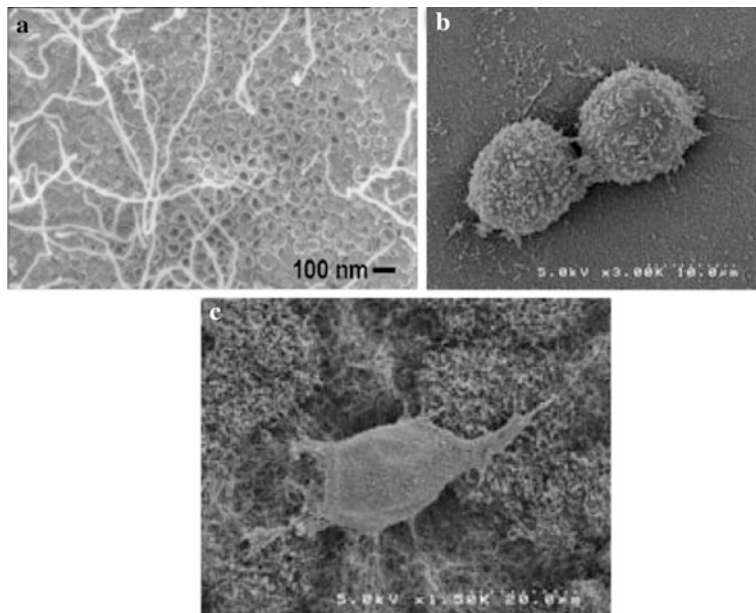


Fig. 12.70 (a) SEM micrograph of carbon nanotubes grown from the nanoholes of an anodized Ti surface with a Co catalyst. (b) Osteoblast adhesion after 4 h on anodized Ti (scale bar: 10 μ m) and (c) on multiwalled carbon nanotubes grown out of a nanohole Ti surface (scale bar: 20 μ m). (Reprinted with permission from [12.238]. © 2007 Institute of Physics)

50 nm holes (Fig. 12.70a) whereas less interaction of osteoblasts is observed with only anodized Ti surfaces (Fig. 12.70b). In addition, calcium deposition was found to be significantly higher when osteoblasts were cultured on CNTs grown from anodized Ti surfaces [12.238]. Surface-enhanced Raman scattering studies, furthermore, observed increased unfolding of vitronectin (a protein which mediates osteoblast function) and, thus, exposure of cell adhesive epitopes on nanoparticulate versus microparticulate materials [12.239, 12.237].

Composites of multiwalled carbon nanotubes (MWNTs) and hydroxyapatite on Ti 6Al4V medical alloys yield porous surfaces which are ideal for natural bone in-growth. Furthermore, cracks are effectively deflected by the MWNTs which contributes to an improvement of fracture toughness [12.240].

12.8.2 Nanostructured Bioceramics for Bone Restoration

Hydroxyapatite (HA), a calcium phosphate, is the ceramic constituent of bone, and the initial reason for its use as an implant material is that it forms direct bonds with living bone (see [12.241]). The adhesion and proliferation of osteoblast cells for bone growth are significantly higher on nanoporous HA than on conventional HA [12.242] and are further increased on surfaces that contain CaTiO_3 [12.243].

Transplantation of osteogenic cells in a suitable matrix is another strategy for engineering bone tissue. 3D distribution and proliferation of cells within a porous scaffold are of clinical significance for the repair of large bony defects. In a 3D nanoporous HA scaffold, bone marrow stromal cells of rats were seeded in vitro. The cells adhered, proliferated, and differentiated well [12.244]. Likewise, bone scaffold material made of a nano-HA/collagen/polylactic acid (PLA) composite has been developed by biomimetic synthesis [12.245]. In an additional example, human osteoblast-like cells on a nanofluorapatite/collagen composite exhibited higher proliferation and differentiation rates than those on HA/collagen. These enhanced osteoblast cell responses were attributed to the fluorine release and the reduced dissolution rate [12.246]. Strong and bioactive composites have been developed by combining calcium phosphate ceramic (CPC) fillers with nanosized SiO_2 fused to whiskers in a resin matrix. The SiO_2 particles were fused to SiC whiskers to roughen the whisker surface for enhanced retention in the matrix. The mechanical properties of the non-cytotoxic CPC-whisker composites nearly matched those of cortical and trabecular bone [12.247]. Composites with needle-like HA crystals may be suitable for intraosseous implantation. These cements exhibit strengths matching those for cancellous bone and non-cytotoxicity qualifying for efficient bone repair surgery [12.248].

An optimum grain size of about 60 nm for osteoblast adhesion has been observed for Al_2O_3 [12.249], whereas the optimum particle size in the case of TiO_2 is about 45 nm. The following hydroxyapatite nanoparticles for treating bone defects are commercially available are Ostim® (Osartis GmbH, Germany); VITOSS® (Orthovita, Inc., USA); and NanOss™ (Angstrom Medica, USA) [12.250].

12.8.3 Fibrous Nanobiomaterials as Bone Tissue Engineering Scaffolds

Tissue engineering making use of nanoscale features to increase new bone synthesis is a potential alternative to current therapies. Nanofiber matrices have shown great promise as tissue engineering scaffolds for bone regeneration. The biomimetic environment of the nanofiber matrix (Fig. 12.71) affects cell–cell and cell–matrix interactions for favorable cell behavior. The advantages of a scaffold composed of ultrafine, continuous fibers are high porosity, variable pore size distribution, high surface-to-volume ratio, and importantly, morphological similarity to the natural extracellular matrix (ECM) [12.237]. In addition, both *in vitro* [12.251] and *in vivo*

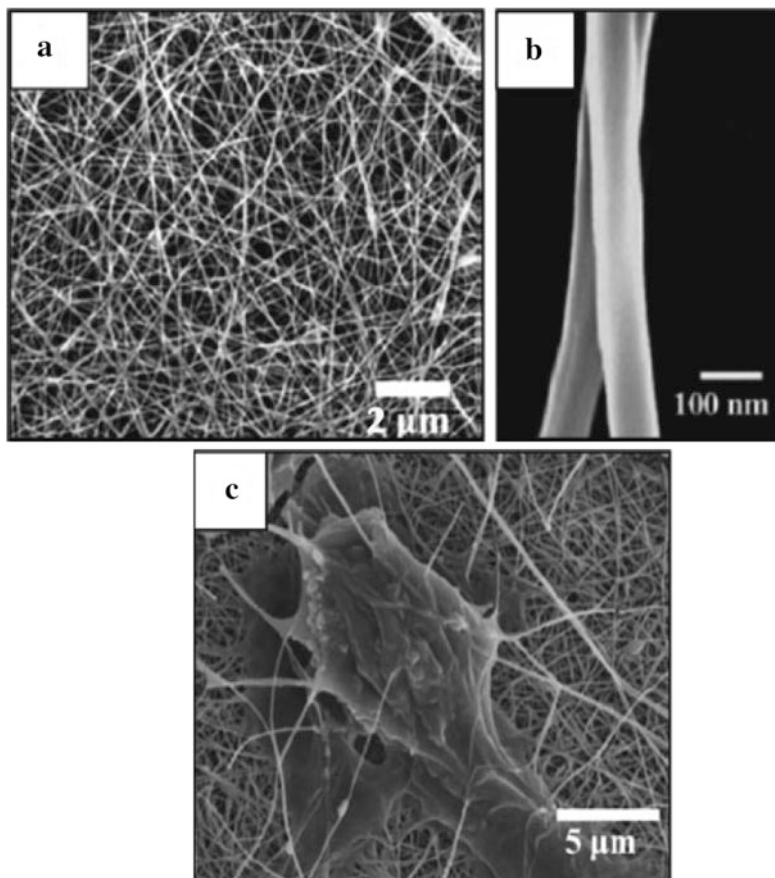


Fig. 12.71 Scanning electron micrographs of (a) electrospun nanofibrous mesh made of chitosan/polyethylene oxide. (b) high magnification of the nanofibers shown in (a); and (c) osteoblast-like cells (MG 63) seeded on a nanofibrous mesh after 5 days culture. (Reprinted with permission from [12.253]. © 2005 Elsevier)

[12.252] results have shown that mesenchymal stem cells undergo osteogenic differentiation with the support of nanofibrous scaffolds with cell and type I collagen formation, and mineralization [12.252]. Human bone marrow stromal cells were found to adhere and proliferate well on a polymeric nanofiber scaffold. In fact, the cells were found to crosslink the nanofibers in the matrix and integrate with the surrounding fibers to form a 3D cellular network. Adherent osteoblast-like cells in electrospun (see Sect. 3.3) chitosan-based nanofibers are shown in Fig. 12.71c. Polymer nanofiber degradation generates space within a scaffold that facilitates cellular processes, such as proliferation and the deposition of newly synthesized ECM. Furthermore, reports indicate the feasibility of developing composite nanofibers by encapsulating nanohydroxyapatite particles within polyphosphazene nanofibers to develop scaffolds having better osteoconductivity and osteointegration [12.254].

The strategies used in bone research have also been applied to other musculoskeletal tissues. Nanofiber scaffolds have also been implemented in ligament and tendon reconstruction research [12.255], as well as in cartilage tissue engineering where nanoparticle titania has been used in biomaterial composites [12.256].

12.8.4 Tissue Engineering of Skin

In tissue engineering of skin there is much interest in producing scaffolds by electrospinning nanofibers for replacing the natural collagen skin scaffolds. This versatile method can produce 3D open porous structures that approximate the structure of collagenous dermis (see Fig. 12.72).

12.8.5 Angiogenesis

The formation of blood vessels (neovascularization or angiogenesis) has been identified as a problem for tissue-engineered constructs [12.257]. Angiogenesis can be substantially stimulated by self-assembled nanostructures of peptide amphiphile molecules on heparin, a complex organic acid (see Fig. 12.73). By this procedure, relatively rigid nanofibers are generated that can be loaded with vascular endothelial growth factor (VEGF), which when implanted *in vivo* gives rise to the stimulation of vascularization.

12.8.6 Promoting Neuron Adhesion and Growth

The stimulation of neuron adhesion and neurite outgrowth is of importance for the regeneration of both the peripheral and the central nervous system after injury or disease. It has been demonstrated (see [12.259]) that topographical features are of relevance for guiding axon growth and pathfinding. The preference of axons to grow on ridge edges rather than in grooves (see Fig. 12.74a) suggests that

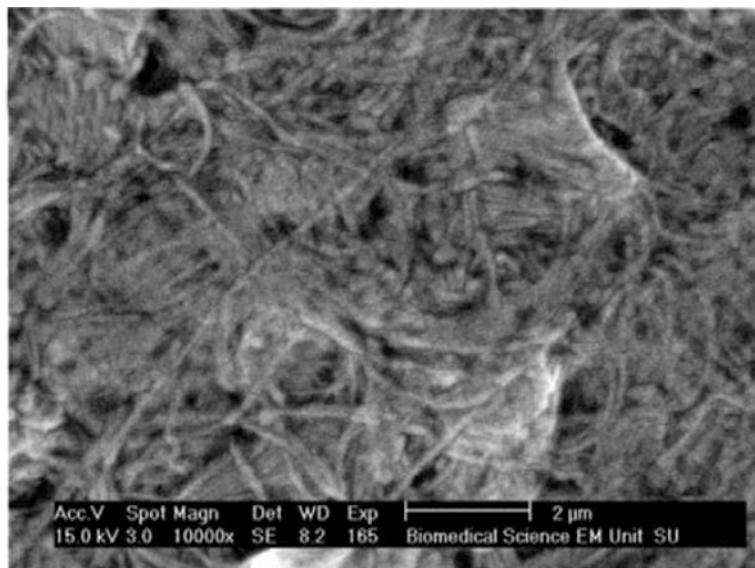


Fig. 12.72 A biodegradable electrospun scaffold. The scaffold fibers show good vascularization and penetration of granulation tissue. Scale bar: 2 μ m. (Reprinted with permission from [12.257]. © 2008 Elsevier)

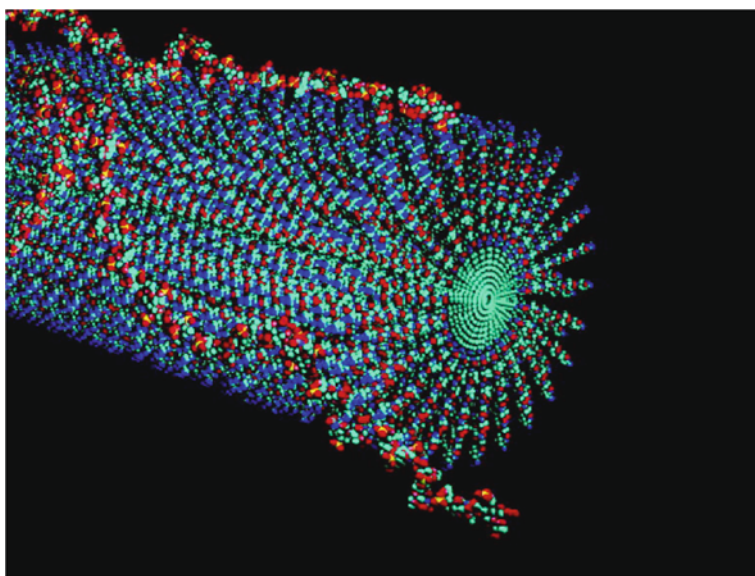
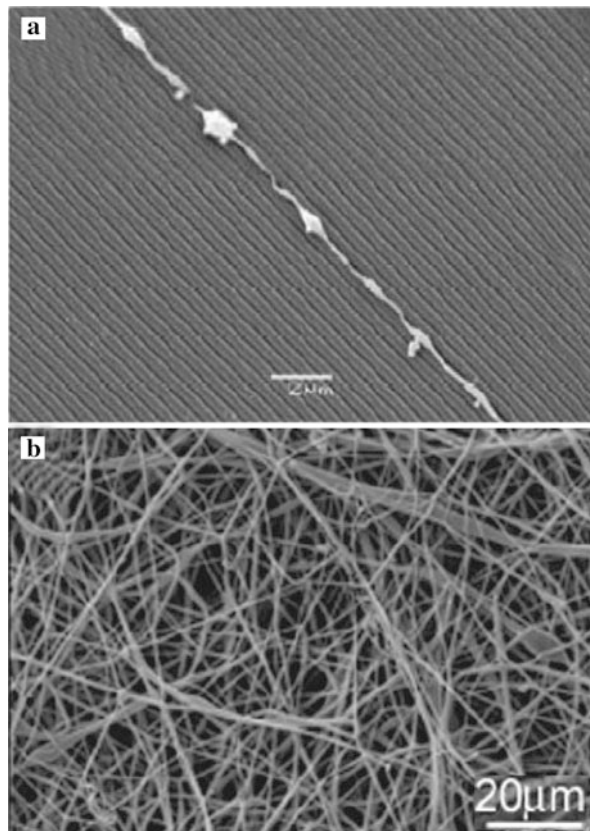


Fig. 12.73 Schematic of a heparin-nucleated nanofiber designed to promote the growth of blood vessels. The cylindrical nanostructure is formed by the aggregation of positively charged peptide amphiphile molecules, which have the capacity to bind to the negatively charged heparin chains and the poly-ion nucleates the fiber. (Reprinted with permission from [12.258]. © 2006 American Chemical Society)

Fig. 12.74 (a) Scanning electron micrographs show that axons prefer to grow along the ridge edges and not in the grooves when the dimensions of the imprinted patterns are 100 nm in width and 500 nm pitch [12.262] ; (b) Scanning electron micrograph of random poly(ϵ -caprolactone) nanofibers produced by electrospinning. (Reprinted with permission from [12.259]. © 2008 Elsevier)



nanofeatures can be incorporated into tissue engineering design strategies to provide contact guidance for nerve regeneration. Creating a scaffold that mimics the *in vivo* 3D protein architecture of the extracellular matrix (ECM) ranging from 50 to 500 nm (see [12.259]) is pivotal for tissue regeneration as cell–matrix interactions are a vital component to cell survival, differentiation, and proliferation. Electrospun poly(ϵ -caprolactone) nanofibers, which are biodegradable and non-toxic (see [12.260]), have been shown to direct neural stem/progenitor cell (NSPC) differentiation into primarily oligodendrocytes (cells in brain supporting tissue) [12.261].

Peptide amphiphile (PA) molecules that self-assemble *in vivo* into supramolecular nanofibers were shown to promote axon elongation in a mouse model of spinal cord injury (SCI) [12.263].

12.8.7 Spinal Cord *In Vitro* Surrogate

Spinal cord injuries (SCI) give rise to paralysis. Central to the repair of these injuries is the need to regrow axonal bundles across the zone of damage which consists of

damaged and disrupted axonal processes, reactive glial and inflammatory cells, and developing glial scar tissue. The development of strategies for the regrowth of axons through a section of damaged spinal cord could benefit from the availability of an *in vitro* model in which the potential clinical utility of candidate techniques could be assessed. For this purpose, a spinal cord surrogate has been fabricated [12.264] from a composite of agarose gel as the parenchymal component and 8 μm thick glass fibers aligned along the surrogate axis to simulate the axonal bundles. This “artificial spinal column” (Fig. 12.75a) reproduces with its pores (pore size 10–100 nm) the characteristics of porous flow in the central nervous system (CNS; extracellular space in the tissue about 20 nm) and the anisotropic anatomical features of the spinal cord [12.264]. These properties are demonstrated when bromphenol blue dye is injected into the artificial spinal column with a spreading preferentially along paths aligned with the fibers (Fig. 12.75b–d). This is a consequence of a porous annulus (with the thickness of the diameter of a gel pore) around each fiber. The porous zones are formed because the polysaccharide gel molecules favor the formation of cross-links at junction zones removed from the fiber surface [12.264]. This surrogate structure may enable the preclinical evaluation of infusion strategies foreseen for drug and cell delivery into living spinal cord tissues. It also may serve

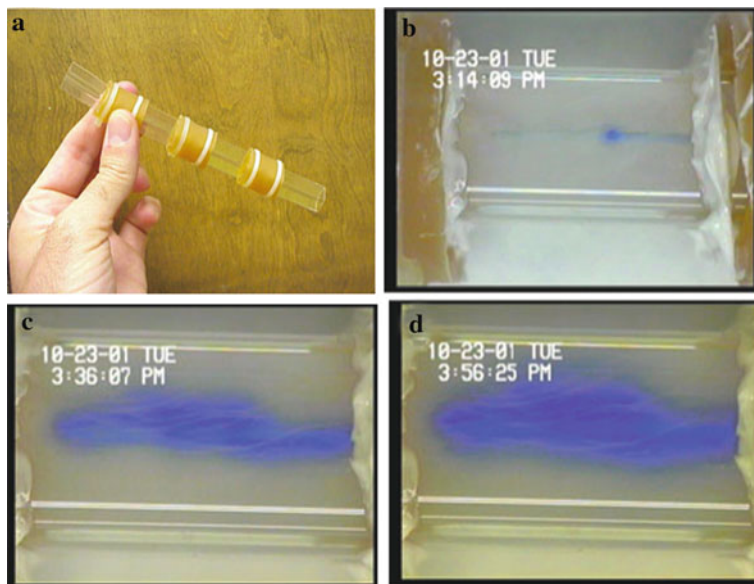


Fig. 12.75 (a) Mechanical structure of the “artificial spinal column” that serves as a glass container for the surrogate spinal cord. The hose junctions can allow for simulation of the effects of the intervertebral disks and facet joints. (b–d) Infusion of bromphenol blue dye into the spinal cord surrogate showing the volume of distribution at (b) 13 min, (c) 35 min, and (d) 55 min. The infusate is flowing preferentially along the fiber tracts within the gel. (Reprinted with permission from [12.264]. © 2002 Institute of Physics)

as a medium to study the regrowth of axons in order to model spinal cord tissue regeneration.

12.8.8 Efforts for Synthesizing Chromosomes

A synthetic chromosome has been constructed by a team of scientists assembled by Craig Venter and led by the Nobel laureate Hamilton Smith [12.234]. Using lab-made chemicals, the scientists have painstakingly stitched together a chromosome that is 381 genes long and contains 580,000 base pairs of genetic code. The DNA sequence is based on the bacterium *Mycoplasma genitalium* which the team pared down to the bare essentials needed to support life, removing a fifth of its genetic makeup. The wholly synthetically reconstructed chromosome was christened *Mycoplasma laboratorium*. It is then transplanted into a living bacterial cell and in the final stage of the process it is expected to take control of the cell and, in effect, become a new life form.

The new life form will depend on its ability to replicate itself and metabolize on the molecular machinery of the cell into which it has been injected, and in that sense it will not be a wholly synthetic life form. However, its DNA will be artificial, and it is the DNA that controls the cell and is credited with being the building block of life [12.234].

12.9 Nanosurgery – Present Efforts and Future Prospects

Incisions have become smaller, dissections have become more focused, and micro-surgery performed under an operating microscope is now the norm. However, even current “microsurgery” is “macro” when compared with the dimensions that are relevant at the nanoscale level. Currently, several technical advances are leading to the manipulation of cellular and subcellular structures at the micrometer and nanometer scales [12.265].

12.9.1 Femtosecond Laser Surgery

By tightly focusing a femtosecond laser pulse, collateral damage to surrounding structures is negligible because the interaction of the laser pulse with the biological material occurs on a much shorter timescale than the heat transfer into the material [12.266]. This reduces the likelihood that the cell itself will be injured. In fact, spatial resolution in the nanometer range can be attained [12.267]. Femtosecond laser pulse energies between 1.2 and 1.7 nJ produce cuts as narrow as 200 nm. Figure 12.76 demonstrates the ablation of a single mitochondrion via precision targeting of the femtosecond laser. Additional studies have demonstrated that ablation of subcellular organelles can be accomplished in a live cell without compromising

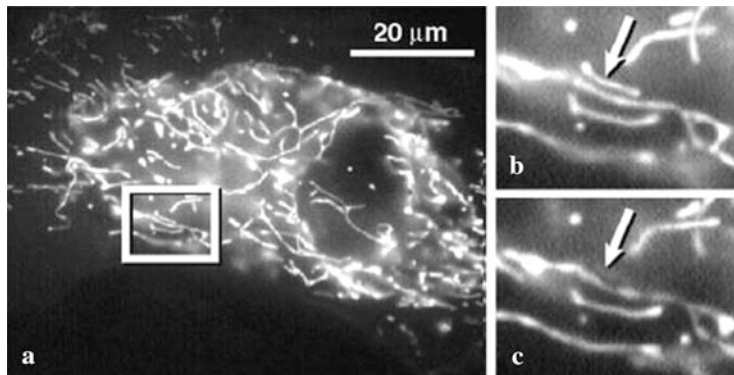


Fig. 12.76 Ablation of a single mitochondrion within a living cell. (a) Fluorescence image of multiple mitochondria. Target mitochondrion (arrow) before (b) and after (c) ablation with 2 nJ laser pulses, where the neighboring mitochondria are unaffected. (Reprinted with permission from [12.268]. © 2005 Tech Science Press)

cell viability [12.269]. These techniques have potential applications in intracellular surgery, including single chromosome dissection, non-invasive inactivation of specific genomic regions and individual chromosomes, and highly localized gene and molecular transfer. Femtosecond lasers have also been applied to gene therapy. A variety of mammalian cells could be directly transfected with DNA, without destroying the cellular structure by using femtosecond lasers to create a single, site-specific, localized perforation in the cell membrane through which DNA could enter (Fig. 12.77).

12.9.2 *Sentinel Lymph Node Surgery Making Use of Quantum Dots*

Sentinel lymph node mapping is a common procedure used to confirm the presence of cancer in a single “sentinel” lymph node (SNL) [12.265]. The current surgical procedures, using radioactive isotopes for lymph node mapping, are, however, inexact and result in more extensive lymph node dissection than is necessary. Near-infrared fluorescent quantum dots (10–20 nm) can be used to provide real-time image guidance for the dissection of SNL [12.271]. After injection of 400 pmol of quantum dots in a 35 kg pig the SNL position can be identified rapidly (see Chap. 11.2; Fig. 11.16).

12.9.3 *Progress Toward Nanoneurosurgery*

The study of neuronal regeneration is critical to the treatments for human neurological diseases. Surgical research has been directed at the neural circuit of

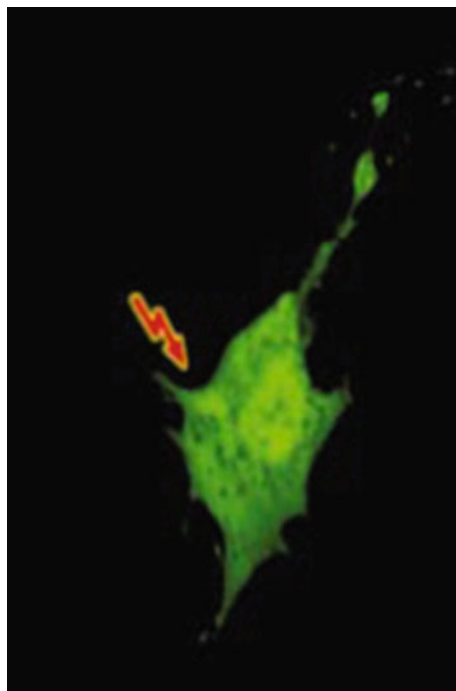


Fig. 12.77 Targeted transfection of Chinese hamster ovarian (CHO) cells with femtosecond lasers. The cell is suspended in a culture medium containing a plasmid DNA vector encoding enhanced green fluorescent protein (EGFP). A near-infrared laser pulse is focused precisely on the edge of the cell membrane (arrow) for single, site-specific, transient perforation of the cell membrane so that the transfection could occur. The expression of EGFP is clearly demonstrated throughout the cell. (Reprinted with permission from [12.270]. © 2002 Nature Publishing Group)

Caenorhabditis elegans nematode worms, that totals 302 neurons, for the ablation of entire neuronal cell bodies. But smaller structures, such as axons and dendrites, have not been targeted. To overcome this limitation, femtosecond laser dissection has been applied to *C. elegans*, where in a bundle of fluorescently labeled neurons the middle neuron was severed without the disruption of the neighboring neurons (Fig. 12.78a, b). For the study of the regeneration of motor neurons, laser surgery in *C. elegans* [12.272] and labeling with green fluorescent protein were employed. These neurons extend circumferential axons to form synapses with body muscles. When these axons were severed by laser pulses (Fig. 12.78c–f), both ends initially retracted, but the majority of the cut axons regrew toward their distal ends within 24 h and these regenerated axons were functional.

12.9.4 Future Directions in Neurosurgery

The visage of trillions of nanorobots streaming through our blood vessels (Fig. 12.79), intent on entering cells, performing nanosurgery on our very genes

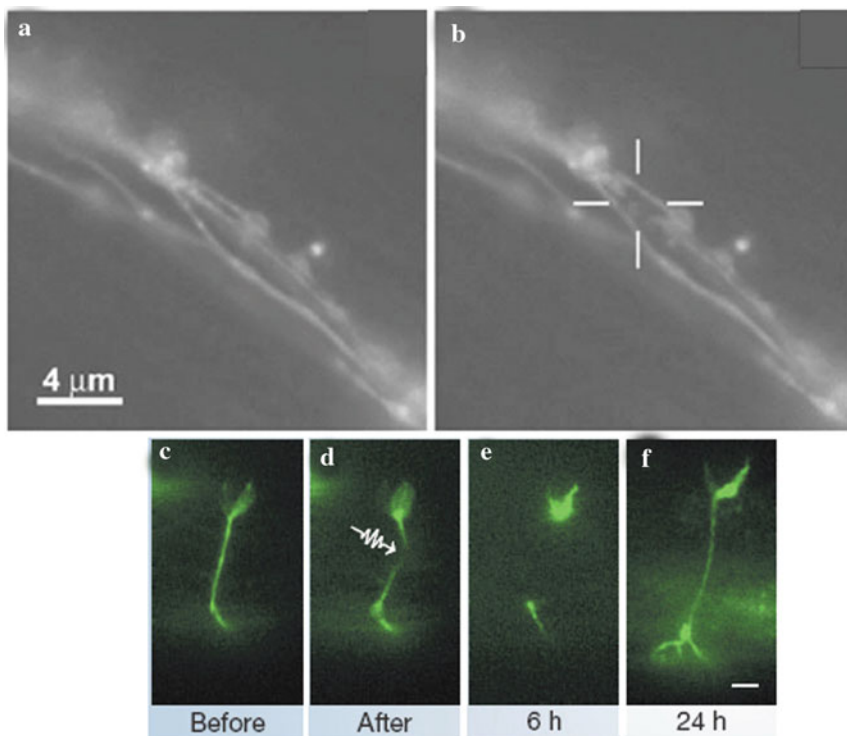
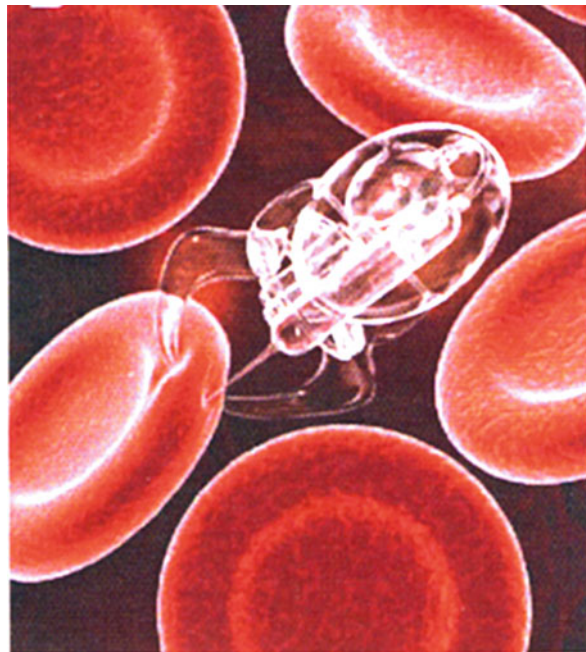


Fig. 12.78 (a, b) Femtosecond laser dissection of a single neuronal dendrite in a neuron bundle of *C. elegans* before (a) and after (b) dissection with a laser pulse of 3.6 nJ. The cross hairs in (b) indicate the region targeted by the laser. Note that the central dendrite is severed, whereas the outer two remain intact [12.267]. (c–f) Functional regeneration after laser axotomy. Fluorescent images of axons labeled with green fluorescent protein shown before, immediately after, and several hours after axotomy with femtosecond lasers. The axon has regenerated after 24 h. The arrow indicates the site of the axotomy. Scale bar: 5 μm [12.272]. (Reprinted with permission from [12.267] (a) (b) and [12.272] (c–f). © 2005 Elsevier (a) (b) and © 2004 Nature Publishing Group (c–f))

by means of femtosecond laser systems and optical tweezers, is still beyond the realm of possibility. However, current developments in nanotechnology are certain to become integrated into the delivery of medical and neurosurgical care in the near future [12.265]. Nanorobots are the stuff of science fiction. Yet, swimming microrobots propelled by artificial flagella bring that fantasy closer to reality [12.273].

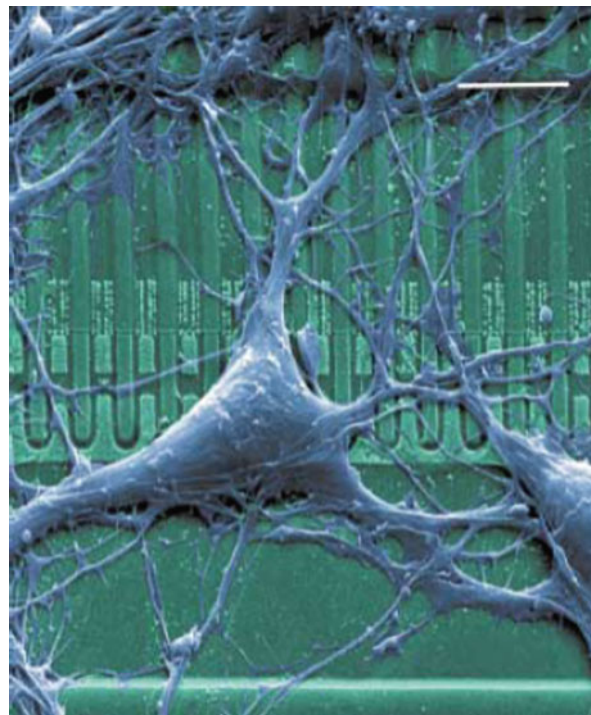
There is a number of applications of nanotechnology that are in development today that could theoretically be integrated into surgical procedures to create highly advanced therapeutic modalities [12.265]. For example, intracranial tumor labeling with systemic injection of multimodal nanoparticles could improve intraoperative visualization of tumor margins. This would be particularly useful in glioma surgery, where tumor margins are frequently indistinct, and would greatly enhance the

Fig. 12.79 Nanorobots (nanobots). Artistic conception of a nanobot injecting a single red blood cell to obtain diagnostic information or implant therapeutic agents. (Reprinted with permission from [12.265]. © 2010 agentur-focus)



capabilities of image guidance systems. In addition, after open craniotomy, nanoparticulate suspensions of drug delivery systems or microchips/nanochips could be implanted within the resection cavity for slow release of antitumor agents to provide continuous prophylaxis against tumor recurrence. Another approach would be the implantation of drug delivery systems which could be activated in the presence of tumor antigens by integrated sensitive nanosensors. Intracranial pressure monitoring and cerebrospinal fluid shunting procedures will also be impacted by developments in nanotechnology. The incorporation of integrated nanotechnology platforms such as nanofluidic chips with nanowire sensors could theoretically improve shunt performance. In addition, bulky battery packs could be replaced with nanoscale hydrogen fuel cells derived, e.g., from nanotubes. Nanowire sensors could monitor the levels of neurotransmitters, thereby providing a means to regulate the amount of neural stimulation necessary to augment neurological function. Such devices could even be implanted into the brain or spinal cord after stroke or catastrophic spinal cord injury. Significant research effort is being devoted to the study of electrical interfacing between individual neurons and silicon microchips (Fig. 12.80) with the goal of developing “brain implants” that will enable restoration of neurological function [12.274]. A platform for single axon repair using combined microtechnology and electrokinetic axon manipulation has been developed [12.275]. Nanofiber polymer scaffolds that morphologically resemble collagen fibrils can be seeded with stem cells to generate cartilage and bone tissue *in vivo*, indicative of potential application in spinal surgery [12.251]. In fact, biomimetics and the development

Fig. 12.80 Neuron–silicon interface. Colored electron micrograph of a cultured hippocampal neuron on a silicon chip with a silicon dioxide surface. An array of field-effect transistors is visible as *dark squares*. Scale bar: 10 μm . (Reprinted with permission from [12.274]. © 2002 Wiley-VCH)



of bioartificial organs will be impossible without the use of molecularly manipulated nanostructures, nanoelectronic interfacing, nanoscale drug delivery systems, etc. (see [12.265]).

A nanosurgery system based on a sub-nanosecond pulsed UV laser for the localized severing of biological polymers has been employed [12.276] to study the biophysical properties of the cytoskeleton by severing microtubules (MTs) and to test the models of the dynamic cytoskeleton behavior. The organized behavior of the cytoskeleton is fundamental for biological activities [12.277] involved in the generation of cell shape, polarity, movement, cell division, and intracellular transport. Defects in cytoskeletal functions have been implicated in vascular diseases, neuronal degeneration, and cancer (see [12.276]). The mechanism of severing likely involves nonlinear absorption of highly focused laser pulses which results in confined ionization and ultimately forms a plasma (see [12.276]).

12.10 Nanodentistry

Nanodentistry will make possible maintenance of comprehensive oral health by involving the use of nanomaterials, biotechnology (including tissue engineering), and ultimately nanorobotics [12.278]. Although the last point of this listing may be

highly speculative, dentistry will be strongly impacted by the current developments in nano- and biotechnologies as discussed with a few examples in the following.

12.10.1 Nanocomposites in Dental Restoration

Dental nanocomposites [12.279] of 75 nm silica particles (Fig. 12.81) treated in 3-methacryloxypropyltrimethoxysilane (MPTS) and dispersed in a resin used for conventional restorative composites (3 M ESPE Dental Products) exhibit mechanical properties equivalent to those of microhybrid composites [12.279]. The silane MPTS acts as a good coupling agent [12.280]. One end contains three methoxy sites that potentially etherify with hydroxyls on the hydrated surface of the silica nanoparticles to produce one to three possible ether bridges and chemically bond

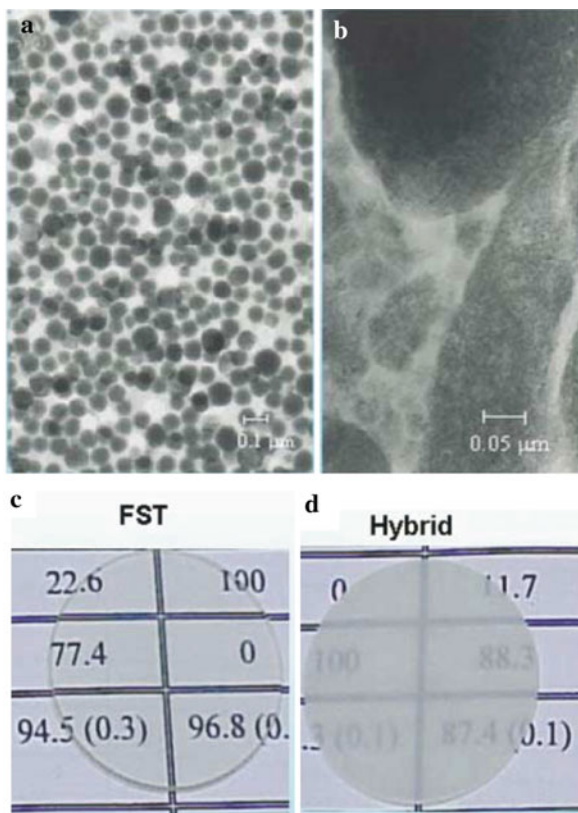


Fig. 12.81 Transmission electron micrographs and visual opacity of dental nanocomposites. (a) Composite with nanometric particles. (b) Conventional composite with a hybrid filler of micro- and nanoparticles. (c) Negligible visual opacity and full translucency of the nanocomposite. (d) Visual opacity of a composite with a hybrid filler of micro- and nanoparticles. (Reprinted with permission from [12.279]. © 2003 American Dental Association)

to that surface. The opposite end is a double-bond functional methacrylate, which becomes co-polymerized with the resin matrix to complete the chemical coupling. Yet, there is evidence of several problems in this hypothetical chain of events. The silane has a propensity to dimerize or trimerize creating methacrylate moieties that no longer can act as coupling agents, making coupling poor. Due to the nanoscale of these interactions, it has been impossible to date to measure the extent of actual chemical interaction along filler particles. Finally, when shrinkage does occur, it produces stresses at external interfaces with tooth structure and internal interfaces with filler particles. Shrinkage leads to porosity which may be concentrated at critical interfaces, having a great effect. If these shortcomings can be managed, there is a strong indication that the mechanical properties of today's composites could be substantially improved [12.280].

Nanocomposites display a much higher glossiness and a much higher gloss retention, measured after 500 tooth brush cycles, than conventional composites. This is due to the removal of particles of only nanosizes due to tooth brush abrasion. In addition, the nanocomposite shows a low visual opacity and high translucency (Fig. 12.81c, d) due to the reduced scattering of light with wavelengths much longer than the nanoparticle size. This allows the clinician to construct a wide range of shades and opacities and, thus, provide highly esthetic restoration in all posterior and anterior applications [12.279].

12.10.2 Nanoleakage of Adhesive Interfaces

The clinical performance of present day adhesives has significantly improved, allowing adhesive restoration with a high level of clinical success (see [12.281]). While the hermetic sealing between current bonding systems and the enamel of the tooth has been achieved, it is still a challenge to seal the resin–dentin interface due to the heterogeneous dentin structure and surface morphology. Bonding compromised by leakage is prone to degradation over time. Many adhesives show decreased bond strength as well as increased nanoleakage under long-term water storage [12.282]. Therefore, the sealing ability of an adhesive, providing long-term mechanical stability is of importance for the success of a resin restoration. The nanoleakage within the resin–dentin interface has been examined by studying silver penetration, from an external solution of silver salt with subsequent photodeveloping to metallic silver grains, via back-scattered electron imaging of field-emission scanning electron microscopy (FE-SEM) and energy-dispersive x-ray spectroscopy (EDS), making use of various adhesive resins. As demonstrated by negligible silver penetration (Fig. 12.82), nanoleakage can be suppressed by using a two-step self-etching adhesive (SE) or a one-bottle one-step self-etching adhesive (TB; Kuraray, Osaka, Japan; for compositions, see [12.281]). However, whereas the self-etch adhesive SE can bond strongly and stably both with the human enamel surface and with human dentin surface (see [12.281]), with regard to TB more studies concerning its bonding efficiency are necessary. Clinically, it is preferred that adhesive systems are hydrophilic during application, then become hydrophobic after application, and completely seal the restoration margins for a significant time.

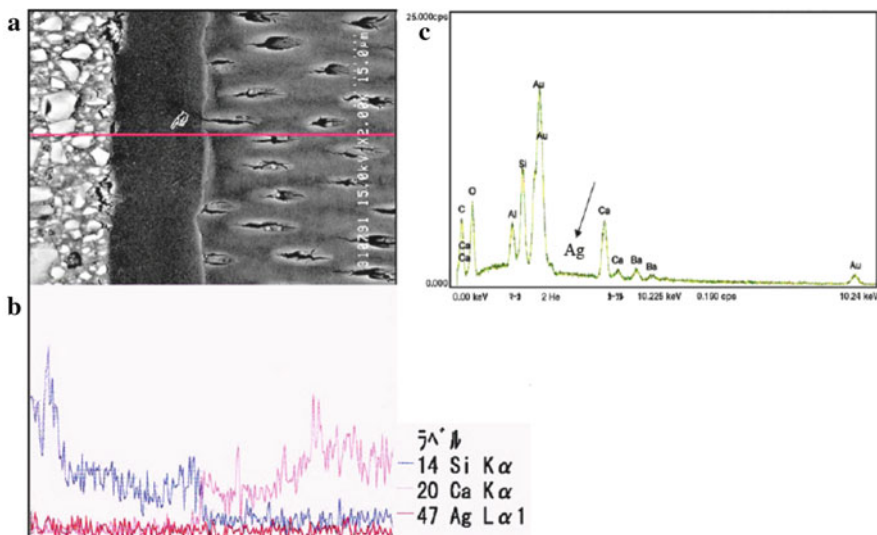


Fig. 12.82 (a) Energy-dispersive x-ray spectroscopy (EDS) of a package of composite (*left*), TB adhesive (*center*), and superficial dentin (*right*). No silver peak is visible in the energy spectra (*black arrow in c*). In subsequent line scan (**b**) along the *red line* (*finger pointer in (a)*) also no silver (*red curve*) and therefore no nanoleakage could be detected. (Reprinted with permission from [12.281]. © 2007 Elsevier)

12.10.3 Nanostructured Bioceramics for Maxillofacial Applications

Bioceramics in dentistry comprise inert, bioactive, resorbable, and composite systems. Nanophase bioceramics for clinical applications in maxillofacial surgery can be promising candidates for bone tissue engineering. Such applications may include replacement of lost teeth, filling of jaw defects or reconstruction of the mandible, and the temporomandibular joint [12.241].

Calciumphosphate ceramics (CPC; with hydroxyapatite $\text{Ca}_{10}(\text{PO}_4)_6(\text{OH})_2$) have been used for dental implants, periodontal treatment, alveolar ridge augmentation, and maxillofacial surgery. Nanophase hydroxyapatite (HA) represents a promising class of maxillofacial implant formulations with improved osseointegrative properties, because the adhesion and proliferation of osteoblasts on nano-HA are significantly higher than on conventional HA. Nanoscale alumina (Al_2O_3) and titania (TiO_2) demonstrate similar properties. In particular, increased osteoblast function on Al_2O_3 nanofibers [12.283, 12.284] suggests that these ceramics may be ideal materials for next-generation maxillofacial reconstruction with increased efficacy (see [12.241]).

On novel nanocomposites consisting of a blend of polylactic acid (PLA) and carbon nanotubes, cell proliferation can be stimulated by electric currents through

the nanotubes, making this composite also a promising material for maxillofacial implants [12.285].

12.10.4 Release of Ca–PO₄ from Nanocomposites for Remineralization of Tooth Lesions and Inhibition of Caries

Secondary caries of the tooth-restoration margins is the most-frequent reason for replacement of restorations. Replacement dentistry accounts for 70% of all operative work and costs \$5 billion/year in the United States (see [12.286]). Recent studies show that calcium (Ca) and phosphate (PO₄) ions can be released from composites to supersaturated levels for apatite precipitation and remineralization of tooth lesions in vitro [12.287]. For enhanced Ca and PO₄ release from a high-strength dental material, a composite of nanophase CaHPO₄ (DCPA), β -Si₃N₄ whiskers (length \sim 5 μ m, diameter \sim 0.4 μ m) fused with 40 nm SiO₂ particles, and a two-part chemically activated resin was synthesized [12.286]. At a mass fraction of the filler (DCPA + whiskers) of 75%, the flexural strength of 114 MPa was not much different from the 112 MPa of a hybrid control. The elastic modulus of the nanocomposite, 14.9 GPa, was higher than that of the control hybrid (11.7 GPa). The release of Ca and PO₄ ions from a $2 \times 2 \times 12$ mm³ composite specimen with 75% filler, in a 50 mL NaCl solution after 56 days was 0.65 mmol/L Ca and 2.29 mmol/L PO₄.

The elastic modulus of the composite with 75% filler is somehow lower than the 18 GPa of dentin, but higher than the 11.7 GPa of the commercial, stress-bearing, non-releasing composite control. The ion release properties of the present nanocomposite are superior to those of earlier microphase Ca–PO₄ composites with a release of 0.3–1.0 mmol/L of Ca and 0.1–0.7 mmol/L of PO₄ [12.287]. The nonlinear dependence of the ion release on the DCPA volume fraction (Fig. 12.83) may be

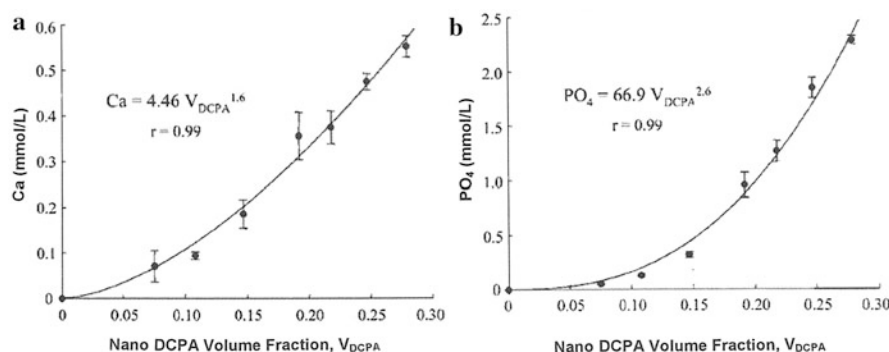


Fig. 12.83 Relationships between (a) Ca and (b) PO₄ release and nano-DCPA volume fraction V_{DCPA} . (Reprinted with permission from [12.286]. © 2007 SAGE)

due to a decrease of the resin polymerization conversion with increasing filler level and consequently an increased diffusion flow of water and ions through the resin.

Regarding the potential applications of the nano-DCPA-whisker composites with the combination of stress-bearing and caries-inhibiting capabilities, the composites with 30–50% fillers may be suitable for use as Ca–PO₄-releasing tooth cavity liners, adhesives, and pit-and-tissue sealants. Flowable DCPA-whisker composites with 50–60% filler may be used as crown cements and orthodontic bracket cements, and to repair defective margins. Composites with 70–75% fillers may be useful in stress-bearing and caries-inhibiting restorations [12.286].

12.10.5 Growing Replacement Bioteeth

Lost teeth are usually replaced with inert prosthetic versions. After age 50, an average of 12 teeth stand to have been lost. In theory, a natural tooth made from the patients own tissue and grown in its intended location would be the best replacement, although such bioengineered teeth have been little more than a dream. Recently, however, progress in understanding how teeth first develop has combined with advances in stem cell biology and tissue engineering to bring us close to the realization of biological replacement teeth. Moreover, teeth will serve as a crucial test of the feasibility of different tissue engineering techniques because mistakes with teeth would not be life threatening and could be corrected [12.288]. A good way to start learning how to build teeth, therefore, is to observe how nature does it.

Six weeks after conception, when a human embryo is less than an inch long, cells are already guiding the formation of its teeth (see [12.288]). Oral epithelial cells (which are destined to line oral cavities) send out the first instructions to mesenchymal cells (which will produce jawbone and soft tissue) to begin odontogenesis or tooth formation. A tooth bud is formed by the embryo's seventh week and a bell-shaped structure after 14 weeks [12.288]. Eventually, the epithelium will become the visible outer enamel of the tooth that erupts from the baby's gum line some 6–12 months after birth, and the mesenchymal cells will have formed the non-visible parts of the tooth, such as dentin, dental pulp, cementum, and periodontal ligament that attaches the tooth to the jawbone. The shape of a tooth will be determined by its position via the so-called homebox genes. The homebox gene called *Barx1*, for example, is switched on, or expressed, by mesenchymal cells in the positions where molar teeth will grow. Because the ability to predict and control tooth shape will be essential for the creation of engineered teeth, scientists can use genes such as *Barx 1* as predictive markers of future shape for teeth created in the lab [12.288].

Three milestones must be reached for the engineering of replacement biological teeth. Sources of cells that can form teeth and are easily obtained from patients themselves must be identified. These teeth must be able to develop in the adult jaw, producing roots. And the shape of the biological teeth must be predictable so that they match the patient's own teeth. Experiments for growing teeth from scratch are primarily performed with mouse cells [12.288]. For example, when stem

cells from adult bone marrow took the place of oral mesenchymal cell populations, the transplanted constructs produced structurally correct teeth, demonstrating that embryonic mesenchyme can be replaced with adult stem cells to generate new teeth. Efforts are continuing for seeking an effective population of substitute cells that could be derived from an adult source [12.288]. In addition, human somatic cells reprogrammed to induced pluripotent stem cells (iPS) [12.289, 290], that exhibit the essential characteristics of embryonic stem cells, could be envisaged to induce the appropriate initiating signals for odontogenesis.

The next experimental step was to see whether teeth could be formed within the mouth. For that, tooth buds from embryonic mice were transplanted into the diastema, the empty region between the molars and incisors, in the upper jaw of adult mice. Three weeks later, the teeth identified in the diastema had formed in the correct orientation, were of appropriate size for the mice, and were attached to underlying bone by soft connective tissue (see [12.288]).

A problem for the teeth generated by any of the tissue engineering methods was that they did not develop roots [12.287]. Efforts were, however, recently focused on stem cells found in the root apical papilla, tissue connected to the tip of the root that is responsible for the root's development [12.291]. These apical papilla cells, which can be considered as younger stem cells [12.291] than pulp cells, provide better tissue regeneration – leading to the formation of all root tissues as well as dentin and cementum, the support substances located in the crown and root, respectively. After the identification of stem cells for creating a new root, an incisor extracted from a miniature pig, which has a similar dental structure to humans, was replaced with stem cells from the extracted wisdom teeth of 18- to 20-year-old humans. Three months after loading the apical papilla stem cells into the incisor socket of the pig, a porcelain crown has been fitted over the mineralized roots and ligaments developing there. Six months after stem cell implantation, the tooth was believed to have a strength sufficient to withstand normal wear and tear [12.292].

12.11 Risk Assessment Strategies and Toxicity Considerations

At the nanoscale, material properties vary as a function of size, which not only enables new benefits but also may lead to unintended health and environmental risks [12.293]. The increased presence of nanomaterials in commercial products has resulted in a growing public debate on the toxicological and environmental effects of direct and indirect exposure to these materials. At present, these effects are not completely elucidated [12.294], but this topic is discussed by a number of agencies and workshops (see, e.g., [12.293, 12.295–12.305]). However, the “...overall federal government (USA) response to identifying and managing nanotechnology risks...” are described as “...slow, badly conceptualized, poorly directed, uncoordinated and undefended...” (see [12.306]). But a number of efforts have been initiated worldwide to investigate the toxicological effects of nanomaterials, including the program “Nanocare” of the German Federal Government [12.307]. Yet, the National

Research Council of the United States criticizes the recent federal nanotechnology plan for lacking risk research [12.308]. The report of the UK Royal Commission on Environmental Pollution (RCEP) [12.309] has concluded that the existing framework of regulation is sufficient and with adaptions should be capable of dealing with the use of nanomaterials.

The concern that nanotechnology will go out of control has been put forward by several futurists [12.310–12.312] and adopted gleefully by science fiction writers [12.313, 12.314]. It is the idea of small machines that can replicate themselves (“assemblers”) and that escape the laboratory. Many scientists, however, see no way that such devices can exist and that this concern can be dismissed [12.315].

A most serious risk of nanotechnology may arise from the fast development of electronics, computers, and telecommunication – fast processors, ultradense memory, methods for searching data bases, ubiquitous sensors, electronic commerce, and banking – into most aspects of life, which is making it increasingly possible to collect, store, and sort enormous quantities of data about people [12.316].

The public perception of nanotechnology is currently studied [12.317, 12.318]. In studies aimed at determining how members of the public would react to balance information about nanotechnology risks and benefits, no evidence for the “familiarity hypothesis” has been reported that support for nanotechnology will grow as awareness of it expands [12.319]. Studies of the influence of religious beliefs on attitudes toward nanotechnology in the United States and Europe showed more positive attitudes about nanotechnology among less religious people [12.320].

In the present section, strategies will be described for environmental, health, and safety (EHS) research and how to gain information needed to enable sound risk assessment and risk management decision making [12.295] in order to guide commercial development [12.293, 12.298, 12.320]. Finally, the present state of specific toxicity studies on various types of nanoparticles [12.294, 12.321–12.323] will be outlined.

12.11.1 Risk Assessment and Biohazard Detection

Risk assessment and biohazard detection of nanomaterials has to comprise the following aspects [12.295]:

- nanomaterial characterization,
- standard terminology,
- standard reference nanomaterials,
- techniques for detecting nanomaterials in biological media,
- in vivo tests and correlation to in vitro tests
- in vitro test validation, and
- model development

Research needs are, furthermore, categorized within the following areas:

- metrology for risk measurement,
- assessment of bioavailability, and
- characterization of potential mobility of embedded nanomaterials

Within these aspects, information on nanoparticle translocation, agglomeration, and toxicity are of particular relevance. In addition, the adequacy of traditional toxicology tests should be scrutinized and cross-disciplinary communication is a prerequisite [12.298].

For *toxicology tests* cytotoxicity assays are utilized (see [12.321]). One simple cytotoxicity test involves visual inspection of cells with bright-field microscopy for changes in cellular or nuclear morphology. However, the majority of cytotoxicity assays used measure cell death via colorimetric methods. Neutral red is a dye that can cross the plasma membrane by diffusion. If the cell membrane is altered, the uptake of neutral red is decreased, allowing for discernment between live and dead cells. Trypan blue is only permeable to cells with compromised membranes; therefore, dead cells are stained blue while live cells remain colorless. The LIVE/DEAD viability test, which includes the two chemicals calcein acetoxyethyl and ethidium homodimer is another assay measuring the number of damaged cells. A third cytotoxicity assay used in several carbon nanoparticle studies (see [12.321]) is lactate dehydrogenase (LDH) release monitoring, where the amount of LDH released is proportional to the number of cells damaged or lysed. The most widely used test is the 3-(4,5 dimethylthiazol-2-yl)-2,5-diphenyl tetrazolium bromide (MTT) viability assay for mitochondria activity which prevails only in living cells.

12.11.2 Cytotoxicity Studies on Carbon, Metal, Metal Oxide, and Semiconductor-Based Nanoparticles

In general, cells can survive short-term exposure to low concentrations (< 10 $\mu\text{g}/\text{mL}$) of nanoparticles. However, at high doses, several groups have found cytotoxic effects (see [12.321]). As causes for the increase in cell death observed at higher concentrations, the generation of reactive oxygen species, and the influence of cell internalization of nanoparticles are common findings.

While much of the function of nanoparticles is due to their core structure, the surface coating defines much of their bioactivity [12.321]. Surface charge also plays a role in toxicity, with neutral surfaces being most biocompatible. Even if no cell damage or death may be apparent after nanoparticle exposure, changes in cellular function may result. Therefore, sub-lethal cellular changes should also be taken into account and tested for, e.g., by genomic and proteomic array tests to explore the cellular signaling alterations behind the toxicity. Furthermore, it should be pointed out that although nanoparticle-induced cytotoxicity has been reported by several

groups, it should be kept in mind that *in vitro* results can differ from what is found *in vivo* and are not necessarily clinically relevant [12.321].

In the following, a selection of studies of the toxicological impact of nanoparticles will be presented (see [12.294, 12.321, 12.322]).

Carbon and organic nanoparticles. Pristine C₆₀ is considered to be fairly non-toxic (see [12.321]), whereas C₆₀ derivatives are relatively non-toxic at low concentration (0.24 ppb) but more cytotoxic at the highest concentration [12.324].

Single-walled carbon nanotubes (SWNTs) have typically been labeled as having cytotoxic effects at high concentrations (see [12.321]). As illustrated in Fig. 12.84, cell death was highest in the cultures exposed to pristine SWNTs while functionalized SWNTs can yield high cell viability. It may be mentioned here that biodegradation of SWNTs through natural, enzymatic catalysis has been demonstrated recently [12.326].

Long fibers (>20 μm) of multiwalled carbon nanotubes (MWNTs) cause inflammation of the mesothelium of mice [12.327], the cell layer that covers the chest (pleural) peritoneal cavities, similar to asbestos, whereas the samples without long but short fibers did not induce inflammatory response. This short-term study [12.327] does not show whether the inflammatory response leads to mesothelioma (cancer).

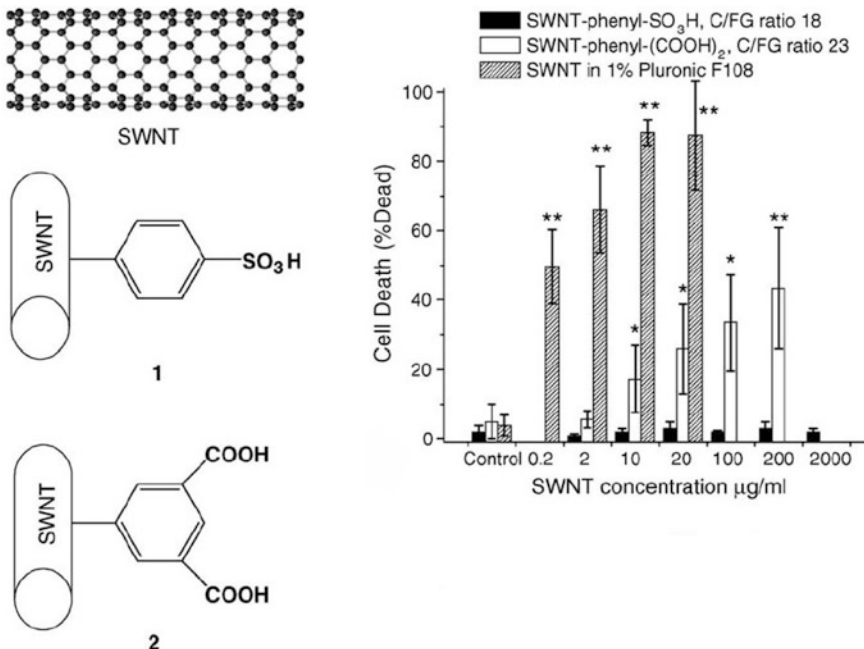


Fig. 12.84 Structure and human dermal fibroblast cytotoxicity data for single-walled carbon nanotubes (SWNTs) and derivatives [12.321, 12.325]. (Reprinted with permission from [12.335]. © 2006 Elsevier)

Cationic polyamidoamine (PAMAM) nanoparticles, a class of nanomaterials that are being widely developed for clinical applications, can induce acute lung injury *in vivo*. Potential remedies are suggested [12.328].

Nanostructured metals. Au nanoparticles have great promise for bioimaging and therapy. Large nanoparticles (18 nm) with surface modifiers did not appear to be toxic at concentrations up to 250 μM [12.329]. In contrast, 1.4 nm Au nanoparticles stabilized by triphenylphosphine cause rapid cell death by necrosis [12.330] as shown by the IC_{50} values (the half-maximal inhibitory concentration – the concentration of an inhibitor that is required to achieve 50% target inhibition) in MTT assays.

Gold nanoshells, which are being developed for imaging contrast and photothermal therapeutic medical applications, show no physiological complications in mice [12.331].

Metal oxide nanoparticles. These types of nanoparticles are used in cosmetics and sunscreens (TiO_2 , ZnO), dental fillers (SiO_2), or as contrast materials for magnetic resonance imaging (iron oxide, see Sect. 12.2). It should be pointed out, however, that TiO_2 absorbs about 70% of the incident UV radiation which leads for TiO_2 with anaphase structure (see [12.305]) in aqueous environments to the generation of hydroxyl radicals ($\cdot\text{OH}$). This may cause DNA strand breaks in human cells [12.332]. In other assessments (see [12.333]) TiO_2 and ZnO nanoparticles have been stated to be safe and non-toxic.

Whereas bare iron oxide nanoparticles at 250 $\mu\text{g}/\text{mL}$ concentrations were shown to induce a loss in fibroblast viability [12.334], poly(ethylene glycol) (PEG)-coated iron oxide nanoparticles are found to be relatively non-toxic [12.335].

Charged nanoparticles can alter the local physical properties of lipid membranes, which could shed light on the interactions between living cells and nanomaterials [12.336].

Semiconductor nanoparticles. Since some of these nanoparticles or quantum dots (QDs) are composed of toxic elements including Cd, Se, Pb, and As, toxicity may be related to the release of free metal ions and the crucial factor, therefore, is stability. In mouse models, no toxicity was observed for ZnS-capped CdSe QDs coated with poly(ethylene glycol) (PEG) [12.337] where the ZnS shell is efficient in reducing the cytotoxicity of the CdSe QDs. *In vitro* cytotoxicity studies report findings similar to *in vivo* studies. Targeted CdSe/ZnS QDs can be internalized by HeLa cells and tracked in live cells for more than 10 days with no morphological signs of toxicity [12.338]. The QDs are internalized mainly within endosomes near the perinuclear region with no nuclear involvement (see [12.321]). It has been shown, however, that QDs can alter gene expression in human bone marrow mesenchymal stem cells [12.338], which can be reduced by PEG treatment of the QDs. Organic-coated CdSe/ZnS core–shell quantum dots, while safe to use at near-neutral pH, could be toxic under other conditions [12.339]. Small CdTe QDs were shown to penetrate the cell nucleus where they could cause damage to DNA and induce apoptosis or cell death. QD cytotoxicity is believed to be due to free-radical formation caused by the presence of free Cd^{2+} from the degradation of the QD core [12.321, 12.340].

At the current stage in nanoparticle safety research, it would be premature to conclude that nanoparticles are inherently dangerous. However, now that a basis has been established, future research should strive to address the deficiencies in current testing and exploit the findings to engineer improved nanoparticles ultimately, e.g., for clinical use [12.321].

12.12 Summary

Nanomedicine comprises the application of nanoscience for diagnosis, treatment, monitoring, and control of biological systems to achieve medical benefit. Nanotechnology is positively impacting health care. Nanoscale and biosystems research are merging with information technology and cognitive science, leading to completely new science and technology platforms such as those for genome pharmaceutic, biosystems on a chip, regenerative medicine, neuroscience. At the forefront of nanomedicine is the research into the delivery and targeting of diagnostic and therapeutic agents with the identification of precise targets and the choice of appropriate nanocarriers to achieve the required responses while minimizing side effects. An impact of nanotechnology on health care is expected by experts with full efficiency around 2020 at many levels including detection of molecular changes in disease pathogenesis, disease diagnosis and imaging, drug delivery and therapy, multifunctional systems for combined diagnosis and therapeutic application, vehicles to report the *in vivo* efficacy of therapeutic agents, and nanoscience basic research. The convergence of nanoscience with biology and medicine is reflected in science policy decisions, initiating the sponsoring of Nanomedicine Development Centers and the channeling of substantial amounts of money into nanomedicine projects. Some nanoparticles have already gained approval by the US Food and Drug Administration (FDA) but outstanding issues related to risk assessment strategies, toxicity considerations, and environmental impact of nanoscale materials have to be resolved before regulatory agencies can approve further pharmaceutical products.

References

- 12.1 S.M. Moghimi et al., *FASEB J.* **19**, 311 (2005)
- 12.2 <http://www.esf.org/puplication/214/Nanomedicine.pdf>
- 12.3 Editorial, *Nat. Mater.* **5**, 243 (2006)
- 12.4 O.C. Farokhzad, R. Langer, *Adv. Drug Delivery Rev.* **58**, 1456 (2006)
- 12.5 M.C. Roco, *Curr. Opin. Biotechnol.* **14**, 337 (2003)
- 12.6 C. Peng et al., *Phys. Rev. E* **75**, 041903 (2007)
- 12.7 N. Shen et al., *Mech. Chem. Biosys.* **2**, 17 (2005)
- 12.8 R.H. Austin, S.-F. Lim, *Proc. Natl. Acad. Sci. USA* **105**, 17217 (2008)
- 12.9 A.D. Maynard et al., *Nature* **444**, 267 (2006)
- 12.10 S.M. Moghimi, T. Kissel, *Adv. Drug. Deliv. Rev.* **58**, 1451 (2006)
- 12.11 M. Harris et al., *J. Clin. Oncol.* **23**, 7768 (2005)

12.12 N.L. Rosi, C.A. Mirkin, *Chem. Rev.* **105**, 1547 (2005)
12.13 P. Alivisatos, *Nat. Biotechnol.* **22**, 47 (2003)
12.14 S.P. Leary et al., *Neurosurgery* **58**, 805 (2006)
12.15 MRS Bulletin **30**, December 2005, p. 930
12.16 http://www.cordis.europa.eu/fetch?Caller=EN_NEWS&ACTION=D...
12.17 A.S. Barnard, *Nat. Mater.* **5**, 245 (2006)
12.18 R. Weissleder, M.J. Pittet, *Nature* **452**, 580 (2008)
12.19 V.P. Torchilin, *Adv. Drug Deliv. Rev.* **58**, 1532 (2006)
12.20 J.-W. Jun et al., *Bull. Korean Chem. Soc.* **27** (7), 961 (2006)
12.21 C. Corot et al., *Adv. Drug Deliv. Rev.* **58**, 1471 (2006)
12.22 M.G. Harisinghani et al., *New Engl. J. Med.* **348**, 2491 (2003)
12.23 J.-H. Lee et al., *Nat. Med.* **13**, 95 (2007)
12.24 M.F. Kircher et al., *Cancer Res.* **63**, 8122 (2003)
12.25 H. Kobayashi et al., *J. Natl. Cancer Inst.* **96**, 703 (2004)
12.26 R.A.M. Heesakkers et al., *Radiolog.* **239**, 481 (2006)
12.27 A. Laghi et al., *Invest. Radiol.* **39**, 666 (2004)
12.28 I.J. de Jong et al., *Eur. Urol.* **42**, 18 (2002)
12.29 G.H. Simon et al., *J. Magn. Reson. Imaging* **23**, 720 (2006)
12.30 M. Stoltz et al., *Nat. Nanotech.* **4**, 186 (2009)
12.31 A.M. Lutz et al., *Radiology* **234**, 765 (2005)
12.32 O. Rabin et al., *Nat. Mater.* **5**, 118 (2006)
12.33 E.R. Wisner et al., *Invest. Radiol.* **38**, 358 (2003)
12.34 P. Schrenk et al., *Eur. J. Surg. Oncol.* **27**, 378 (2001)
12.35 M.D. Lu et al., *Ultrasound Med. Biol.* **33**, 1736 (2007)
12.36 W.Y. Lau et al., *Ann. Surg.* **237**, 171 (2003)
12.37 T. Albrecht et al., *Ultraschall Med.* **25**, 249 (2004)
12.38 R. Weissleder, *Science* **312**, 1168 (2006)
12.39 A. Quon, S.S. Gambhir, *J. Clin. Oncol.* **23**, 1664 (2005)
12.40 H.A. Wieder et al., *J. Clin. Oncol.* **22**, 900 (2004)
12.41 N. Avril et al., *J. Clin. Oncol.* **23**, 7445 (2005)
12.42 S. Surti et al., *IEEE Trans. Nucl. Sci.* **50**, 1357 (2003)
12.43 J.S. Karp et al., *J. Nucl. Med.* **44**, 1340 (2003)
12.44 S.I. Ziegler et al., *J. Nucl. Med.* **41**, 20 (2000)
12.45 D.H.S. Silverman, A. Alavi, *Radiol. Clin. N. Am.* **43**, 67 (2005)
12.46 D.H. S. Silverman, *J. Nucl. Med.* **45**, 594 (2004)
12.47 W.J. Powers, A.R. Zazulia, *Neuroimaging Clin. N. Am.* **13**, 741 (2003)
12.48 H.-P.W. Schlemmer et al., *Radiolog.* **248**, 1028 (2008)
12.49 F.A. Jaffer et al., *Circulatio.* **116**, 1052 (2007)
12.50 M. Fleischmann et al., *Chem. Phys. Lett.* **26**, 163 (1974)
12.51 S. Keren et al., *Proc. Natl. Acad. Sci. USA* **105**, 5844 (2008)
12.52 Y.W. Wang et al., *Nano Lett.* **4**, 1689 (2004)
12.53 X.M. Yang et al., *Nano Lett.* **7**, 3798 (2007)
12.54 B. Marte et al., *Nature* **452**, 547 (2008)
12.55 A.D. Weston, L. Hood, *J. Proteome Res.* **3**, 179 (2004)
12.56 M.M.-C. Cheng et al., *Curr. Opin. Chem. Biol.* **10**, 11 (2006)
12.57 M. Stoeckli et al., *Nat. Med.* **7**, 493 (2001)
12.58 S. Pan et al., *Mol. Cell. Proteomics* **4**, 182 (2005)
12.59 D.G. Georganopoulou et al., *Proc. Natl. Acad. Sci. USA* **102**, 2273 (2005)
12.60 R.A. Beckman et al., *J. Appl. Phys.* **96**, 5921 (2004)
12.61 L. Hood et al., *Science* **306**, 640 (2004)
12.62 R. Beckman et al., *Science* **310**, 465 (2005)
12.63 T. Thundat, A. Majumdar, *Sensors and Sensing in Biology and Engineering* (Springer, Berlin 2003)

12.64 C. Ziegler, Anal. Bioanal. Chem. **379**, 946 (2004)
12.65 R. Datar et al., MRS Bull. **34**, 449 (2009)
12.66 M. Alvarez et al., Langmuir **20**, 9663 (2004)
12.67 R. Mukhopadhyay et al., Langmuir **21**, 8400 (2005)
12.68 B.L. Weeks et al., Scanning **25**, 297 (2003)
12.69 H.F. Ji et al., Expert Rev. Mol. Diagnostics **47**, 859 (2004)
12.70 G. Wu et al., Nat. Biotechnol. **19**, 856 (2001)
12.71 H. Chen et al., Biomed. Microdevices **6**, 55 (2004)
12.72 X.H. Gao et al., Nat. Biotechnol. **22**, 969 (2004)
12.73 V. Ntzachristos et al., Eur. Radiol. **13**, 195 (2003)
12.74 R.E. Bailey, S.M. Nie, J. Am. Chem. Soc. **125**, 7100 (2003)
12.75 K.N. Yu et al., Bioconjugate Chem. **18**, 1155 (2007)
12.76 P.L. Yeagle, *Biology of Cholesterol* (CRC Press, Boca Raton, 1988)
12.77 S. Avaramudhan et al., Biosens. Bioelectron. **22**, 2289 (2007)
12.78 S.T. Reddy et al., Nat. Biotechnol. **25**, 1159 (2007)
12.79 P. Yager et al., Nature **442**, 412 (2006)
12.80 A.C. R. Grayson et al., Nature Mater. **2**, 767 (2003)
12.81 T. Franke, A. Wixforth, Phys. Unserer Zeit 2/2007 (38), p. 88
12.82 M.A. Unger et al., Science **288**, 113 (2000)
12.83 G. MacBeath, S.L. Schreiber, Science **289**, 1760 (2000)
12.84 D.R. Walt, Science **287**, 451 (2000)
12.85 E.S. Lander, Nat. Genet. **21**, 3 (1999)
12.86 D.S. Ginger et al., Angew. Chem. Int. Edn. Engl. **43**, 30 (2004)
12.87 K.B. Lee et al., Nano Lett. **4**, 1869 (2004)
12.88 J.W. Hong et al., Nat. Biotechnol. **22**, 435 (2004)
12.89 T.H. Wang et al., J. Am. Chem. Soc. **127**, 5354 (2005)
12.90 J.W. Hong, S.R. Quake, Nat. Biotechnol. **21**, 1179 (2003)
12.91 P.R. Srinivas et al., Lab. Invest. **82**, 657 (2002)
12.92 M. Ferrari, Nat. Rev./Cance. **5**, 161 (2005)
12.93 R. McKendry et al., Proc. Natl. Acad. Sci. USA **99**, 9783 (2002)
12.94 M. Su et al., Appl. Phys. Lett. **82**, 3562 (2003)
12.95 R. Pantoja et al., Biosens. Bioelectron. **20**, 509 (2004)
12.96 F. Patolsky et al., Proc. Natl. Acad. Sci. USA **101**, 14017 (2004)
12.97 P. Gould, Materialstoday **11**, July – August 2008, p. 17
12.98 J. Pipper et al., Angew. Chem. Int. Edn. **47**, 3900 (2008)
12.99 T.A. Desai et al., Biomed. Microdevices **1**, 131 (1999)
12.100 P. Sinha et al., Nanotechnology **15**, S585 (2004)
12.101 M. Arruebo et al., Nanotoday **2**, June 2007, p. 24
12.102 ISI Web of Knowledge © The Thomson Corporation. Search terms: 'drug delivery' and 'nanoparticles'. Date of search: December 2006)
12.103 R. Langer et al., Nat. Mater. **8**, 444 (2009)
12.104 J. Lu et al., small. **3**, 1341 (2007)
12.105 I.I. Slowing et al., J. Am. Chem. Soc. **129**, 8845 (2007)
12.106 Y. Pommier, Nat. Rev. Cancer **6**, 789 (2006)
12.107 L. Lacerda et al., Nanotoday **2**, Dec. 2007, p. 38
12.108 L.A. Nagahara et al., MRS Bull. **34**, 406 (2009)
12.109 M.P. Melancon et al., MRS Bull. **34**, 415 (2009)
12.110 R.H. Liu et al., MRS Bull. **34**, 432 (2009)
12.111 W.B. Lin et al., MRS Bull. **34**, 441 (2009)
12.112 A. Bajaj et al., Proc. Nat. Acad. Sci. USA **106**, 10912 (2009)
12.113 M.R. Stratton et al., Nature **458**, 719 (2009)
12.114 E.C. Hayden, Nat. **458**, 131 (2009)

12.115 S. Kommareddy, M. Amiji, *Cancer Gene Therap.* **14**, 488 (2007)
12.116 G. Mahendra et al., *Cancer Gene Ther.* **12**, 26 (2005)
12.117 S. Lehrman, *Nature* **401**, 517 (1999)
12.118 F. Yuan et al., *Cancer Res.* **54**, 4564 (1994)
12.119 N.L. Rosi et al., *Science* **312**, 1027 (2006)
12.120 W.D. Peng et al., *The Prostate* **67**, 855 (2007)
12.121 S. Dhar et al., *Proc. Natl. Acad. Sci. USA* **105**, 17356 (2008)
12.122 M.V. Yezhelyev et al., *J. Am. Chem. Soc.*, **130**, 9006 (2008)
12.123 Z. Zhang et al., *Clin. Cancer Res.* **12**, 4933 (2006)
12.124 P.G. Rose, *Oncologist* **10**, 205 (2005)
12.125 H. Wartlick et al., *J. Drug Target* **12**, 461 (2004)
12.126 R.M. Schiffelers et al., *J. Control. Release* **91**, 115 (2003)
12.127 A.K. Salem et al., *Nat. Mater.* **2**, 668 (2003)
12.128 J. Wang et al., *J. Drug Target* **13**, 73 (2005)
12.129 K.E. Bullock et al., *Mol. Imaging* **5**, 1 (2006)
12.130 U. Schillinger et al., *J. Magn. Magn. Mater.* **293**, 501 (2005)
12.131 M. Arruebo et al., *Nanotechnology* **17**, 4057 (2006)
12.132 J.Q. Zhang et al., *Pharm. Res.* **22**, 573 (2005)
12.133 P. Taepaiboon et al., *Nanotechnology* **17**, 2317 (2006)
12.134 U. Steinfeld et al., *Int. J. Pharm.* **311**, 229 (2006)
12.135 F. Wiekhorst et al., *J. Nanosci. Nanotechnol.* **6**, 3222 (2006)
12.136 C.J. Sunderland et al., *Drug Develop. Res.* **67**, 70 (2006)
12.137 D.W. Chakeres, F. Vocht, *Prog. Biophys. Molec. Biol.* **87**, 255 (2005)
12.138 A.J. Rosengart et al., *J. Magn. Magn. Mater.* **293**, 633 (2005)
12.139 O. Rotarin, N.J.C. Strachan, *J. Magn. Magn. Mater.* **293**, 639 (2005)
12.140 S.M. Moghimi, T. Kissel, *Adv. Drug Deliv. Rev.* **58**, 1451 (2006)
12.141 S.H. Kim et al., *J. Am. Chem. Soc.* **129**, 2669 (2007)
12.142 Y.-E.L. Koo et al., *Adv. Drug Deliv. Rev.* **58**, 1556 (2006)
12.143 K.A. Dawson et al., *Nat. Nanotechnol.* **4**, 84 (2009)
12.144 L.L. Maldoon et al., *Neurosurgery* **57**, 785 (2005)
12.145 G.X. Xu et al., *Bioconjugate Chem.* **19**, 1179 (2008)
12.146 <http://www.medicalnewstoday.com/medicalnews.php?newsid=18716>
12.147 A. Moore et al., *Radiology* **214**, 568 (2000)
12.148 E.A. Neuwelt et al., *Neuropathol. Appl. Neurobiol.* **30**, 456 (2004)
12.149 O. Veiseh et al., *NanoLett.* **5**, 1003 (2005)
12.150 S.C. Steiniger et al., *Int. J. Cancer* **109**, 756 (2004)
12.151 W. Tang et al., *Photochem. Photobiol.* **81**, 242 (2005)
12.152 R. Kopelman et al., *J. Magn. Magn. Mater.* **293**, 404 (2005)
12.153 W.H. Sub et al., *Nanotoday* **4**, 2 (2009)
12.154 T.-Y. Liu et al., *Nanotoday* **4**, 52 (2009)
12.155 K. Shimizu et al., *Export Opin. Ther. Targets* **9**, 63 (2005)
12.156 E. Ruoslathi et al., *Curr. Pharm. Des.* **11**, 3655 (2005)
12.157 D. Le Bihan et al., *Radiology* **161**, 401 (1986)
12.158 J. Overgard in J. Overgard, ed. *Hyperthermia Oncology* (Taylor and Francis, London, 1985)
12.159 S.J. DeNardo et al., *J. Nucl. Med.* **48**, 437 (2007)
12.160 C.J. Gannon et al., *Cancer* **110**, 2654 (2007)
12.161 L.R. Hirsch et al., *Proc. Nat. Acad. Sci. USA* **100**, 13549 (2003)
12.162 L.R. Hirsch et al., *Ann. Biomed. Eng.* **34**, 15 (2006)
12.163 M. Johannsson et al., *Int. J. Hyperthermia* **21**, 637 (2005)
12.164 A. Jordan et al., *J. Magn. Magn. Mater.* **225**, 118 (2001)
12.165 K. Kupferschmidt, *Stuttgarter Zeitung* July 16, 2009
12.166 D. Haemmerich, P.F. Laeseke, *Int. J. Hyperthermia* **21**, 755 (2005)

12.167 P.F. Engstrom et al., in *Cancer Medicine*, vol. 7, eds. D.W. Kufe et al., (B.C. Dekker, Hamilton, Canada, 2006) p.1292

12.168 C.H. Durney et al., *Radiofrequency Radiation Dosimetry Handbook*, 4th edn. (Brooks AFB, Tex: U. S. Air Force School of Aerospace Medicine Press, 1986)

12.169 L.D. Landau, E.M. Lifshitz, *Electrodynamics of Continous Media* (Elsevier, Oxford, 2004)

12.170 H. Dumortier et al., *NanoLett.* **6**, 1522 (2006)

12.171 R. Singh et al., *Proc. Natl. Acad. Sci. USA* **103**, 3357 (2006)

12.172 N.W. Kam et al., *Proc. Natl. Acad. Sci.* **102**, 11600 (2005)

12.173 J.C. Hindman, *J. Chem. Phys.* **44**, 4582 (1966)

12.174 W.R. Chen et al., *Cancer Lett. (Shannon, Ire)* **98**, 169 (1996)

12.175 H. Maeda, *Adv. Enzyme Regul.* **41**, 189 (2001)

12.176 C. Loo et al., *NanoLett.* **5**, 709 (2005)

12.177 P. Chakravarty et al., *Proc. Natl. Acad. Sci. USA* **105**, 8697 (2008)

12.178 A.M. Hawkridge et al., *Proc. Natl. Acad. Sci. USA* **102**, 17442 (2005)

12.179 G.S. Bodor et al., *Clin. Chem.* **38**, 2203 (1992)

12.180 H.S. Guo et al., *J. Nanosci. Nanotechnol.* **5**, 1240 (2005)

12.181 M. Wolf et al., *Biosens. Bioelectron.* **19**, 1193 (2004)

12.182 S.K. James et al., *Int. J. Cardiol.* **93**, 113 (2004)

12.183 M.C. Fishbein et al., *Cardiovasc. Pathol.* **12**, 65 (2003)

12.184 J.-S. Park et al., *Nature Nanotech.* **4**, 259 (2009)

12.185 T. Kim et al., *Proteomics* **7**, 4203 (2007)

12.186 M. Alonso-Sande et al., *Macromolecules* **39**, 4152 (2006)

12.187 A. Besheer et al., *J. Control. Release* **111**, 73 (2006)

12.188 X.Y. Xiong et al., *J. Control. Release* **120**, 11 (2007)

12.189 W.D. Bennett, *Expert Opin. Drug Deliv.* **2**, 763 (2005)

12.190 P. Dames et al., *Nat. Nanotechnol.* **2**, 495 (2007)

12.191 K. Saito et al., *Magnet. Reson. Med. Sci.* **4**, 151 (2005)

12.192 C. Alexiou et al., *IEEE Trans. Appl. Superconduct.* **16**, 1527 (2006)

12.193 B. Gleich et al., *IEEE Trans. Nanotechnol.* **6**, 164 (2007)

12.194 M.S. Forman et al., *Nat. Med.* **10**, 1055 (2004)

12.195 C. Roney et al., *J. Control. Release* **108**, 193 (2005)

12.196 A. Alzheimer, *Allg. Z. Psychiatr. Psych. – Gerichtl.* **64**, 146 (1907)

12.197 M.S. Wolfe, *Sci. Am.* May 2006, p. 61

12.198 J. Schnabel, *Nature* **459**, 310 (2009)

12.199 A. Finefrock et al., *J. Am. Geriatr. Soc.* **51**, 1143 (2003)

12.200 C. Opazo et al., *J. Biol. Chem.* **277**, 40302 (2002)

12.201 Z. Zhuang et al., *J. Med. Chem.* **44**, 1905 (2001)

12.202 Q. Smith, *A review of Blood Brain Barrier Transport Techniques* (Humana Press, Totowa, NJ, 2003)

12.203 C. Ritchie et al., *Arch. Neurol.* **60**, 1685 (2003)

12.204 X. Huang et al., *Biochemistry* **38**, 7609 (1999)

12.205 L.L. Rubin, J.M. Staddon, *Annu. Rev. Neurosci.* **22**, 11 (1999)

12.206 K.S. Soppimath et al., *J. Control. Rel.* **70**, 1 (2001)

12.207 M.J. Kogan et al., *NanoLett.* **6**, 110 (2006)

12.208 C. Soto et al., *Nat. Med.* **4**, 822 (1998)

12.209 E.A. Fradinger, G. Bitan, *Trends in Biotechnology* **23**, 531 (2005)

12.210 A.J. Haes et al., *J. Am. Chem. Soc.* **127**, 2264 (2005)

12.211 X. Ji et al., *Colloids Surf. B* **50**, 104 (2006)

12.212 S. Linse et al., *Proc. Natl. Acad. Sci. USA* **104**, 8691 (2007)

12.213 V.L. Colvin, K.M. Kulinowski, *Proc. Natl. Acad. Sci. USA* **104**, 8679 (2007)

12.214 J. Laurén et al., *Nature* **457**, 1128 (2009)

12.215 N. Buzhynsky et al., *J. Mol. Biol.* **374**, 162 (2007)

12.216 N.N. Kumar, N.B. Gilula, *EMBO Reports* **8** (1), 51 (1996)

12.217 N. Buzhynskyy et al., *EMBO Rep.* **8**, 51 (2007)

12.218 J. Chen et al., *Nat. Nanotechnol.* **1**, 142 (2006)

12.219 G.A. Silva, *Nat. Nanotechnol.* **1**, 92 (2006)

12.220 R. Oehler, *Max-Planck-Research* **4**, 38 (2001)

12.221 V.T. C. Pappas et al., *Nanolett.* **7**, 513 (2007)

12.222 S. Patil et al., *J. Phys. Chem.* **C111**, 8437 (2007)

12.223 M.T. Huisman et al., *Mol. Pharmacol.* **59**, 806 (2001)

12.224 L.K. Shah, M.M. Amiji, *Pharm. Res.* **23**, 2638 (2006)

12.225 S. Noble, D. Faulds, *Drugs* **52**, 93 (1996)

12.226 A. Bender et al., *Int. Conf. AIDS* **11**, 64 (1996)

12.227 D.B. Shenoy, M.M. Amiji, *Int. J. Pharm.* **293**, 261 (2005)

12.228 M.-C. Bowman et al., *J. Am. Chem. Soc.* **130**, 6896 (2008)

12.229 E.S. Lee et al., *Angew. Chem. Int. Edn.* **47**, 2418 (2008)

12.230 MRS Bull **31**, March 2006, p. 181

12.231 http://www.mtr.com.hk/eng/corporate/file_rep/PR-06-084-E.pdf

12.232 S.T. Kang et al., *Langmuir* **23**, 8670 (2007)

12.233 NSTI Nanotechnology Conference and Trade Show, Boston, USA, 2008; *Biomaterials and Nanotechnology in Tissue Engineering*

12.234 The *Guardian*, October 6, 2007

12.235 L.J. Zhang, T.J. Webster, *Nanotoday* **4**, 66 (2009)

12.236 J.Y. Ying, *Nanotoday* **4**, 1 (2009)

12.237 E.M. Christenson et al., *J. Orthop. Res.* **25**, 11 (2007)

12.238 S. Sirivisoot et al., *Nanotechnology* **18**, 365102 (2007)

12.239 T.J. Webster et al., *Tissue Eng.* **7**, 291 (2001)

12.240 C. Kaya et al., *Adv. Eng. Mater.* **10**, 131 (2008)

12.241 O. Adamopoulos and T. Papadopoulos, *J. Mater. Sci.: Mater. Med.* **18**, 1587 (2007)

12.242 T.J. Webster et al., *J. Biomed. Mater. Res.* **51**, 475 (2000)

12.243 T.J. Webster et al., *J. Biomed. Mater. Res.* **67A**, 975 (2003)

12.244 X. Mao et al., *Tissue Cell* **37**, 349 (2005)

12.245 S.S. Liao et al., *J. Biomed. Mater. Res. Part B: Appl. Biomater.* **69B**, 158 (2004)

12.246 B.-H. Yoon et al., *Biomaterials* **26**, 2957 (2005)

12.247 H.H. K. Xu et al., *Biomaterials* **25**, 4615 (2004)

12.248 L.E. Carey et al., *Biomaterials* **26**, 5002 (2005)

12.249 T.J. Webster et al., *Biomaterials* **20**, 1221 (1999)

12.250 R. Saravana Kumar, R. Vijayalakshmi, *Ind. J. Dent. Res.* **17**, 62 (2006)

12.251 W.J. Li et al., *Biomaterials* **26**, 5158 (2005)

12.252 M. Shin et al., *Tissue Eng.* **10**, 33 (2004)

12.253 N. Bhattacharai et al., *Biomaterials* **26**, 6176 (2005)

12.254 S. Bhattacharyya et al., *MRS Symp. Proc.* **845**, 91 (2005)

12.255 S. Sahoo et al., *Tissue Eng.* **12**, 91 (2006)

12.256 J.K. Savaiano, T.J. Webster, *Biomaterials* **25**, 1205 (2004)

12.257 S. MacNeil, *Materialstoday* **11**, May 2008, p. 26

12.258 K. Rajangam et al., *Nano Lett.* **6**, 2086 (2006)

12.259 L.M. Y. Yu et al., *Materialstoday* **11**, May 2008, p. 36

12.260 R.A. Hule, D.J. Pochan, *MRS Bull.* **32**, 354 (2007)

12.261 D.R. Nisbet et al., *J. Biomater. Sci. Polym. Ed.* **19**, 623 (2008)

12.262 F. Johansson et al., *Biomaterials* **27**, 1251 (2006)

12.263 V.M. Tysseling-Mattiace et al., *J. Neurosci.* **28**, 3814 (2008)

12.264 G.T. Gillies et al., *Nanotechnology* **13**, 587 (2002)

12.265 S.P. Leary et al., *Neurosurgery* **58**, 1009 (2006)

12.266 H.-E. Swoboda, *Best Physik J.*, Sept. 2007, p. 12

12.267 I.Z. Maxwell et al., *Med. Laser Appl.* **20**, 193 (2005)

12.268 N. Shen et al., *Mech. Chem. Biosys.* **2**, 17 (2005)

12.269 U.K. Tirlapur, K. Konig, *Plant J.* **31**, 365 (2002)

12.270 U.K. Tirlapur, K. Konig, *Nature* **418**, 290 (2002)

12.271 S. Kim et al., *Nat. Biotechnol.* **22**, 93 (2004)

12.272 M.F. Yanik et al., *Nature* **432**, 822 (2004)

12.273 M. Sitti, *Nature* **458**, 1121 (2009)

12.274 P. Fromherz, *Chem. Phys. Chem.* **3**, 276 (2002)

12.275 D.W. Sretavan et al., *Neurosurgery* **57**, 635 (2005)

12.276 J. Colombelli et al., *Traffic* **6**, 1093 (2005)

12.277 B. Alberts et al., *Molecular Biology of the Cell* (Garland Science, New York, 2002)

12.278 R.A. Freitas, *J. Amer. Dent. Assoc.* **131**, 1559 (2000)

12.279 S.B. Mitra et al., *J. Am. Dental Associat.* **134**, 1384 (2003)

12.280 S.C. Bayne, *J. Dental Educ.*, May 2005, p. 571

12.281 Y. Yuan et al., *Dental Mater.* **23**, 561 (2007)

12.282 M. Okuda et al., *Oper. Dent.* **27**, 289 (2002)

12.283 R.L. Price et al., *J. Biomed. Mater. Res.* **67A**, 1284 (2003)

12.284 T.J. Webster et al., *Biomaterials* **26**, 953 (2005)

12.285 R.L. Price et al., *J. Biomed. Mater. Res.* **70A**, 129 (2004)

12.286 H.H. K. Xu et al., *J. Dent. Res.* **86**, 378 (2007)

12.287 S.H. Dickens et al., *Dent. Mater.* **19**, 558 (2003)

12.288 P.T. Sharpe, C.S. Young, *Sci. Am.* August 2005, p. 24

12.289 J.Y. Yu et al., www.sciencemag.org/cgi/content/abstract/1151526

12.290 S. Yamanka et al., *Cell* **131**, 861 (2007)

12.291 N. Swaminathan, *Sci. Am. News.* December 26, 2006

12.292 W. Sonoyama et al., *PLoS ONE*, Dec. 2006

12.293 Environmental, Health, and Safety Research Needs for Engineered Nanoscale Materials, US National Nanotechnology Coordination Office (2006); www.nano.gov

12.294 R. Brayner, *Nanotoday* **3**, 1–2, 48 (2008)

12.295 Towards Predicting Nano-Biointeractions: An International assessment of Nanotechnology, Health, and Safety Research, <http://icon.rice.edu>; see K. Rand, *MRS Bull.* **33**, 649 (2008)

12.296 J. Kling, *Nat. Biotechnol.* **10**, 1068 (2007)

12.297 Editorial, *Nat. Nanotechnol.* **3**, 697 (2008)

12.298 J.M. Balbus et al., *Environ. Health Perspect.* **115**, 1654 (2007)

12.299 Commission of the European Union, see *Stuttgarter Nachrichten*, June 17, 2008

12.300 *Legislation to Strengthen Nanotechnology Safety Research*, U. S. House of Representatives, Press Release June 5, 2008

12.301 <http://www.oecd.org/env/nano-safety/>

12.302 N. Pidgeon et al., *Nat. Nanotech.* **4**, 95 (2008)

12.303 A.D. Maynard et al., *Nature* **444**, 267 (2006)

12.304 R.H. Austin, S.F. Lim, *Proc. Natl. Acad. Sci. USA* **105**, 17217 (2008)

12.305 V. Murashov, J. Howard, *Nature Nanotech.* **4**, 467 (2009)

12.306 D. Goldston, *Nature* **450**, 1141 (2007)

12.307 www.fz-juelich.de/pj/index.php?index=707

12.308 *Nature* **456**, 853 (2008)

12.309 M. Pitkethly, *Materialstoday* **12**, Jan-Feb 2009, p. 23; www.rcep.org.uk/novelmaterials.html

12.310 E. Drexler, *Engines of Creation: The Coming Era of Nanotechnology* (Anchor Press/Doubleday, Garden City, NY, 1986)

12.311 B. Joy, *Wired* 8.04, 37 (2000)

12.312 C. Phoenix, E. Drexler, *Nanotechnology* **15**, 869 (2004)

12.313 N. Stephenson, *The Diamond Age: Or, a Young Lady's Illustrated Primer* (Bantam Spectra, New York, 1995)

12.314 M. Crichton, *Prey* (Harper Collins Publ., New York, 2003)

12.315 G.M. Whitesides, *Sci. Am.* Sept. 2001, p. 70

12.316 P.S. Anton et al., The Global Technology Revolution: Bio/Nano/Materials Trends and their Synergies with Information Technology by 2015 (Rand, Santa Monica, 2001)

12.317 S.C. Currall, *Nat. Nanotech.* **4**, 79 (2009)

12.318 C. Toumey, *Nat. Nanotech.* **4**, 136 (2009)

12.319 D.M. Kahan et al., *Nat. Nanotech.* **4**, 87 (2008)

12.320 D.A. Scheufele et al., *Nat. Nanotech.* **4**, 91 (2008)

12.321 N. Lewinski et al., *Smal.* **4**, No. 1, 26 (2008)

12.322 C. Buzea et al., *Biointerphases* **2** (4), MR 17 (2007)

12.323 S. Tinkle (ed.) *Health and Environmental Impacts of Nanoscale Materials—Safety by Design* (MRS Proceedings Vol. 1103E, Warrendale, 2008)

12.324 C. Sayes et al., *Nano Lett.* **4**, 1881 (2004)

12.325 C. Sayes et al., *Toxicol. Lett.* **161**, 135 (2006)

12.326 B.L. Allen et al., *Nano Lett.* **8**, 3899 (2008)

12.327 C.A. Poland et al., *Nat. Nanotechnol.* **3**, 423 (2008)

12.328 C.G. Li et al., *J. Mol. Cell. Biol.* **1**, 37 (2009)

12.329 E. Connor et al., *Small* **1**, 325 (2005)

12.330 Y. Pan et al., *Small* **3**, 1941 (2007)

12.331 W.D. James et al., *Radioanal. Nucl. Chem.* **271**, 455 (2007)

12.332 R. Dunford et al., *FEBS Lett.* **418**, 87 (1997)

12.333 P. Somasundaran et al., *MRS Bull.* **32**, 779 (2007)

12.334 A.K. Gupta, S. Wells, *IEEE Trans. Nanobio.* **3**, 66 (2004)

12.335 W.W. Yu et al., *Nanotechnology* **17**, 4483 (2006)

12.336 B. Wang et al., *Proc. Natl. Acad. Sci. USA* **105**, 18171 (2008)

12.337 M. Akerman et al., *Proc. Natl. Acad. Sci. (USA)* **99**, 12617 (2002)

12.338 S.C. Hsieh et al., *Biomaterials* **27**, 1656 (2006)

12.339 S. Mahendra et al., *Environ. Sci. Technol.* **42**, 9424 (2008)

12.340 J. Lovric et al., *Chem. Biol.* **12**, 1227 (2005)